Institut für Angewandte Physik

Fachrichtung Physik

Fakultät Mathematik und Naturwissenschaften

Technische Universität Dresden

Excitation, Interaction, and Scattering of Localized and Propagating Surface Polaritons
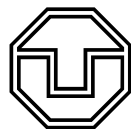
Dissertation

zur Erlangung des akademischen Grades

Doktor rerum naturalium

(Dr. rer. nat.)

vorgelegt von

Jan Renger

geboren am 14.11.1976

in Löbau

TECHNISCHE UNIVERSITÄT DRESDEN

(2006)

1. Gutachter: Prof. Dr. Lukas M. Eng

2. Gutachter: Prof. Dr. Lukas Novotny

3. Gutachter: Prof. Dr. Joachim R. Krenn

Die Arbeit wurde eingereicht am 22. Mai 2006.

IV

Abstract

Surface polaritons, i.e., collective oscillations of the surface charges, strongly influence the optical response at the micro- and nanoscale and have to be accounted for in modern nanotechnology. Within this thesis, certain basic phenomena involving surface polaritons are investigated by means of the semianalytical multiple-multipole (MMP) method. The results are compared to experiments.

In the first part, the surface plasmon resonance (SPR) of metal nanoparticles is analyzed. This resonant collective oscillation of the free electrons in a metallic nanoparticle leads to an enhancement and confinement of the local electric field at optical frequencies. The local electric field can be further increased by tailoring the shape of the particle or by using near-field-interacting dimers or trimers of gold nanospheres. The hot spots found under such conditions increase the sensitivity of surface-enhanced Raman scattering by several orders of magnitude and simultaneously reduce the probed volume, thereby providing single-molecule sensitivity.

The sub-wavelength-confined strong electromagnetic field associated with a SPR provides the basis for scattering-type near-field optical microscopy or tip-enhanced Raman spectroscopy, where the metal particle serves as a probe that is scanned laterally in the vicinity of a substrate. The presence of the latter causes a characteristic shift of the SPR towards lower frequencies. This effect originates in the near-field interaction of the surface charges on the objects. Furthermore, the excitation of higher-order modes becomes possible in case of an excitation by a strongly inhomogeneous wave, such as an evanescent wave. These modes may significantly contribute to the near field but have only very little influence on the far-field signature.

Instead of using resonant probes, one may place a nonresonant probe in the vicinity of a substrate having a high density of electromagnetic surface states. This also produces a resonance of the light scattering by the system. Especially polar crystals, such as the investigated silicon carbide, feature such a high density of surface phonon polariton states in the mid-infrared spectral region, which can be excited due to the near-field interaction with a polarized particle. Thereby, a resonance is created leading to a strong increase of the electric field at the interface.

In the second part of the thesis, special emphasis is put on surface plasmon polaritons (SPPs). Such propagating surface waves can be excited directly by plane waves only at patterned interfaces. This process is studied for the case of a groove. The groove breaks the translational invariance, so that the SPPs can be launched locally at the edges of the groove. Additionally, the mode(s) inside the groove are excited. These modes can basically be understood as metal-

insulator-metal cavity modes. Their dispersion strongly depends on the groove width. The cavity behavior caused by the finite depth provides another degree of freedom for optimizing the SPP excitation by plane waves.

Thin metallic films deposited on glass offer two different SPP waveguide modes, each of which can be addressed preferentially by a proper choice of the width of the groove. The reflection, transmission, scattering, and the conversion of the modes at discontinuities such as edges, steps, barriers, and grooves can be controlled by appropriately designing the geometry at the nanoscale.

Furthermore, the excitation of SPPs at single and multiple slits in thin-film metal waveguides on glass and their propagation and scattering is shown by scanning near-field optical experiments. Such waveguide structures offer a means for transporting light in a confined way. Especially triangularly shaped waveguides can be used to guide light in sub-wavelength spaces.

Kurzfassung

Die Wechselwirkung von elektromagnetischer Strahlung mit sub-λ-kleinen Teilchen bzw. Oberflächenstrukturen (λ – Wellenlänge) ermöglicht nicht nur eine Miniaturisierung optischer Geräte, sondern erlaubt sehr interessante Anwendungen, beispielsweise in der Sensorik und Nahfeldoptik. In der vorliegenden Arbeit werden die zu Grunde liegenden Effekte im Rahmen der klassischen Elektrodynamik mit Hilfe der semianalytischen Methode der multiplen Multipole (MMP) analysiert, und die Ergebnisse werden mit Experimenten verglichen.

Im ersten Teil werden Oberflächenplasmonenresonanzen (engl. surface plasmon resonance – SPR) einzelner und wechselwirkender Metallteilchen untersucht. Die dabei auftretende resonante kollektive Schwingung der freien Elektronen des Partikels bewirkt eine deutliche Erhöhung und Lokalisierung des elektromagnetischen Feldes in seiner Umgebung. Die spektrale Position und die Stärke der SPR eines Nanoteilchens, die von dessen geometrischer Form, Permittivität und Umgebung abhängen, können nur im Grenzfall sehr kleiner ($\ll \lambda$) Teilchen elektrostatisch beschrieben werden, wohingegen der verwendete semianalytische MMP-Ansatz weitaus flexibler ist und insbesondere auch auf größere Partikel, Teilchen mit komplizierterer Form bzw. Ensembles von Partikeln anwendbar ist.

Die betrachteten einzelnen kleinen ($< \lambda$) Goldkügelchen und Silberellipsoide besitzen eine stark ausgeprägte SPR im sichtbaren optischen Bereich. Diese ist auf eine dipolartige Polarisierung des Teilchens zurückzuführen. Höhere Moden der Polarisation können entweder als Folge von Retardierungseffekten an größeren ($\sim \lambda/2$) Teilchen oder bei der Verwendung inhomogener (z.B. evaneszenter) Wellen angeregt werden.

Partikel, die sich in der Nähe eines Substrates befinden, unterliegen der Nahfeldwechselwirkung zwischen den (lichtinduzierten) Oberflächenladungen auf der Oberfläche des Teilchens und des Substrats. Dies führt zu einer Verschiebung der SPR zu niedrigeren Frequenzen und einer Erhöhung des lokalen elektrischen Feldes. Letzteres bildet die Grundlage z.B. der spitzenverstärkten Raman-Spektroskopie und der optischen Nahfeldmikroskopie mit Streulichtdetektion.

Dasselbe Prinzip bewirkt ein stark überhöhtes elektrisches Feld zwischen miteinander wechselwirkenden Nanopartikeln, welches z.B. die Sensitivität der oberflächenverstärkten Raman-Mikroskopie um mehrere Größenordnungen steigern kann.

Im Gegensatz zur SPR einzelner Nanopartikel kann die Resonanz der Lichtstreuung im Fall eines Partikels in der Nähe eines Substrats aus der durch die Nahfeldwechselwirkung induzierten Anregung elektromagnetischer Oberflächenzustände entstehen. Diese wirken ihrerseits auf das Nanopartikel zurück, wobei eine resonante Lichtstreuung beobachtbar ist. Dieser, am Beispiel einer metallischen Nahfeldsonde über einem Siliziumcarbid-Substrat analysierte, Effekt ermöglicht bei einer ganzen Klasse von polaren Kristallen interessante Anwendungen in

der Mikroskopie und Sensorik basierend auf der hohen Dichte von Oberflächenphononpolaritonen dieser Kristalle im mittleren infraroten Spektralbereich und deren nahfeldinduzierten Anregung.

Im zweiten Teil der Arbeit werden kollektive Anregungen von Elektronen an Metalloberflächen untersucht. Die dabei auftretenden plasmonischen Oberflächenwellen (engl. surface plasmon polaritons – SPPs) weisen einen exponentiellen Abfall der Intensität senkrecht zur Grenzfläche auf. Diese starke Lokalisierung der Energie an der Oberfläche bildet die Grundlage vieler Anwendungen, z.B. im Bereich der hochempfindlichen Detektion (bio)chemischer Verbindungen oder für eine zweidimensionale Optik (engl. plasmonics).

Das Aufheben der Translationsinvarianz längs der Oberfläche ermöglicht die direkte Anregung von SPPs durch ebene Wellen. Die Abhängigkeit dieser Kopplung von der Geometrie wird am Beispiel eines Nanograbens untersucht. Dabei werden neben den SPPs ebenfalls eine oder mehrere Moden im Graben angeregt. Folglich ermöglicht die geeignete Wahl der Grabengeometrie die Optimierung der Umwandlung von ebenen Wellen in SPPs.

Im – in der Praxis weit verbreiteten – Fall asymmetrisch eingebetteter metallischer Dünnschichtwellenleiter existieren zwei Moden. In Abhängigkeit von der Grabenbreite kann die eine oder die andere Mode bevorzugt angeregt werden.

Die Analyse der Wechselwirkung von SPPs mit Oberflächenstrukturen, z.B. Kanten, Stufen, Barrieren und Gräben, zeigt die Möglichkeit der Steuerung der Reflexions-, Transmissions- und Abstrahleigenschaften durch die gezielte Wahl der Geometrie der „Oberflächendefekte" auf der Nanoskala und deckt die zu Grunde liegenden Mechanismen und die daraus resultierenden Anforderungen bei der Herstellung neuer plasmonischer Komponenten auf. Exemplarisch wird das Prinzip der SPP-Anregung an einzelnen und mehreren Gräben in dünnen metallischen Filmen sowie der sub-λ-Feldlokalisierung an sich verjüngenden metallischen Dünnschichtwellenleitern unter Verwendung der optischen Nahfeldmikroskopie experimentell gezeigt.

Contents

List of Figures

List of Tables

List of abbreviations

The list comprises selected symbols and abbreviations:

Symbol / abbreviation	Meaning
$[\ldots]^*$	complex conjugated
i	imaginary unit $i^2 = -1$
$\mathrm{Im}[\ldots]$	imaginary part
$\mathrm{Re}[\ldots]$	real part
∇	nabla (differential) operator
α	polarizability
α_{eff}	effective polarizability
β	surface response function
δ_{SPP}	propagation length of SPP
δ_{skin}	field penetration/skin depth in the metal
ε	permittivity
γ_i	longitudinal propagation constant of the i'th mode
λ, λ_0	wavelength in free space
Λ	modulation period of the field, wavelength of SPP or mode
ω	frequency
ω_{SP}	surface plasmon frequency
μ	permeability, $\mu = 1$ at optical frequencies was assumed
ν	wavenumber $\nu = \frac{1}{\lambda}$
ρ	surface charge density, radius
σ	mode excitation cross section
c	speed of light in vacuum
k_0	wavevector in vacuum $k_0 = \omega/c$
k	absolute value of wavenumber in the medium $k = (\varepsilon\mu)^{\frac{1}{2}}k_0$
$k_\parallel$	component of the wavevector parallel to the interface
$k_\perp$	component of the wavevector normal to the interface
n	refractive index
r	reflection coefficient
t	transmission coefficient, time
$\boldsymbol{E}$	vector of the electric field
$\boldsymbol{H}$	vector of the magnetic field
ATR	attenuated total internal reflection
EBL	electron beam lithography
FDTD	finite-difference time domain

Symbol / abbreviation	Meaning
FE	field enhancement
FIB	focused ion beam
MaX-1	Maxwell solver that includes MMP
MIM	metal-insulator-metal structure
MMP	multiple-multipole method
NA	numerical aperture
SEM	scanning electron microscopy
SERS	surface-enhanced Raman scattering
SiC	silicon carbide
SNOM	scanning near-field optical microscope
s-SNOM	scattering-type/apertureless SNOM
SPhP	surface phonon polariton
SPP	surface plasmon polariton
SPR	surface plasmon resonance
TERS	tip-enhanced Raman spectroscopy
TIR	total internal reflection

Chapter 1

Introduction

Optics – one of the oldest disciplines in physics – has undergone a rapid change and progress in the last decades with regard to understanding the interaction of light with very small structures, mainly pushed by new fabrication techniques and applications relying on them. In the limit that the wavelength is no longer small compared to the structural sizes, the classical concepts and techniques known from ray optics cannot be applied. Moreover, some terms, such as reflection and transmission, become (partially) meaningless while scattering and absorption have to be taken into account in order to appropriately describe the optical properties of such nanostructures. This complex subject, called nanooptics, comprises a lot of interesting resonance effects which have to be considered in today's nanotechnology and optoelectronics. Furthermore, understanding the interaction of light with sub-wavelength-sized structures opens a new dimension for tailoring the optical properties of artificial materials and devices, such as metamaterials and negative-refractive-index materials [1, 2].

Especially the polarizability of noble-metal nanoparticles may show a resonance in the visible spectral region. This phenomenon is called surface plasmon resonance (SPR)[1], which reflects the fact that the polarizability of metals is dominated by a plasma oscillation of the free electrons. The attractive feature of such SPRs is that the electromagnetic field in the vicinity of the particle is strongly enhanced. This field confinement opens the door to several prospective applications such as the utilization of "hot spots"in the electric field to chemically sense small volumes for example in surface-enhanced Raman scattering (SERS) [3–5]. Further on, such a SPR can be used to increase the sensitivity in scattering-type near-field optical microscopy (s-SNOM) [6–8] which allows the lateral mapping of the optical properties with a

---

[1]The term surface plasmon resonance is used for different phenomena in parallel in literature. The term plasmon denotes the quantum unit of the plasma oscillation in analogy to a photon. Within this thesis, the surface plasmon polariton resonance of nanoparticles is called surface plasmon resonance (SPR) and the term polariton is omitted in order to underline the localized nature of the oscillating plasma wave within the particle. Later, the propagating surface waves at a metal-dielectric boundary are called surface plasmon polariton (SPP) emphasizing their propagation along the surface and to contrast to the SPR.

lateral resolution beyond the diffraction limit of classical far-field optics. Similar techniques can be used in near-field nanolithography [9] to structure a photoresist at sub-wavelength scales or to store data optically with ultrahigh density.

Similarly, polarization waves of the electron plasma at the surface of a metal may cause an exponentially decaying electromagnetic field in the dielectric [10]. Such (propagating) surface waves – commonly referred to as surface plasmon polaritons (SPPs) – are associated with a strong concentration of the electromagnetic field at the interface. Therefore, they are well suited for surface sensing applications, such as chemical and biosensing (see Ref. [11, 12] and references therein).

The possibility to transport light in a confined way by means of SPPs is currently attracting a lot of attention as it promises a way to construct small optical interconnections and signal processing devices on electronic chips [13, and references therein] in order to further speed up electronic devices.

The impact of surface plasmons and their potential applications become even more obvious when we look closer into today's optoelectronic devices. The metal structures used for the electrical connections also provide the ground on which SPPs can exist. Especially, excited molecules close to metal surfaces couple to the SPP states [14]. Fortunately, this mechanism does not inevitably reduce the device performance because the inherent field confinement and enhancement of SPPs can be utilized in a cavity. Furthermore, the electromagnetic energy trapped in the SPPs can be recycled into propagating modes on nanopatterned interfaces and, additionally, the light transported by the SPP can be easily coupled out of the (organic) light-emitting devices [15–17] because it is not subjected to the trapping by total internal reflection inside the device.

Outline of this work

This work is organized as follows: After a brief introduction to the method of multiple multipoles and a short excursion into the interaction of electromagnetic radiation with matter in chapter 2, this powerful, numerically efficient, and physically intuitive technique is applied to problems both of near-field optics and plasmonics in order to shed light on the underlying physics. In this thesis, the particular problems under investigation can be grouped into two parts as outlined in Fig. 1.1:

- The *localized* surface plasmon resonance (SPR) of single nanoparticles is discussed in chapter 3. The associated strong, locally confined field may be further increased by means of closely arranged nanoparticles that interact via their near-fields, as discussed in chapter 4 for dimers and trimers of gold spheres. Special emphasis is put on evaluating the local electric field strength, which determines the sensitivity in processes that critically depend on it as, for example, Raman scattering or second harmonic generation
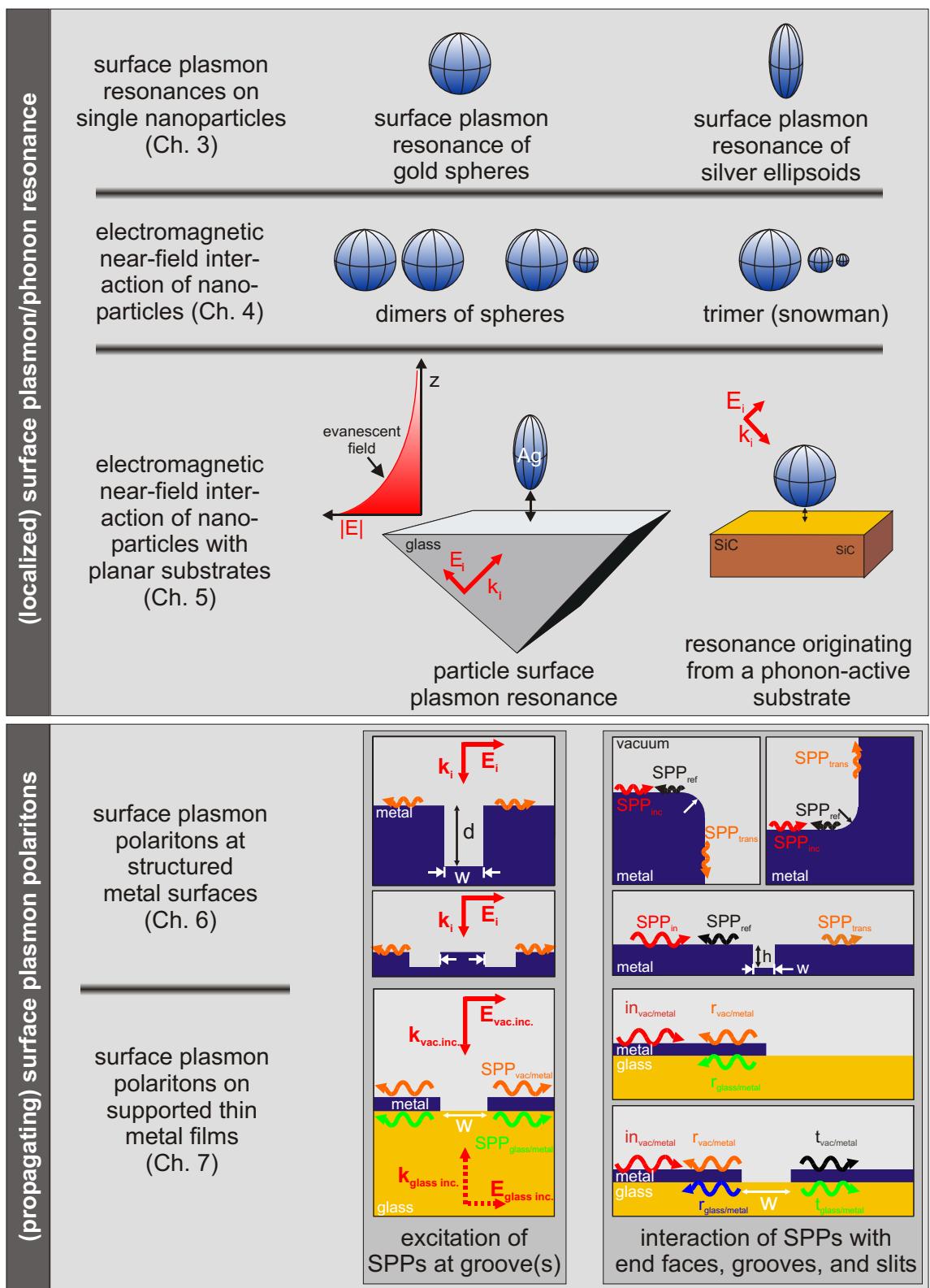
Figure 1.1 *Thesis overview – systems studied in this thesis.*

and other nonlinear processes.

The strong, confined electric field close to nanoparticles may also be used to probe the local optical properties of a sample by scanning such a nanoparticle across it. The effects occurring when such a probe is placed close to a planar interface are discussed in chapter 5 for two distinct cases: Firstly, the probe is excited at its SPR. Secondly, the excitation in the mid-infrared spectral region is far-off from the SPR. In the latter case, the polarized probe may excite localized surface phonon polaritons on polar crystals, which opens the door to interesting sensing applications.

- The second part of the thesis is devoted to propagating surface plasmon polaritons present at the interface between a metal and a dielectric. The excitation, interaction, and scattering of SPPs on patterned surfaces or at surface defects is first analyzed assuming the simple case of an interface between metallic and dielectric semi-infinite half-spaces in chapter 6. The modifications in the case of plasmonic devices based on thin-film metal waveguides is analyzed in chapter 7.

Chapter 2

The multiple-multipole method

This chapter surveys the numerical methods used in electromagnetics. Special emphasis is laid on the method of multiple multipoles, which is extensively used in the following parts of this thesis.

2.1   Introduction

The interaction of electromagnetic radiation with matter is described by Maxwell's equations together with the constitutive relations chosen. For linear, homogeneous, isotropic, locally responding materials, harmonic time dependence $e^{-i\omega t}$ of the fields, and in the absence of free charges and free currents, these partial differential equations are given by [18, 19]:

$$\nabla \cdot \varepsilon \boldsymbol{E} = 0, \tag{2.1}$$

$$\nabla \times \boldsymbol{E} = i\omega\mu\boldsymbol{H}, \tag{2.2}$$

$$\nabla \cdot \mu \boldsymbol{H} = 0, \tag{2.3}$$

$$\nabla \times \boldsymbol{H} = -i\omega\varepsilon\boldsymbol{E}. \tag{2.4}$$

The quantities ε and μ are the complex permittivity and permeability of the material that is usually divided into so-called domains D_i in which ε and μ are spatially uniform.

Provided that the material is isotropic so that ε and μ are simple scalars, Eqs. (2.1) and (2.3) in such domains reduce to $\nabla \cdot \boldsymbol{E} = 0$, $\nabla \cdot \boldsymbol{H} = 0$. The curl of Eqs. (2.2) and (2.4) can then be written as the homogeneous Helmholtz equation:

$$\left(\nabla^2 + k^2\right)\boldsymbol{E} = 0, \qquad \left(\nabla^2 + k^2\right)\boldsymbol{H} = 0, \tag{2.5}$$

with $k^2 = \varepsilon\mu\omega^2/c^2$. Therefore, every electromagnetic field must satisfy Eq. (2.5). The total electromagnetic field $\boldsymbol{E}$ and $\boldsymbol{H}$ can be expressed as a superposition of the excitation field $\boldsymbol{E}_{\text{in}}$ and $\boldsymbol{H}_{\text{in}}$, and the one arising because of the light-matter interaction, $\boldsymbol{E}_{\text{sca}}$ and $\boldsymbol{H}_{\text{sca}}$:

$$\boldsymbol{E} = \boldsymbol{E}_{\text{in}} + \boldsymbol{E}_{\text{sca}}, \qquad \boldsymbol{H} = \boldsymbol{H}_{\text{in}} + \boldsymbol{H}_{\text{sca}}. \tag{2.6}$$

These expressions together with the linearity of the operator $(\nabla^2 + k^2)$ can be used to split off the known excitation resulting in an inhomogeneity on the right side of the Helmholtz equation (2.5) that includes only $\boldsymbol{E}_{\text{sca}}$ and $\boldsymbol{H}_{\text{sca}}$ instead of the total fields. The solution has also to fulfill the boundary conditions at the border ∂D_{ij} between D_i and D_j:

$$
\begin{aligned}
(\boldsymbol{E}_{\parallel}^{D_i} - \boldsymbol{E}_{\parallel}^{D_j}) &= 0, \\
(\varepsilon_{D_i} E_{\perp}^{D_i} - \varepsilon_{D_j} E_{\perp}^{D_j}) &= 0, \\
(\boldsymbol{H}_{\parallel}^{D_i} - \boldsymbol{H}_{\parallel}^{D_j}) &= 0, \\
(\mu_{D_i} H_{\perp}^{D_i} - \mu_{D_j} H_{\perp}^{D_j}) &= 0.
\end{aligned}
\tag{2.7}
$$

The symbols $\parallel$, $\perp$ indicate the field component parallel and normal to the boundary, respectively.

The analytical solution of this partial differential equation is known for some special cases only, mostly for problems having a high degree of symmetry, e.g. being spherical. Many numerical techniques [20, 21, and references therein] for solving Eq. (2.5) have been implemented, last but not least promoted by the tremendously increased computation speed of modern computers. The methods can be classified with respect to whether they discretize the volume (domain methods, e.g. the finite-difference time domain (FDTD) method) or the boundary (boundary methods, e.g. *generalized multipole techniques* (GMT) such as the *multiple-multipole* method (MMP)). The other main classification criterion is whether the method assumes a fixed frequency, corresponding to a time dependence $e^{-i\omega t}$, (frequency domain, e.g. MMP) or discretizes the temporal behavior of the electromagnetic field (time domain, e.g. FDTD). As usual, no method is suitable for all various kinds of problems and the appropriate method has to be chosen for every individual case. For instance, for the investigation of femtosecond nonlinear optical effects in anisotropic media, FDTD might be a better choice, whereas linearly responding media can be very well and efficiently modelled by MMP.

2.2   Solving Maxwell's equations using MMP

Starting in the 1980s, the multiple-multipole method (MMP) was developed and implemented at the Swiss Federal Institute of Technology in Zurich by Ch. Hafner and coworkers [22–24]. This well established method belongs to the GMT group and has its roots in the method of image charges, Mie theory, circular harmonic analysis and point matching. MMP has been successfully applied to various problems in electromagnetism, such as light propagation in waveguides [25, 26] and periodic structures [27] (e.g. lithography masks in semiconductor industries [28], light propagation and scattering at small apertures [29, 30], the analysis and optimization of photonic crystals [31]), and many others. It is beyond the scope of this work to present all the details (see [23, 24, 32–34]) of MMP, but we rather restrict ourselves to a short overview.

In this frequency domain technique, the time dependence of the electromagnetic field is assumed to be harmonic, $e^{-i\omega t}$, which is not written explicitly in the following equations. Furthermore, MMP is a semianalytical boundary method in the sense that the differential equations (2.5) are exactly (analytically) fulfilled inside the homogeneous domains D_i, whereas the boundary conditions are only approximately satisfied. Because of the fact that only the boundary needs to be discretized, the numerical effort is considerably smaller than in domain techniques such as FDTD, especially for problems close to one that has a known analytical solution.

The electromagnetic field $F^{D_i}(\vec{r}) = \{\boldsymbol{E}(\vec{r}), \boldsymbol{H}(\vec{r})\}$ at the position $\vec{r}$ inside D_i can be written as a linear superposition:

$$F^{D_i}(\vec{r}) = f_{\text{in}}^{D_i}(\vec{r}) + \sum_{\eta} c_{\eta} f_{\eta}^{D_i}(\vec{r}) + \text{error}. \tag{2.8}$$

The so-called expansions, formed by a subset of the basis functions $f_{\eta}^{D_i}$, are known analytical solutions of Maxwell's equations, such as multipole fields or Bessel functions of different orders and degrees, waveguide modes, plane waves, or even more complex functions, e.g. distributed multipoles. The remaining task is to fulfill the continuity of $E_{\parallel}^{D_{i,j}}$, $H_{\parallel}^{D_{i,j}}$, $\varepsilon_{D_{i,j}} E_{\perp}^{D_{i,j}}$, and $\mu_{D_{i,j}} H_{\perp}^{D_{i,j}}$ at the boundary ∂D_{ij} between D_i and D_j. This is done at certain collocation points, leading to an algebraic matrix equation of the type:

$$\sum_{\xi} \mathcal{A}_{\zeta,\xi} \boldsymbol{C}_{\xi} = \boldsymbol{G}_{\zeta}. \tag{2.9}$$

The elements of the rectangular matrix $\mathcal{A}_{\zeta,\xi}$ are known, because the columns correspond to the basis functions and each row corresponds to a boundary condition at one of the collocation points. The vector $\boldsymbol{G}_{\zeta}$ represents the excitation, and hence the only unknown vector $\boldsymbol{C}_{\xi}$ is obtained by solving Eq. (2.9). The *generalized point matching* (GPM) technique employed uses an overdetermined system of equations (more boundary conditions than coefficients c_{η}), which is much more robust with respect to the individual positions of the collocation points than point matching techniques using a square matrix [24, p. 191]. The expansion coefficients are determined in a least-square sense by minimizing the residual $R = \|\mathcal{A}\boldsymbol{C} - \boldsymbol{G}\|^2$. The usual vector norm $\| \cdot \|^2$ is used, which corresponds to the total field mismatch summed over all collocation points N_{col} at the boundaries:

$$\begin{aligned}
R = \sum_{k=1}^{N_{col}} \Bigg\{ &|w_{E_{\parallel}}(\vec{r}_k)|^2 \left[\boldsymbol{E}_{\parallel}^{D_i}(\vec{r}_k) - \boldsymbol{E}_{\parallel}^{D_j}(\vec{r}_k) \right] \cdot \left[\boldsymbol{E}_{\parallel}^{D_i}(\vec{r}_k) - \boldsymbol{E}_{\parallel}^{D_j}(\vec{r}_k) \right]^* \\
&+ |w_{E_{\perp}}(\vec{r}_k)|^2 \left| \left[\varepsilon_{D_i} E_{\perp}^{D_i}(\vec{r}_k) - \varepsilon_{D_j} E_{\perp}^{D_j}(\vec{r}_k) \right] \right|^2 \\
&+ |w_{H_{\parallel}}(\vec{r}_k)|^2 \left[\boldsymbol{H}_{\parallel}^{D_i}(\vec{r}_k) - \boldsymbol{H}_{\parallel}^{D_j}(\vec{r}_k) \right] \cdot \left[\boldsymbol{H}_{\parallel}^{D_i}(\vec{r}_k) - \boldsymbol{H}_{\parallel}^{D_j}(\vec{r}_k) \right]^* \\
&+ |w_{H_{\perp}}(\vec{r}_k)|^2 \left| \left[\mu_{D_i} H_{\perp}^{D_i}(\vec{r}_k) - \mu_{D_j} H_{\perp}^{D_j}(\vec{r}_k) \right] \right|^2 \Bigg\}.
\end{aligned} \tag{2.10}$$

The weights in Eq. (2.10) are defined as [24, p. 233]:

$$
w_{E_\parallel}(\vec{r}_k) = \eta_k \, (\Delta s_k)^{\frac{1}{2}} , \qquad\qquad w_{H_\parallel}(\vec{r}_k) = \eta_k \left(\frac{\mu_{D_i} \mu_{D_j}}{\varepsilon_{D_i} \varepsilon_{D_j}} \right)^{\frac{1}{4}} (\Delta s_k)^{\frac{1}{2}},
$$

$$
w_{E_\perp}(\vec{r}_k) = \eta_k \left(\frac{1}{\varepsilon_{D_i} \varepsilon_{D_j}} \right)^{\frac{1}{2}} (\Delta s_k)^{\frac{1}{2}}, \qquad w_{H_\perp}(\vec{r}_k) = \eta_k \left(\frac{1}{\varepsilon_{D_i} \varepsilon_{D_j} \mu_{D_i} \mu_{D_j}} \right)^{\frac{1}{4}} (\Delta s_k)^{\frac{1}{2}}.
$$

The factors containing ε and/or μ maintain the dimensional consistency and ensure equal weighting of all boundary conditions. Otherwise, the mismatch given by Eq. (2.10) could differ for the individual field components by orders of magnitude. The factors Δs_k in the weights reflect the fact that the collocation points need not be distributed equidistantly across ∂D_{ij}. The interface segment Δs_k, which is associated with the matching point at $\vec{r}_k$, has an area defined by the distance to the neighboring matching points. In 2D models, these small surface elements are replaced by line elements. The distance between neighboring collocation points has to be chosen carefully to properly account for the field variation which strongly depends on the geometrical features to be modelled. The weights ensure an appropriate balancing of the various collocation points in the residual of Eq. (2.10). The parameter η_k may be defined manually to force the code to emphasize certain regions or points, which is sometimes necessary.

The residual defined by Eq. (2.10) is evaluated using linear algebra routines for solving the matrix Eq. (2.9). The standard solver used in MMP is the Givens algorithm based on plane rotations and the QR decomposition [24,35, and references therein]. The accuracy of the result is gauged by looking at the violation of the boundary conditions at the collocation points rather than looking at the functional value R. The program/graphical user interface is able to visualize the error distribution (violation of the boundary conditions) locally. Therefore, one may try to improve the setting/orders of the expansion in a next step in order to achieve more accurate results. The field at any point in space is defined by the series expansion in Eq. (2.8). Therefore, it is possible to visualize the field on any afterwards-chosen grid or perform integrations without recomputing the solution, which is a unique advantage as compared to the domain methods, which have to store the field at every predefined grid point.

2.3   Further remarks on MMP modelling

The results presented in this work were obtained with two different implementations of the MMP method. The MMP-3D Fortran code [34] was compiled under SGI-IRIX [36] and the executable program was run on SGI Origin 2000 and Origin 3800 at the Center for Information Services and High Performance Computing at the TU Dresden. This environment was used

for solving the problems presented in chapter 5, while the graphical user interface XMMPTool running on the local computer served for modelling and visualization. The calculations in chapters 4, 6, and 7 as well as most of the results in chapter 3 were carried out by the Microsoft-Windows-based MMP program MaX-1 [37]. The considerably increased speed of modern desktop computers allows MaX-1 to run on such a computer with similar performance as that obtained on a single CPU of a several years old high-power multiprocessor machine. Despite the fact that both MMP packages use the same underlying method, the files containing the project description, e.g. boundary definitions, expansion settings etc., are not portable because MaX-1 uses new features which were not or differently implemented in the older version. The following paragraphs are intended to shortly review certain important technical aspects of the modelling procedure.

Boundaries

The boundaries separating the piecewise homogeneous domains have to be chosen according to the interfaces present in the problem to be modelled. Occasionally *fictitious boundaries* are introduced inside physically homogeneous (ε, μ uniform) domains for numerical reasons and convergence purposes [24]. Therefore, the code can be forced to use only a small set of expansions for the field evaluation in certain domains. The old MMP-3D version creates the collocation points, in the following called *matching points*, according to the previously chosen line or surface elements. Hence, changing the positions and/or orders of the multipoles (expansions) may require to redefine these elements. This drawback was eliminated in MaX-1. Here the boundary is specified by defining certain points between which a spline approximation is used. The program automatically generates the matching points along this spline-interpolated boundary, taking into account the position and the order of the multipoles as well as user-defined values such as the desired overdetermination of the matrix (Eq. (2.9)) or the maximum distance between neighboring matching points. Nevertheless, in order to keep to the safe side it is highly recommended that the user manually inspects the automatically generated matching point distribution to prevent violation of the sampling theorem [34].

Expansion setting

In principle, the series expression of the electromagnetic field in Eq. (2.8) can be done by any complete set of functions $f_\eta^{D_i}$ that satisfy Eq. (2.5). A highly accurate solution may be obtained with minimal numerical effort (small number of η) if known analytical solutions of the problem under investigation are used. Because for many problems such eigensolutions are not known, *multipoles* of certain orders and degrees placed at *multiple locations* are widely used to describe the field. As the field at the origin of every individual multipole is singular, the multipoles modelling the field in D_i have to be placed outside of this domain and the

validity is usually restricted to a single domain only:

$$
f_k^{D_i} = \begin{cases} f_k & \text{in } D_i \text{ and on } \partial D_{ij} \\ 0 & \text{in } D_j \ (j \neq i). \end{cases}
\tag{2.11}
$$
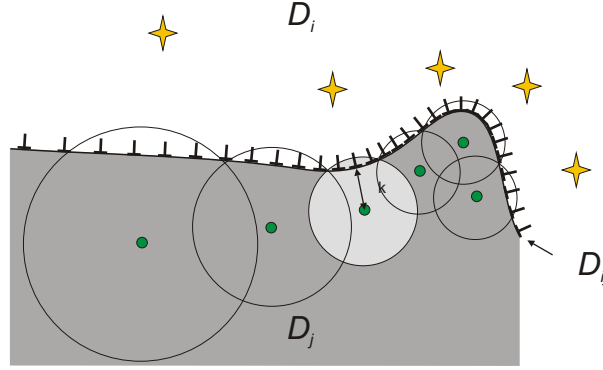
Figure 2.1   *MMP uses multipoles at multiple locations to approximate the field at the discretized boundary ∂D_{ij}. The multipoles describing the field in the domain D_i, marked by the green circles, have to be placed outside D_i (in D_j) because of the singularities at their origins. The area of greatest influence of a single multipole is indicated by the circles having radii of $1.2 \ldots 1.4 \cdot \rho_k$.*

Several aspects have to be kept in mind for the positioning of the multipoles:

- The field at a certain matching point is mainly defined by the closest multipole. In order to avoid numerical dependencies between neighboring multipoles, the distance between them should be larger than 1.2 to 1.4 ρ_k [34], where ρ_k is the distance to the nearest matching point as illustrated in Fig. 2.1.

- To model regions where the field varies strongly, the multipoles have to be placed closer to the boundary, and/or their orders has to be increased locally. Such strongly varying fields mostly coincide with pronounced geometrical features at the boundary such as small curvature radii (see Fig. 2.1).

- The size of the matrix as well as the time for solving Eq. (2.9) increase with the number of expansions. Therefore, regions where the field behaves regularly should be modelled with a low density of multipoles.

The automated multipole setting routine implemented in MaX-1 by E. Moreno [38] helps to distribute the multipoles but the parameters used by this procedure have to be adapted and optimized for the actual problem.

Other types of expansions, such as multipoles distributed along a line or ring, Bessel functions, and harmonic expansions (plane waves/Rayleigh waves) are also implemented, increasing the flexibility of the code as well as improving the convergence when used properly. Another attractive feature of MMP is its very close relationship to analytical routines, which allows one to incorporate previously found or analytical solutions, e.g. waveguide modes, as basis-functions in Eq. (2.8) by defining so-called connections. A *connection* is a linear superposition of basis functions with given coefficients a_l:

$$f_{\mathrm{con}}(\vec{r}) = \sum_l a_l f_l(\vec{r}). \tag{2.12}$$

The internal coefficients may be obtained by solving an eigenvalue problem or problems being less complex (e.g. symmetric). These connections can describe the field in multiple domains and are handled as a whole. Therefore, it is possible to gain physical insight by tracking the c_η coefficient of the connection to map how this connection (e.g. mode) contributes to the solution.

Last but not least, MaX-1 can be controlled via *directives*. Similar to macros, they provide a means to access all program features, such as defining the frequency and geometry, setting multipoles, running the solver, etc. With this, one can easily change the geometry, as extensively done in chapters 6 and 7 of this thesis.

Chapter 3

Local field confinement and enhancement

The interaction of electromagnetic radiation with small particles has again been pushed into the focus of research in the last years. The broad interest is mainly motivated by sensorics and local-probe microscopy techniques as well as by the greatly improved experimental facilities compared to the time when G. Mie [39] and Lord Rayleigh did their pioneering work on understanding the optical properties of small particles ($\ll \lambda$). Such small particles may show a resonance of their polarizability, and hence, a locally strongly enhanced field, which can be used to enhance physical phenomena that are sensitive to the local electric field. The Raman cross section, for example, may be increased by many orders of magnitude (surface-enhanced Raman scattering [3, 4]). Nowadays, tip-enhanced Raman scattering [40–42] even provides the sensitivity and confinement necessary for single-molecule spectroscopy [43].
In the following, the basic mechanism of light interacting with matter at the nanometer scale will be discussed, starting with an electrostatic approximation. After a short review of the key points of this well known model, its limitations are presented by analyzing gold and silver particles having diameters outside the small-diameter regime.

3.1   Optical properties of single nanoparticles

The fully three-dimensional solution of the electrodynamic response of a particle excited by an electromagnetic wave turns out to be non-trivial in general. However, to a large extent, the underlying phenomena and physics can be analyzed and understood by means of the much simpler quasi-electrostatic model [19, 44]. For particles being small compared to the incident wavelength λ, the exciting field $\boldsymbol{E}_{\text{in}}$ is nearly uniform across the whole particle and the retardation arising because of the finite speed of light is negligible. Consequentially, the scattering problem can be evaluated in the electrostatic limit by simply calculating the

polarization of the particle under the assumption of a time-harmonic oscillation.

For an ellipsoid with the semiaxes $a \geq b \geq c$ aligned parallel to the x, y, and z coordinate axes, the dipole moment is given by the polarizability α (see Ref. [19] p. 145) in the principal axis system:

$$P_{\mathrm{x,y,z}} = \alpha_{\mathrm{x,y,z}} \, \varepsilon_0 E_{\mathrm{in,x,y,z}} \tag{3.1}$$

$$\text{with } \alpha_{\mathrm{x,y,z}} = \frac{4}{3}\pi abc \frac{\varepsilon - \varepsilon_i}{\varepsilon_i + L_{\mathrm{a,b,c}}(\varepsilon - \varepsilon_i)}. \tag{3.2}$$

The parameters ε and ε_i are the dielectric "constants" of the material of the particle and of the surrounding medium, respectively. For spheroids, the purely geometric factor L_j can be expressed in terms of the eccentricity e [19].

Prolate spheroid (b = c):

$$L_a = \frac{1 - e^2}{e^2} \left[-1 + \frac{1}{2e} \ln \frac{1 + e}{1 - e} \right], \qquad e^2 = 1 - \frac{b^2}{a^2}, \tag{3.3}$$

Oblate spheroids (a = b):

$$L_a = \frac{g(e)}{2e^2} \left[\frac{\pi}{2} - \arctan g(e) \right] - \frac{g^2(e)}{2}, \tag{3.4}$$

$$g(e) = \left(\frac{1 - e^2}{e^2} \right)^{\frac{1}{2}}, \qquad e^2 = 1 - \frac{c^2}{a^2}. \tag{3.5}$$

The remaining factors L_b or L_c are fixed by the relation:

$$L_a + L_b + L_c = 1.$$

The polarization of the particle is thus driven by the oscillating incident field. The oscillating charges on the particle cause a scattering into the far field as well as absorption of electromagnetic radiation. Within the framework of the quasi-electrostatic model the absorption cross section C_{abs} is simply given by:

$$C_{\mathrm{abs}} \sim k \, \mathrm{Im}[\alpha] \quad \text{with} \quad k = \frac{2\pi}{\lambda}.$$

Therefore, the internal losses are proportional to the particle volume, whereas the scattering cross section C_{sca}, given by

$$C_{\mathrm{sca}} \sim \frac{k^4}{6\pi} \, |\alpha|^2 \, ,$$

is proportional to the square of the volume. This leads to a rapidly vanishing scattering signature for very small particles. The polarization inside the particle is directly related to the *local electric-field enhancement* (FE) at the apex of the particle. For prolate particles this is given by:

$$\frac{|E_{\mathrm{loc}}|}{|E_{\mathrm{in}}|} = \left| \frac{\varepsilon}{\varepsilon_i + L_a(\varepsilon - \varepsilon_i)} \right|. \tag{3.6}$$

For vanishing denominators in Eqs. (3.2) and (3.6), a resonance of the polarization of the particle can occur. This condition fixes the singularity of Eqs. (3.2) and (3.6) in the complex ε plane, whereas the dielectric data of the material determines how close the material comes to this singularity (because $\text{Im}[\varepsilon] > 0$). Hence, the polarization remains finite for absorbing media.

The surrounding medium has $\text{Re}[\varepsilon_i] \geq 1$ in the majority of experiments. Therefore, $\text{Re}[\varepsilon] < 0$ is required in order to fulfill the resonance condition. Consequently, the material of the particle has to have a resonance in its (atomic) polarizability resulting in $\text{Re}[\varepsilon] < 0$, e.g. caused by the free electrons in metals or by phonons in polar crystals. In the case of metals these resonant collective charge oscillations in the particle are commonly referred to as *surface plasmon resonance (SPR)*.

The appealing simplicity of the equations above allows the investigation of the SPR for particles having a different (spheroidal) shape.
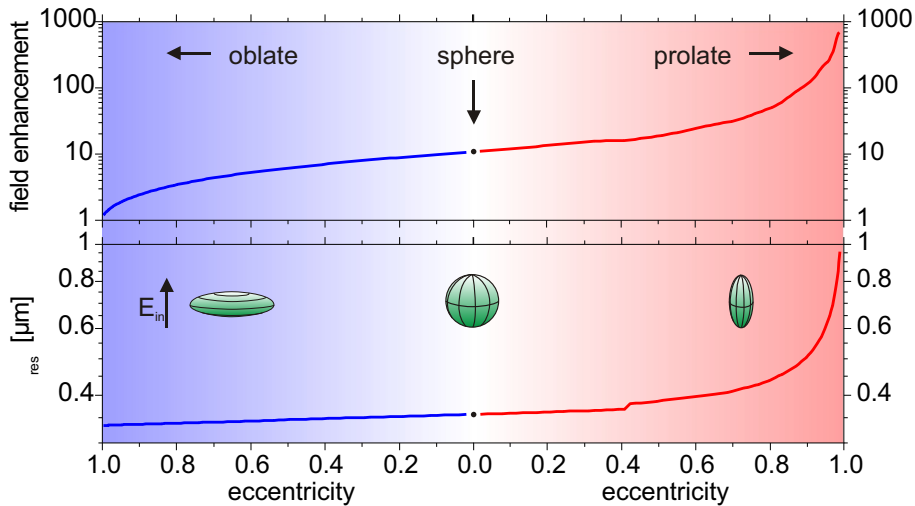
Figure 3.1 *Electric field enhancement and spectral position of the surface plasmon resonance (SPR) for a spheroidal silver particle in the electrostatic approximation as a function of the eccentricity e of the spheroid. The enhancement at the SPR increases strongly for elongated, prolate shapes and shifts towards longer wavelengths, whereas flattened, oblate shapes cause a blueshift and a reduction of the enhancement.*

The magnitude of the FE at the SPR as well as the spectral position of the SPR are displayed in Fig. 3.1 for a spheroid made of silver. A sphere ($a = b = c \ll \lambda$) shows a SPR at $\lambda = 357$ nm with roughly 11 times enhanced field according to the ε_{Ag} data from Ref. [45][1]. Stretching the sphere to a prolate shape causes an anisotropy of the polarizabilities along the short and long semiaxes. The SPR of the long axis is redshifted and the corresponding local electric field

---

[1]The magnitude and position of the SPR is extremely sensitive to the ε value assumed.

at the apex of the particle is strongly increased. The stronger FE originates from the larger absolute value of ε in the numerator of Eq. (3.6), the reduced damping in the red spectral region, and the smaller value of L_a. Both effects are reversed for flattened, oblate spheroid. The predictive power of the quasi-electrostatic model seems impressive. For instance, it predicts the huge field enhancement factors, which can explain the giant Raman enhancement factors reported [5]. The remaining question is: Does the electrostatic picture account for all effects that are present in a realistic experimental setup? What and where are the limitations of this model?

The stringent assumption of the model is the uniformity of the incident field across the particle, which can be violated in two ways:

- If the size of the particle is no longer small compared to λ, then the incident field for a given time varies across the particle.

- In the case of an inhomogeneous excitation (such as an evanescent wave), the incident field is nonuniform even for small particles.

Both points are interesting not only from an academic point of view. Nanoparticles made of various materials, such as Au, Pt, and polystyrene, are commercially available and the range of applications covers biosensors, chemical analysis, detection of ferroelectric polarization [46,47], and novel plasmonic bandstructures. The following examples have been realized during this thesis and give an introduction to the following chapters.

3.2   Surface plasmon resonance of gold nanospheres

Let us focus on the first point mentioned and look at the influence of the size of the nanoparticle on its spectral response. For the sake of simplicity, the gold spheres are assumed to be surrounded by vacuum and illuminated by a p-polarized plane wave as depicted in the inset of Fig. 3.2. Hence, the influence of a supporting substrate is neglected at the moment.

Using the wavelength-dependent data of the dielectric function of gold taken from Ref. [45], the local FE at nanospheres having various diameters d is displayed in Fig. 3.2. The value of the enhancement was determined by taking the local electric $|E_{\text{loc}}|$ at the outer top position at the sphere (as indicated by the arrow in the inset in Fig. 3.2) and normalizing it to the strength of the incident electric field $|E_{\text{in}}|$.

  For the smallest particles ($d \leq 30$ nm), the spectra in Fig. 3.2 reveal a maximum in the FE of somewhat more than 4.3 in the green spectral range around $\lambda = 520$ nm. The broad shoulder extending up to $\lambda = 650$ nm originates from the dielectric properties of gold. The internal damping mainly given by $\text{Im}[\varepsilon_{Au}]$, strongly decreases from $\text{Im}[\varepsilon_{Au}(\lambda = 310 \text{ nm})] = 7$ around the interband resonance of gold in the blue/ultraviolet spectral range to as little as $\text{Im}[\varepsilon_{Au}(\lambda = 650 \text{ nm})] = 1$. The nearly identical results for $d = 10$ nm of the numerical three-dimensional MMP simulation (red curve in Fig. 3.2) and the analytical electrostatic
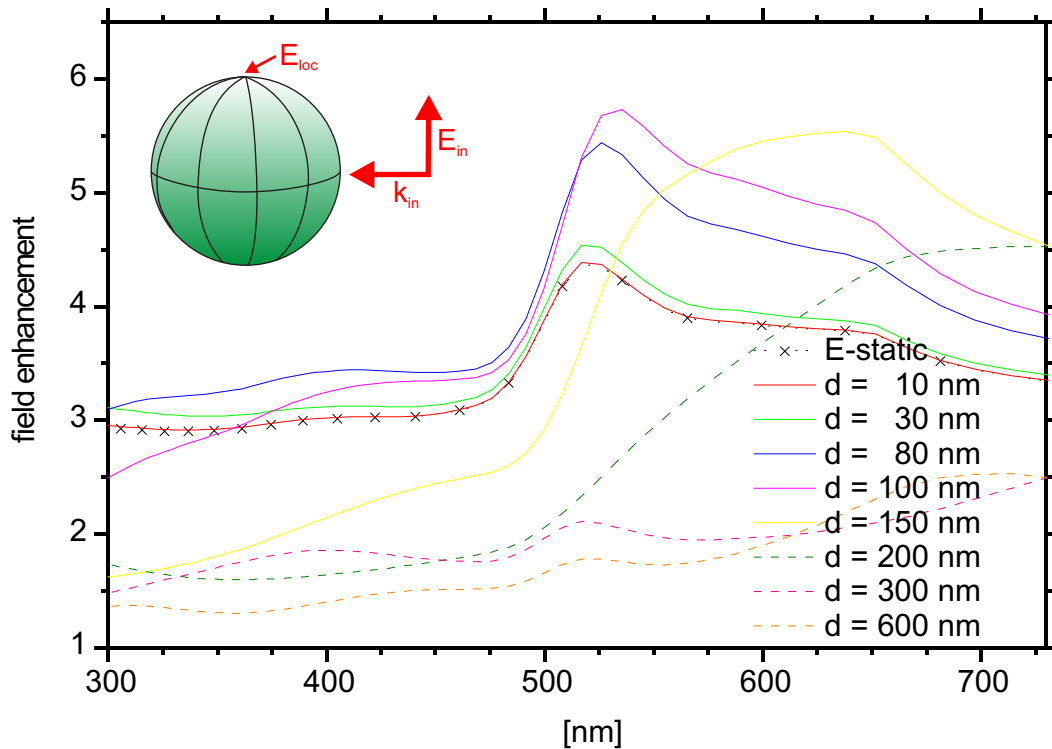
Figure 3.2   *The enhancement of the local electric field at a spherical gold nanoparticle caused by a SPR in the visible spectral range. The SPR for particles which are not very small compared to λ, e.g. $d = 80$ and 100 nm, is slightly redshifted and stronger than predicted by the quasi-electrostatic model (marked by the $\times$), which accurately describes smaller particles, such as $d = 10$ nm. The SPR strongly redshifts for $d > 100$ nm, while for $d > 200$ nm additional resonances occur, but the maximum field decreases.*

approximation (black dotted line with crosses) underline the validity of the latter in the small-particle limit.

Moving to slightly larger particles causes the SPR to become slightly redshifted and the FE to increase, which cannot be accounted for in the electrostatic limit because of the lack of a characteristic length scale in that description. However, the qualitative results still remain valid up to $d \simeq 100$ nm. The reason for this correspondence becomes clear when looking at the $|E|$ field pattern displayed in Fig. 3.3 (a). The incident electric field causes a dipolar polarization for small particles which is easily understood in electrostatics theory. The $|E|$ field patterns for $d = 150$ nm and $d = 300$ nm shown in Fig. 3.3 (b) and (c) deviate from a purely dipolar response, exhibiting an increasing asymmetry between the forward and backward scattered light for larger particles. The dipolar mode redshifts strongly for increasing d and for spheres having $d > 200$ nm it is outside the range plotted in Fig. 3.2. The additional small
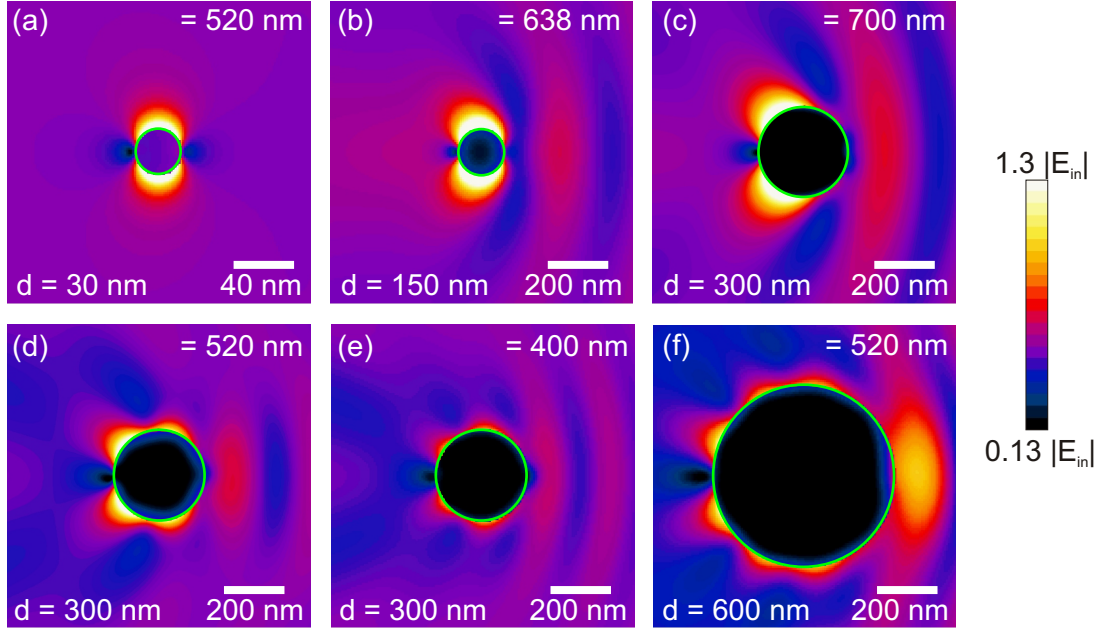
Figure 3.3   *(a) The |E| pattern for small ($\ll \lambda$) gold spheres shows mainly a dipolar polarization of the particle. (b)...(f) For larger particles, the increased retardation causes a dephasing and the excitation of higher-order modes.*

resonances can be associated with higher-order modes as displayed in Fig. 3.3 (d)-(f) but the gain of the electric field is much less compared to smaller particles[2]. These deviations from the electrostatic result for small particles can be treated analytically by Mie's theory [39] instead of electrostatics. Since a multipole in MMP is nothing else than a multipolar expansion in Mie's theory, the results of the corresponding Mie calculation are not explicitly shown.

3.3   Silver ellipsoid in an evanescent field

The optical response under inhomogeneous excitation will now be illustrated for an ellipsoidal silver particle. The inhomogeneous illumination can easily be achieved by illuminating a glass/vacuum interface from the glass side and choosing an angle of incidence larger than the critical one. Hence, the p-polarized plane wave, whose incidence angle is assumed to be $45°$, is totally internally reflected into the glass ($\varepsilon_{\text{glass}} = 2.25$) and an evanescent wave is created at the surface in the vacuum half-space. This electromagnetic wave decays exponentially normal to the interface. The decay constant $k_\perp$ can be adjusted by changing the angle of incidence ϕ through $k_\perp = \sqrt{k_0^2 - k_\parallel(\phi)^2}$, with $k_0 = \frac{2\pi}{\lambda}$. For example, the intensity of the evanescent wave

---

[2]The fact that the point where E_{loc} is determined is kept fixed may influence the value of the FE because of the different $|E|$ field pattern of the modes. Therefore, the maximum of the field for higher modes can be slightly larger than plotted in Fig. 3.2 while the overall spectrum will be almost unaffected.

at $\phi = 45°$ rapidly drops down (normal to the interface) to a $1/e$ value within $z_{1/e} \approx \frac{1}{4}\lambda$. The widely used excitation scheme drawn in Fig. 3.4 is known as the total-internal-reflection (TIR) method. The absence of propagating modes (from the excitation) in the upper vacuum half-space is advantageous from the experimental point of view in order to discriminate the scattered light from the incident. A silver ellipsoid placed in this evanescent field will sense
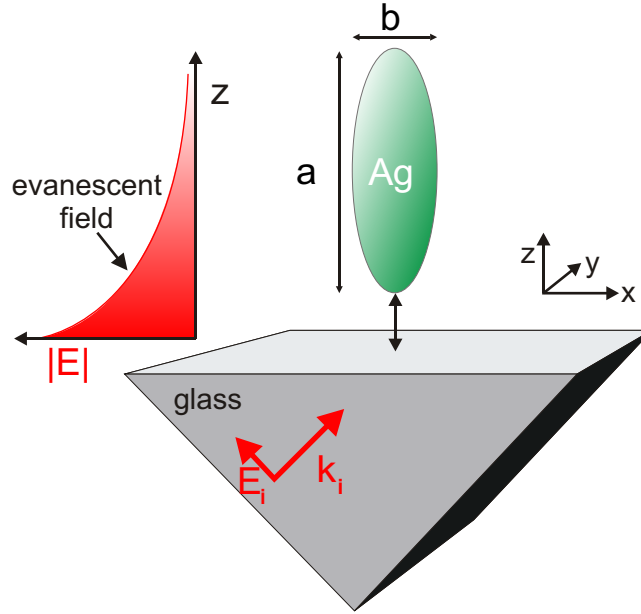
Figure 3.4 *Inhomogeneous particle illumination through evanescent optical fields. The p-polarized incident plane wave undergoes total internal reflection at the glass interface. Hence, k_z is purely imaginary in the upper half-space, corresponding to an evanescent wave. The silver ellipsoid senses this field by getting polarized. The interaction of the particle with the substrate is not accounted for in this section.*

this field and will become polarized. For the sake of simplicity, we start the calculation without accounting for the role of the interface (this task is postponed to a later chapter). Neglecting the influence of the interface corresponds to a setup in which the particle-interface separation Δ is large (but the particle still senses the evanescent field). In order to characterize the field enhancement produced by the particle, we normalize the electric-field amplitude at both ends of the ellipsoid to the exciting field E_0 present at the position of the front end when the particle is absent. In Fig. 3.5 these two normalized field amplitudes are plotted as a function of wavelength for different ellipsoid sizes with an axis ratio of 10:3 and a long axis of $a = 10$, 50, and 100 nm.

All field enhancement spectra show a strong resonance in the green or yellow spectral range which can be attributed to the excitation of a surface plasmon. The smallest particle (10 nm in length) exhibits the SPR between 514 and 528 nm. For particles which are much smaller
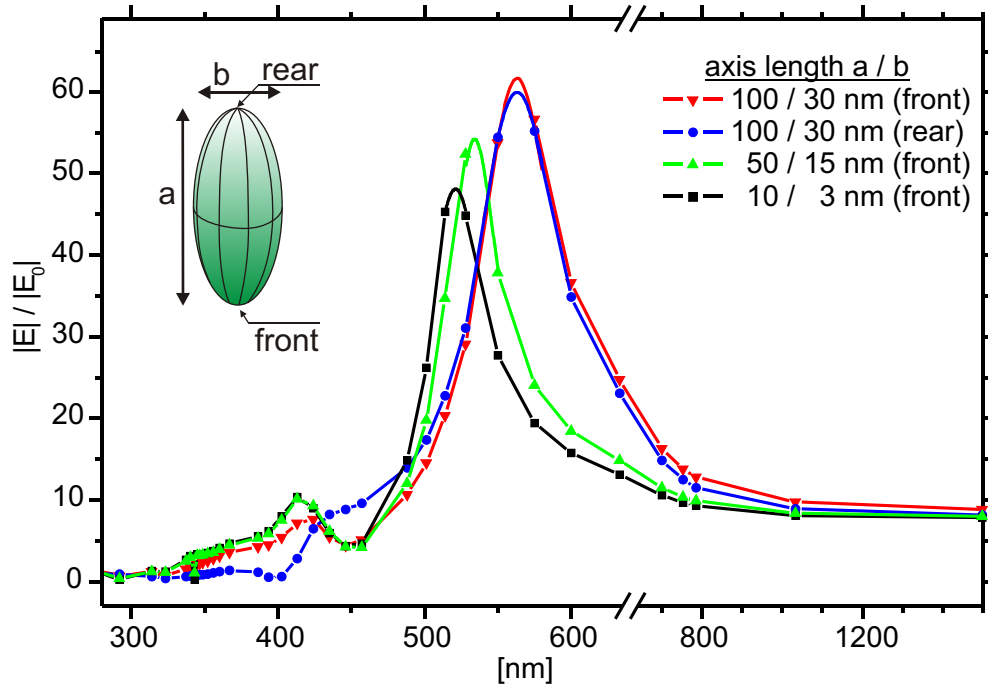
Figure 3.5 *Electric-field amplitude near the apex of a silver ellipsoid under evanescent excitation. For a larger particle size the strong dipole-like resonance shifts to longer wavelengths (redshift). Due to the less symmetric excitation a smaller second resonance shows up at 420 nm only at the front side of the particle. Conversely, the rear end shows a similar resonance at longer wavelengths indicated as a shoulder in the main resonance peak [48].*

than the wavelength, the electrostatic description [19, 44] is sufficient for finding the main resonance peak. For instance, for an ellipsoid with an axis ratio of 10:3 excited by an electric field parallel to its long axis, the electrostatic model predicts the resonance to occur at that specific frequency for which $\mathrm{Re}(\varepsilon_{\mathrm{res,long}}) = -9.48$, and the SPR for the mode parallel to the short axis at $\mathrm{Re}(\varepsilon_{\mathrm{res,short}}) = -1.21$. Using the dielectric properties of silver published by Palik [49], we obtain resonance wavelengths of ≈ 525 nm and ≈ 340 nm, respectively. The very pronounced SPR along the larger ellipsoid axis dominates the spectral response, whereas the mode parallel to the short axis around 340 nm does not give rise to any maximum because of the field distribution (strongest field along the short semiaxis of the particle and not at the sharp apex on the long semiaxis). The excellent agreement between the MMP simulation and the analytical electrostatic solution confirms the coincidence of both descriptions for particles which are small compared to the wavelength.

The spectral response of the larger two particles, shown in Fig. 3.5 is much more difficult to describe analytically [50], as the electrostatic picture does not apply. This fact manifests itself by a redshift of the strong resonance peak by as much as 40 nm in our MMP calculation.
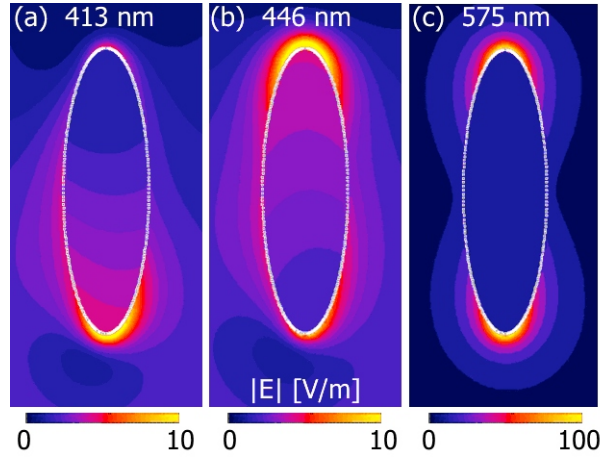
Figure 3.6   *Electric-field amplitude pattern for a silver ellipsoid with an axis ratio of 100 nm : 30 nm illuminated by an evanescent wave at different wavelengths. At 575 nm (c) the polarization inside the particle is nearly homogeneous and it scatters like a dipole. Due to the evanescent field, a second mode is excited at shorter wavelengths with the electric field concentrated either at the front (a) or rear (b) end of the ellipsoid.*

Taking a closer look at the spectral responses in Fig. 3.5, we find a second less pronounced maximum around 420 nm. This resonance can be attributed to a higher-order resonance excited by the evanescent field. In contrast to plane waves, the rapidly decaying field has a lower symmetry and is able to excite higher-order modes in the particle. Fig. 3.6 displays the significant difference between this mode and the formerly mentioned surface plasmon mode in which the whole particle is homogenously polarized. For this higher-order mode, the electric field is mostly concentrated to the front end of the particle, while it is much weaker at the rear end. Conversely, there is a similar resonance for which the field is strongest at the rear end. That resonance occurs at a larger wavelength of 446 nm for a 100-nm-long ellipsoid and is superimposed to the main SPR as a shoulder shown in Fig. 3.5. Note that all fields are normalized to the same undisturbed field amplitude $|E_0|$ as introduced earlier.

For wavelengths larger than the main SPR, the field pattern is similar to Fig. 3.6 (c) but weaker in intensity. Hence, for $\lambda \geq \lambda_{\mathrm{res}}$ the particle can be treated as an oscillating dipole.

Before summarizing, it is worth while observing the strength of the higher-order mode. The field gradient normal to the interface can easily be increased by choosing a larger angle of incidence (see p. 18), which makes the excitation of the higher-order mode more efficient. As a recalculation of the spectra revealed (data not shown), the strength of this mode also strongly increases if one introduces a (fictitious) reduced damping ($\mathrm{Im}[\varepsilon]$) of the optical response of the particle.

3.4   Summary: validity of the quasi-electrostatic description

The results presented in the last two sections illustrate the SPR, which constitutes a resonance of the polarizability of the nanoparticle. The nonuniform spectral behavior has to be accounted for in the interpretation of measurements which are sensitive to the local electric field, such as an experiment by Wokaun *et al.* on Raman scattering [51], the observation of photoluminescence mediated by two-photon absorption at nanoparticles by Beversluis/Bouhelier *et al.* [52,53], or the investigation of second-harmonic generation from nanoparticles by Antoine *et al.* [54]. Hence, adjusting the spectral position of the SPR by properly choosing the material (thereby $\varepsilon(\lambda)$), the geometrical shape, and the size opens the door to increased sensitivity. The SPR of nanoparticles can be understood within a simple quasi-electrostatic model. That is because the strong SPR modes are dipolar excitations by nature, and higher-order modes are more strongly affected by the increased damping at frequencies closer to the plasma frequency. Therefore, the main trend is qualitatively well reproduced by this simple model, but one should always remember its limitations:

- *Size effects* that occur when the characteristic length L of the particle is no more small compared to λ. As long as $L \leq \lambda/20$, the predictions of the electrostatic model are accurate. For particles with $L < \lambda/2$, the SPR is redshifted compared to the simple model. Because of the presence of geometrical resonances, larger particles ($L > \lambda/2$) behave completely differently.

- *Inhomogeneous excitation* created by strongly decaying fields, e.g. evanescent waves or dipolar fields, causes the excitation of higher-order modes even in small particles. The quasi-electrostatic model corresponds to a dipolar approximation. This is often sufficient, but every electromagnetic field having non-vanishing higher-order spatial derivatives of the intensity couples to higher order modes in the particle [18].

For the sake of completeness, a few remarks concerning very small particles are necessary. In that case, additional damping mechanisms contribute, namely the scattering of the oscillating electrons at the surface and quantum finite-size effects. If the diameter of the nanoparticles is in the order of the free path length of the electrons, the surface scattering increases the dissipation inside the material, which is otherwise dominated by electron-electron scattering [55]. First steps to clarify the role of quantum finite-size effects were presented recently, using the time-dependent local-density approximation [56] to treat only the conduction electrons quantum-mechanically and the rest classically. Both effects are not accounted for by the dielectric constants of the bulk material. Therefore, the intrinsic damping may be larger for particles smaller than 10 nm, as reported in Ref. [57–59]. However, these experiments have to be carried out and analyzed very carefully because other effects might easily hide these contributions, such as small variations of the shape, a coupling to neighboring nanoparticles, or substrate effects as will be discussed in the next two chapters.

Chapter 4

Electromagnetic interaction of nanoparticles

The aim of this chapter is to shed some light on the basic mechanism of near-field coupling by investigating special cases rather than to present a complete treatment of the huge field of electromagnetic interacting nanoparticles. The investigation presented in this work was motivated by experimental studies. Commercially available gold nanoparticles are used mainly because of practical reasons of long-term stability. The gold spheres are chemically inert, unlike silver which easily reacts with sulphur. Unfortunately, the price for the lower reactivity is a stronger damping in Au compared to Ag in the visible spectral range. The results of the previous chapter indicate that a reasonably large enhancement by a SPR can only be achieved with sphere diameters below 150 nm. Therefore, the following investigation has been limited to spheres having $d = 10, 30,$ and 80 nm.

Ferreting out highly confined, strongly enhanced electromagnetic fields has been the scope of numerous studies. But from a practical point of view, optimizing the shape and material of single nanoparticles is restricted to a few experimentally realizable structures. Another road to enhanced electric fields has already been marked in the literature: Placing several interacting nanoparticles close together can greatly increase the local electric field strength. Such structures have mostly been used as SERS substrates and may be produced in a more or less controlled way by thermal treatment [60] or in a much more well-defined way by means of electron beam lithography (EBL) of thin metal films. This tool allows the nanopatterning of two-dimensional structures having geometrical features down to some tens of nanometers. The interaction between pairs [61–63] as well as arrays [64, 65] of EBL-produced cylinders has been studied both by measuring the Raman enhancement [64–66] and by analyzing the scattered or absorbed light [61, 62, 67]. The interaction has been modelled by investigating a simpler two-dimensional system consisting of a pair of cylinders [68, 69] or pairs/arrays of spheroids [62, 65, 70, 71] and a strong radiative or near-field coupling has been found, depending on the separation and polarization.

Other groups looked closer at the energy transport and dispersion in chains of nanoparti-
cles (plasmon wire) [72, 73, and references therein] and tee-structures/junctions made up of
nanoparticle chains [74]. All of these studies reveal that the two different eigenmodes behave
differently when the sub-λ separation between neighboring particles is reduced. More pre-
cisely, the transverse modes, in which the individual particles are polarized perpendicularly to
the chain axis, show a blueshift for smaller spacing, whereas the longitudinal mode (particles
polarized along the chain axis) is shifted to lower energies (redshift) [73]. The numerical simu-
lation in Ref. [75] clearly shows that the nearest-neighbor interaction dominates the response
of the chain.

Li *et al.* [76] picked up the idea of sub-λ light guiding of the longitudinal mode and proposed
an "efficient nanolens consisting of a linear self-similar chain of metallic nanoparticles". In
such an arrangement, the field is enhanced at the first sphere, leading to an enhanced exci-
tation of the second particle, which excites the third sphere. Therefore, the surface plasmon
resonators are successively fed, which results in a very high field (hot spot) between the two
last particles. Hence, such structures would feature an enormous Raman enhancement, which
could make them attractive for single-molecule detection.

4.1   Optical properties of gold dimers

Placing two identical spheres close to each other is maybe the simplest nontrivial problem
and should be discussed at the beginning. Before presenting the results of the rigorous
3D calculation, let us discuss the electrodynamic problem qualitatively in the limiting but
illustrative case that the particles are small.
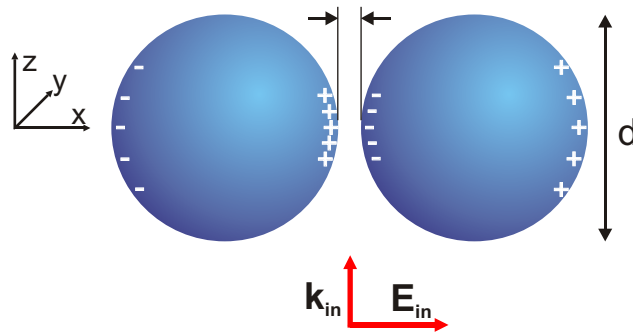
Figure 4.1   *Illuminating two spheres which are separated by a small gap leads to a strong
near-field interaction because of the oscillating surface charges induced on the spheres. The
surface charges are sketched for one point in time.*

We consider an arrangement as depicted in Fig. 4.1, with the chain axis of the two small

spheres parallel to the incident electric field $\boldsymbol{E}_{\mathrm{in}}$. The incident plane wave induces an oscillating polarization in both particles. The particles are polarized in the same manner, which leads to opposite surface charges at both spheres inside the gap as sketched in Fig. 4.1 for a certain point in time. Hence, two surface charges with opposite signs, located at a short distance to each other, produce a strong field. Depending on the ratio of the gap width to the sphere radius, the strong near-field interaction does not only increase the local electric field in the gap but may also alter the spectral response of the dimer compared to an isolated particle.

4.1.1 Two identical spheres

The system under inspection consists of two spheres having equal diameters d and a fixed separation of $\Delta = 5$ nm. Figure 4.2 displays the local electric-field enhancement (FE) for different values of d of $10, 30,$ and 80 nm. The values of the FE were taken at the surface
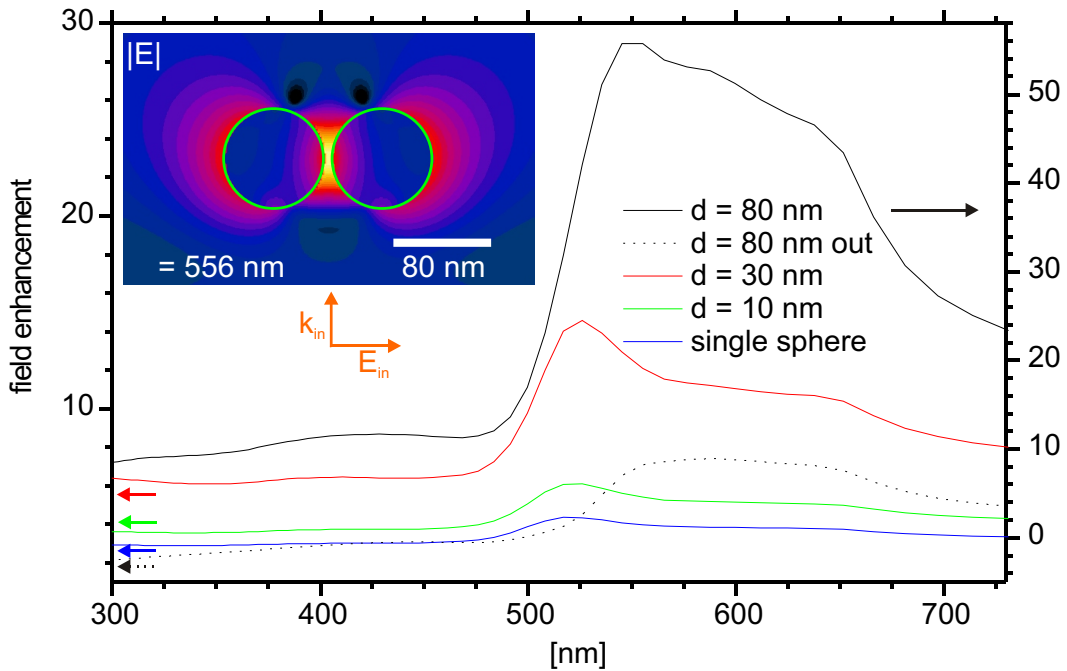
Figure 4.2 *The strong near-field interaction of two identical gold spheres with a diameter of 80, 30, and 10 nm separated by a gap of 5 nm leads to a high concentration of oppositely signed charges on the two surfaces facing each other. Hence, $|\boldsymbol{E}|$ can be much stronger between the spheres than at a single sphere. The highest field is found for $d = 80$ nm because of the stronger polarization for larger particles. The inset shows the $|\boldsymbol{E}|$ pattern for 80-nm spheres at the SPR ($\lambda = 556$ nm) in the xz plane. The color scale is logarithmic with successive colors differing by a factor of 1.2 in the $|\boldsymbol{E}|$ field.*

of the sphere on the chain axis (x axis). The maxima of the FE are equal at both particles
because of the symmetry of the problem.

Taking a closer look at the spectra of a single sphere (blue curve, of Fig. 3.2) and of a pair of
spheres with $d = 80$ nm (Fig. 4.2), one finds a clear difference in shape. In the pair case, the
SPR is redshifted by approx. 25 nm because of the stronger near-field interaction at the inner
point whereas at the outer point (black dotted curve) only a very broad maximum around
590 nm is found. For smaller particles ($d = 30$, and 10 nm), this effect was not found, which
underlines that the strength of the near-field interaction increases strongly for very closely
arranged particles. The important parameter is the ratio of separation to radius and not just
the separation.

4.1.2   Two differently sized spheres

Replacing the second sphere by a smaller one breaks the symmetry of the arrangement. Hence,
the electromagnetic field becomes asymmetric as shown by the $|E|$ field pattern in Fig. 4.3.
The graph displays the results for two spheres with $d_1 = 80$ nm and $d_2 = 30$ nm separated
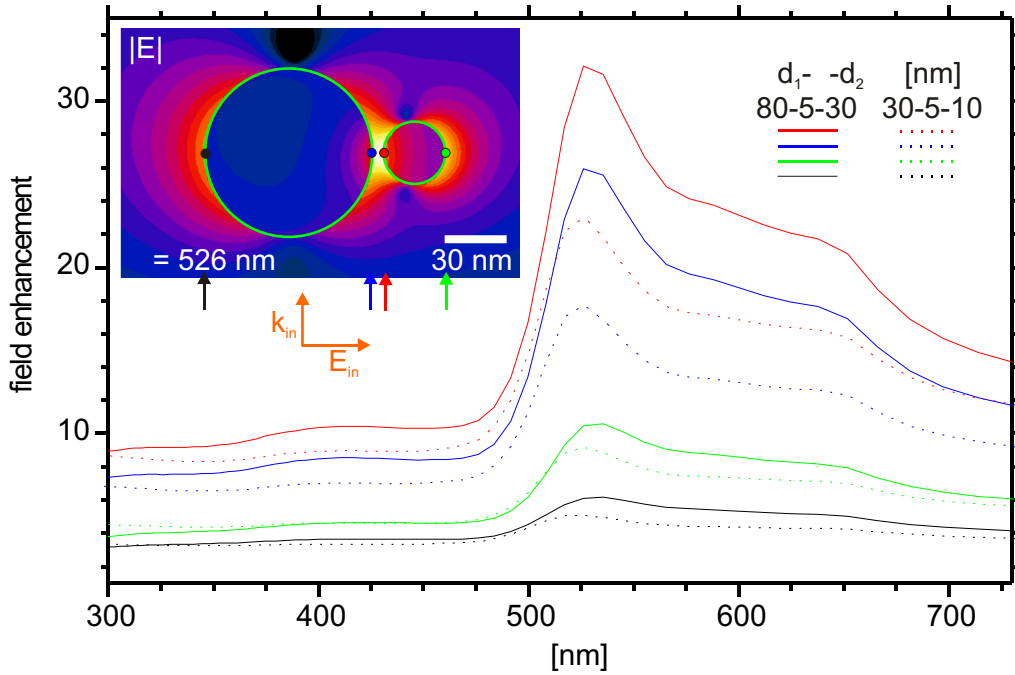
Figure 4.3   *Spectra of the FE of a gold dimer having $d_1 = 80$ nm, $d_2 = 30$ nm, $\Delta = 5$ nm,
as well as for $d_1 = 30$ nm, $d_2 = 10$ nm, and $\Delta = 2$ nm. The colors of the curves and the
marked points in the inset indicate the locations where the FE was determined. The highest
field is situated inside the gap at the surface of the smaller sphere. Successive colors differ by
a factor of 1.2 in the logarithmic $|\boldsymbol{E}|$ pattern.*

by a $\Delta = 5$ nm gap and for another pair of spheres shrinked by factor $\approx 0.33\ldots0.4$, having $d_1 = 30$ nm, $d_2 = 10$ nm, and $\Delta = 2$ nm. The different colors refer to the four locations along the chain axis where the FE is recorded (they are indicated in the $|E|$ inset, too).

Because of the smaller radius of curvature, the FE is now highest at the surface of the smaller sphere, but the absolute value of the FE is less than for the 80-5-80-nm arrangement in Fig. 4.2. This is most probably because of the fewer surface charges at smaller spheres compared to larger ones. The outer points on the dimer (marked by black and green) are not subject to such strong near-field interaction. Hence, the amplitude of the FE is significantly smaller than inside the gap.

Since also the gap width Δ was reduced in proportion, the spectra of the nanodimers having $d_1 = 80$ nm, $d_2 = 30$ nm, and $d_1 = 30$ nm, $d_2 = 10$ nm, respectively, are qualitatively identical in respect to their shape, as one would expect in the quasi-electrostatic model.

4.1.3 Experimental preparation of gold dimers

Depositing nanoparticles only a few nanometers away from each other seemed to be a rather complicated task. A direct deposition of the clusters is beyond the capabilities of today's standard scanning probe setups. Therefore, techniques relying on the occasional self-arrangement were used in order to "arrange"the dimers (for details see Ref. [77] and references therein). The gap width Δ was controlled via an additional spacer layer covering the gold clusters, consisting of alkane thiols ($C_{22}H_{45}SH$) as sketched in Fig. 4.4. The thiol ($S-H$) group
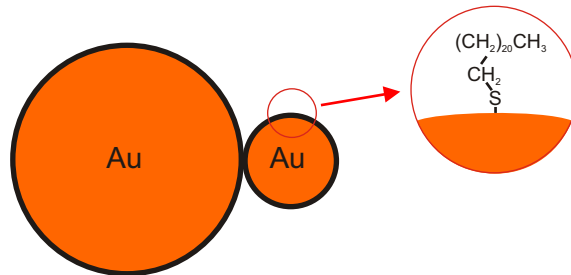
Figure 4.4 *The alkane thiol forms a self-assembled monolayer in the trans conformation around the gold spheres. The thickness of the layer is defined by the number of $-CH_2-$ groups. The two spheres are separated by the docosanethiol layers by $2\cdot 3$ nm.*

binds strongly to the gold surface of the nanoparticle by forming a covalent metal-sulphur bond. The molecules form a well ordered self-assembled monolayer in which they stand almost upright. The thickness of this layer can therefore be controlled by changing the number of $-CH_2-$ groups of the alkane. The commercially available aqueous gold particle suspension was added to a solution of this alkane and ethanol (for further details see Ref. [77]). The formation of the metal-thiol complex is nearly finished after 24 hours. After this pretreatment
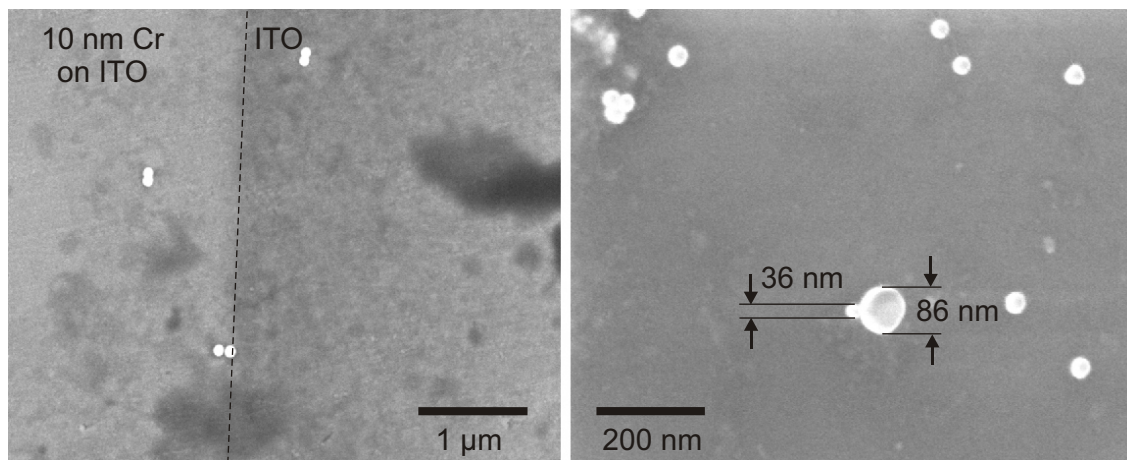
Figure 4.5 *SEM images of gold dimers. (left) Dimers made up of 80-nm clusters deposited onto a bare or Cr-covered ITO substrate to ensure electrical conductivity. (right) A dimer consisting of 30-and 80-nm spheres (courtesy of J. Seidel).*

the dispersion of gold clusters with $d = 30$ nm and $d = 80$ nm was spin-coated onto the substrate once or twice. The dimers arranged themselves by chance and were then inspected by means of a scanning-electron microscope (SEM). In order to prevent charging of the clusters by the electrons and to avoid the associated blurring in the high-resolution SEM pictures, conductive substrates are necessary. Optically transparent indium tin oxide (ITO) or a thin layer of chromium [78] deposited onto glass are typically used. The result of such a screening is displayed in Fig. 4.5.   Raman spectroscopy of suitable test molecules may serve to probe the near field of the field-enhancing metal structure. The intensity of Raman-shifted light scattered by molecules situated close to the metal structure is a direct measure of field enhancement and shows a fourth-power dependence on the enhancement factor. In the present case, the thiol molecules acting as the spacer layer between the clusters may simultaneously serve as Raman-active probe molecules. In this way the field in the gap region between the clusters, where the strongest field is expected, can be probed.

The Raman activity of the thiol layer is clearly confirmed by a spectral analysis of the light scattered by the thiol-coated clusters. The measurement (Fig. 4.6) was performed with a confocal optical microscope coupled to a grating spectrometer. Light from a single-mode frequency-doubled Nd:YAG laser with a wavelength of $\lambda = 532$ nm was focused through a high-numerical-aperture oil-immersion objective onto a single cluster, and the scattered light collected by the same objective was sent to the spectrometer. A notch filter suppressed the Rayleigh-scattered light by six orders of magnitude. In the case of bare gold clusters only Raman lines originating from the immersion oil were observed, whereas spectra taken on thiol-coated gold clusters showed a number of additional well resolved lines, which can be
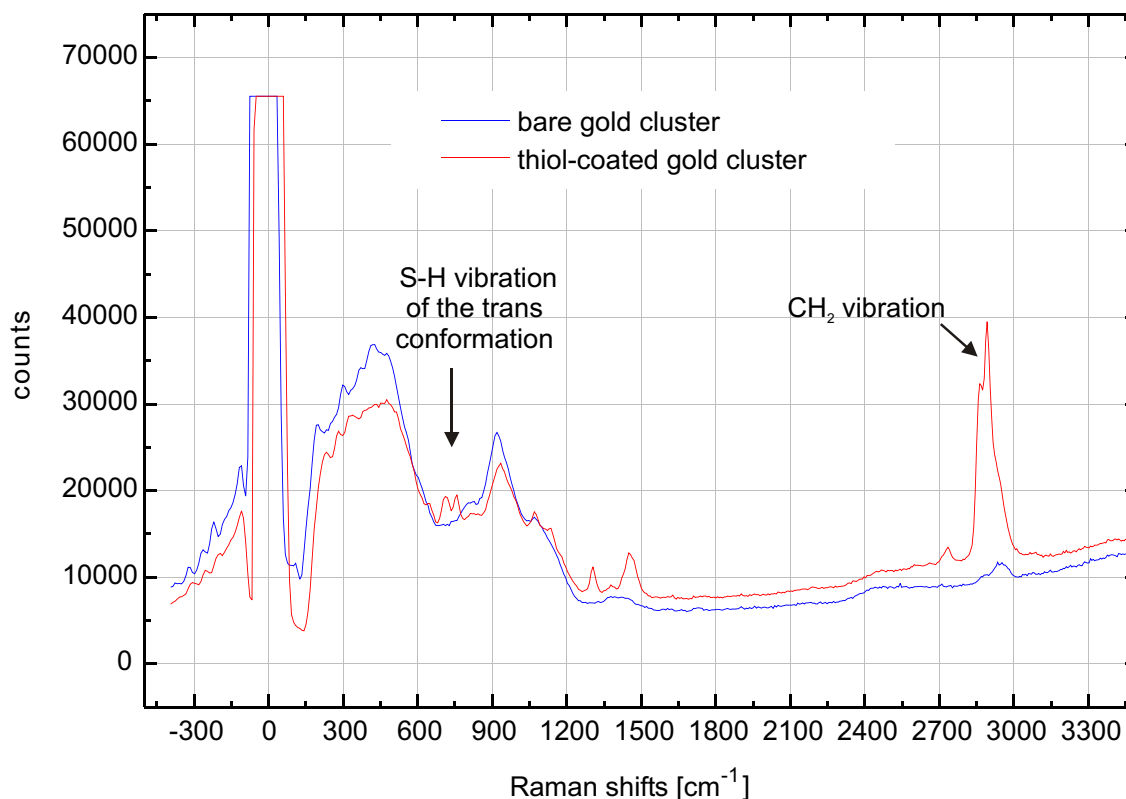
Figure 4.6 *Raman spectra taken on a bare and a thiol-coated gold cluster, respectively. Without the thiol layer, only lines originating from the immersion oil are observed. The strong line around zero is caused by Rayleigh-scattered light which is not completely suppressed by the notch filter. (courtesy of R. Lettow)*

attributed to various vibronic modes of the hydrocarbon chain (around 2900 cm^{-1}) and the end groups of the thiol molecule (around 750 cm^{-1}) as shown in Fig. 4.6.

Furthermore, first attempts were made to measure Raman spectra originating from dimers of thiol-coated clusters. At present, the Raman data are still to scarce to draw any quantitative conclusions, but the work is continued at the TU Dresden.

Another tricky possibility to study the dynamics of cluster dimers experimentally was reported by the group of Sandoghdar [80]. They "simply"glued a single gold cluster to the apex of a glass fiber tip of their SNOM setup. The second cluster was deposited on the substrate and illuminated. The inter-particle distance and therewith the strength of interaction was controlled by scanning the SNOM tip while the scattered light was analyzed.

4.2   Optical properties of gold trimers (snowman)

After studying the dimer system in detail, we turn our attention to the setup mentioned in
the introduction of this chapter, which is also displayed in Fig. 4.7.

The third sphere added to the dimer is placed in close proximity to the second one. Therefore,
this additional particle is subject to the enhanced near field of the dimer and should further
gain in enhancement. This idea can be extended to even larger systems by adding additional
particles to further super-focus/confine the light, theoretically.
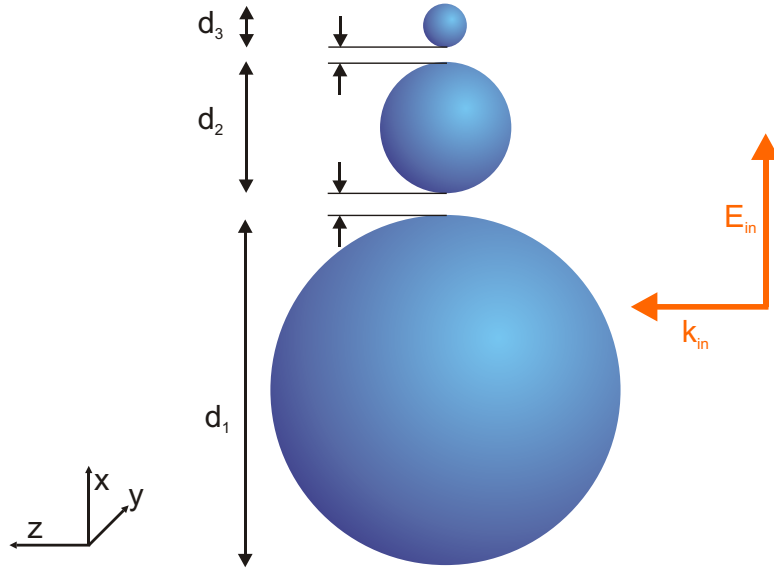
Figure 4.7 *Closely packed triple-sphere setup (snowman).*

Reality is often more complex than expected at the first glance, particulary when one has
simple pictures in mind. The first system which we analyze consists of three spheres having
$d_1 = 80$ nm, $d_2 = 30$ nm, and $d_3 = 10$ nm, separated by equal gaps with $\Delta_1 = \Delta_2 = 5$ nm.
The solid curves in Fig. 4.8 display the value of the FE at 6 different locations along the chain
axis. The highest value can be found between the largest and the medium-sized particles
at the surface of the latter (red curve). The magnitude $(32 \times |E_{in}|)$ and spectral position
$(\lambda = 526$ nm$)$ is identical to those found in the dimer system (see: $d_1 - \Delta - d_2 : 80 - 5 - 30$ nm
in Fig. 4.2). Between the medium and smallest spheres the FE is less than 24.

After this disillusioning result for the snowman having two equal gaps, the calculation was
repeated assuming a reduced second gap $\Delta_2 = 2$ nm. This reduction indeed follows the idea
proposed by Li et al. [76] of building a self-similar chain. The second gap was scaled according
to $\Delta_2 = \kappa \Delta_1$ with $\kappa = d_2/d_1$ and rounded to 2 nm. The plots of the spectral dependence of
the FE are displayed in the same Fig. 4.8 but marked as dotted lines.

The reduction of the second gap causes the electric field to become strongest in this gap at
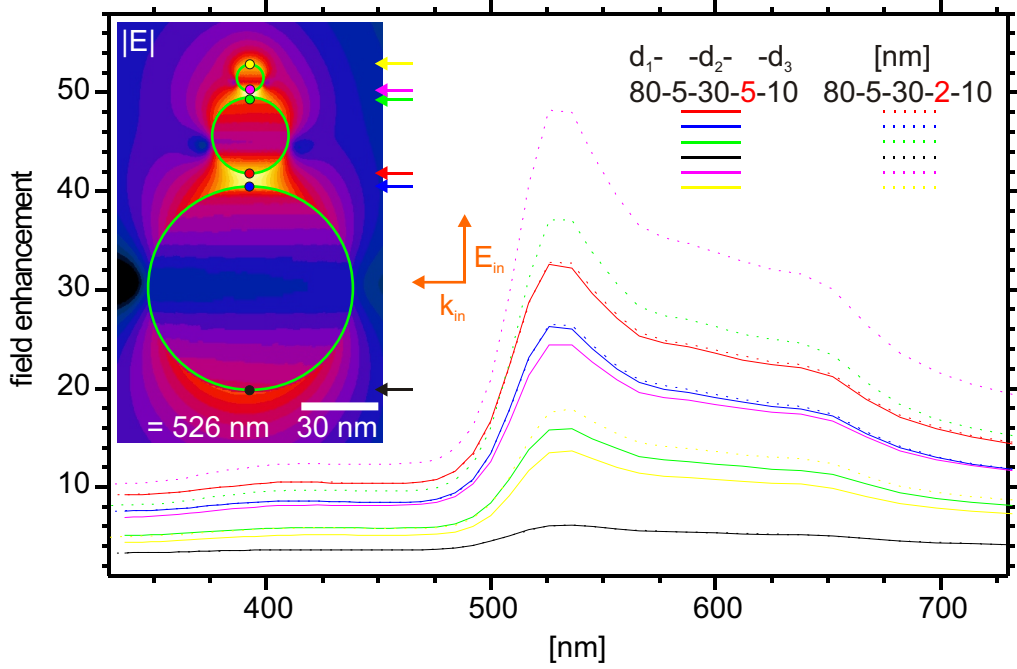
Figure 4.8 *Local electric field at a snowman structure having two equal gaps ($\Delta_1 = \Delta_2 = 5$ nm - solid curves) as well as for a self-similar arrangement ($\Delta_1 = 5$ nm, $\Delta_2 = 2$ nm - dotted curves). The colors of the curves and the marked points in the inset indicate the locations where the FE was determined. The highest field is located between the largest and medium-sized spheres with a maximum close to the middle sphere in the case $\Delta_1 = \Delta_2 = 5$ nm. Reducing the second gap to $\Delta_2 = 2$ nm results in FE of up to 48 inside the smaller gap. The inset displays the $|\boldsymbol{E}|$ field at the sphere surfaces and in the xz plane. Successive colors differ by a factor of 1.2.*

the surface of the smallest sphere. The enhancement is roughly 48. Comparison of this value to the result for the dimer having $d_1 - \Delta - d_2 = 30 - 2 - 10$ nm (see Fig. 4.3) suggests that the "feeding" by the largest sphere produces an additional yield of roughly 2. Or in other words, the presence of the large 80-nm sphere doubles the local field. The $|E|$ field pattern of the self-similar arrangement is displayed as an inset in Fig. 4.8. The $|E|$ field at the sphere surfaces and in the xz plane is plotted in contrast to the previous figures, which show the field in the xz plane only. Because the field is mostly concentrated inside the gap between the spheres and not at the outer positions, such a configuration would not be very suitable as a local probe for scanning near-field optical microscopy, unfortunately. Nevertheless, it might be a very promising approach for chemical sensing of nanosized volumes and increase the sensitivity towards single-molecule detection.

The value of the maximum FE of 48 is much smaller than the value of 600-1300 reported in Ref. [76] for a snowman structure made of silver having $\kappa = 0.3$. This large difference

originates mainly from the much lower internal damping of silver in comparison to gold leading to a much sharper and stronger SPR. The FE produced by a single silver sphere is roughly three times higher than the one of a gold particle even in the small-particle limit. Another difference to the calculation in Ref. [76] is that all the results presented in this chapter account for retardation, whereas Li et al. used electrostatics and dipolar excitation only.

4.3   Summary: coupled nanoparticles

In conclusion, the coupling of individual surface plasmon resonators by the near-field interaction of the surface charges can be used to create strongly confined and enhanced fields on the nanometer scale. Focusing the field at the smallest sphere is not realizable with equal separations between the particles in a chain of particles having successively decreasing diameters. A smaller volume causes a reduced polarizability, which has to be compensated by a stronger near-field interaction - this requires a reduced separation. The scaling may be chosen to be self-similar but this is not a necessary requirement.

Chapter 5

Tip-sample interaction

In this chapter, the interaction of light with the coupled system consisting of a nanoparticle that is placed very close to a planar substrate is investigated. The analysis of both a particle excited at or close by to its SPR frequency and a resonance of the system residing in the substrate highlights the basic effects resulting from the near-field interaction of the system. The main emphasis is directed to the impact of this model of the tip-sample interaction on near-field optical microscopy in the visible and infrared spectral region.

The SPR of nanoparticles and therewith the associated highly confined field can be used to create an optical source for scanning probe microscopy. These tools open the door to a resolution well below the classical optical diffraction limit. Therefore, the electromagnetic field distribution in close proximity to an illuminated object plays a key role in scanning near-field optical microscopy (SNOM) and in novel plasmonic devices. SNOM pushes the resolution in optical microscopy beyond the diffraction limit by probing the near field rather than record-
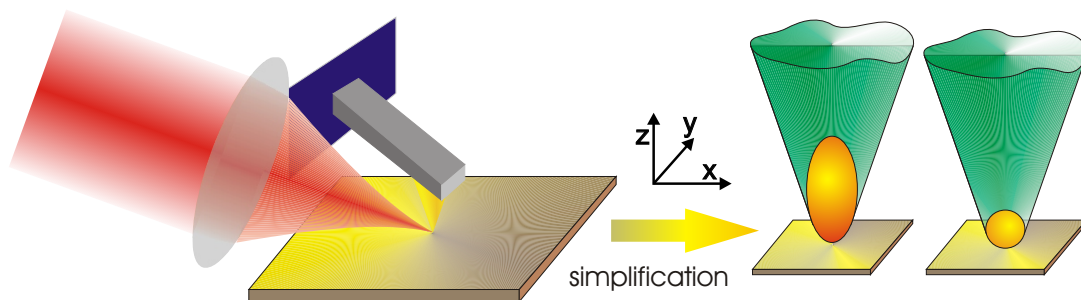

Figure 5.1 *In a typical scattering-type SNOM the focused laser light is scattered at the apex of a sharp tip, creating a strong and locally confined optical source. The scattering signature of such a system is commonly investigated in the limit of an ellipsoid or sphere replacing the massive tip.*

ing a conventional far-field image. In one specific version of SNOM, known as scattering-type SNOM (s-SNOM) [6–8, 81], probing is realized by scattering the near field at a sharp dielectric [81] or metallic [6–8] tip (see Fig. 5.1), or with a metallic nanoparticle [82]. The particularly attractive feature of this approach is that a strong field enhancement is achieved at the apex due to both the pointed tip geometry (lightning rod effect) and the excitation of plasmons in the metal. This technique has been successfully applied to both scanning near-field infrared spectroscopy [83] and scanning near-field Raman spectroscopy, also known as tip-enhanced Raman spectroscopy (TERS) [41, 42, 60, 84, 85]. The latter method is related to surface-enhanced Raman spectroscopy (SERS), which makes use of the field enhancement at rough metal surfaces [3, 4]. In contrast to SERS, TERS offers high spatial resolution with well defined excitation by the highly localized field at the tip. Especially noble-metal nanoparticles show strong plasmonic resonances in the visible range. This spectrally nonuniform behavior has to be considered when experimental data obtained with surface- or tip-enhanced techniques such as SERS and TERS, or with techniques that are sensitive to the electric field strength such as second harmonic generation [86] are interpreted. Beside massive metallic tips, also dielectric tips and metal-coated aperture-SNOM probes carrying a small metallic particle have been investigated recently, see [82, 87, 88] and [89, 90], respectively. Such an arrangement features a stronger surface plasmon resonance compared to solid metal tips as well as increased field enhancement [91] and resolution.

One question remaining is: How does the sample influence the response of the tip or single particle and, hence, the observable signal. One of the simplest and historically first approaches was again the application of the quasi-electrostatic dipole model [18], which can account for the tip-sample interaction by assuming an effective polarizability α_{eff} rather than the polarizability α of a pure particle. In the vicinity of an interface, the dipole field generated by the particle is reflected and reinteracts with the sphere. In the quasi-electrostatic approach, the whole polarizable particle is replaced by the corresponding dipole located at the center of the particle and the coupled system is described by the superposition of this original dipole field and the field from its image dipole located in the substrate. The latter changes the local field at the position of the particle dipole, thereby modifying its dipole moment. The total field radiated to the far-field can be attributed to the total dipole moment made up of the particle and its image charge distribution. The result can conveniently be written in terms of α_{eff} connecting the total dipole moment of the probe-sample system to the exciting field $\boldsymbol{E}_{\text{in}}$. The effective polarizability tensor α_{eff} is diagonal in the principal axis system for particles being rotational symmetric perpendicular to the interface. The tensor elements normal and parallel to the interface are:

$$\alpha_{\text{eff,zz}} = \frac{\alpha(1+\beta)}{1 - \frac{\alpha\beta}{16\pi h^3}} = \alpha_{\text{eff,z}}, \quad \alpha_{\text{eff,xx}} = \frac{\alpha(1-\beta)}{1 - \frac{\alpha\beta}{32\pi h^3}} = \alpha_{\text{eff,x}}, \tag{5.1}$$

where $h = \Delta + a$ indicates the distance between the point dipole (at the center of the

particle) and the interface. The latter is characterized by its surface response function $\beta = (\varepsilon - 1)/(\varepsilon + 1)$, which has a pole for $\varepsilon = -1$. The total scattered power P_{tot} is proportional to the square modulus of the total dipole moment times the fourth power of the frequency ω (Rayleigh scattering) [19]:

$$P_{\text{tot}} \propto \omega^4 \{|\alpha_{\text{eff,x}} E_x|^2 + |\alpha_{\text{eff,z}} E_z|^2\}. \tag{5.2}$$

This short excursion into the analytical dipole model highlights the underlying mechanism. A resonance of the scattered power corresponds to a large value of α_{eff}. In the limit of large heights between the probe dipole and the sample, this happens when α has a resonance, and therefore the scattering signature is dominated by the probe itself. However, in the case of very small separations, the denominator of Eq. (5.1) might vanish. Analogously, that is associated with a resonance of α_{eff}, which strongly depends on the sample under investigation. Especially samples having $\varepsilon < 0$ might respond resonantly when the probe is placed nearby, even in the case when neither the probe nor the sample shows a resonance when illuminated separately. But when the probe is placed close to the sample, the strong near-field interaction may lead to an excitation of localized surface states which are not addressable by a direct sample illumination from the far field.

The discussion in this chapter begins with the case of resonant probes and concerns both the near- as well as the far-field signature. Later, the second case in which the resonance originates from the tip-sample interaction is investigated in the mid-infrared spectral region, where the surface states arise from localized surface phonon polaritons.

5.1 Resonant probes - silver ellipsoid in the vicinity of a glass interface

Much analytical/numerical work has been devoted to the interaction of propagating waves with a probe at or close to its SPR, mostly in the context of s-SNOM and SERS/TERS [91–98]. We simplify the case that a resonant probe is placed in very close proximity to a substrate by replacing the tip by a small ellipsoid of revolution placed in the evanescent field above a glass prism as displayed in Fig. 3.4. Most of the theoretical results presented so far either neglect the role of the sample surface or the strong variations of the dielectric properties of realistic materials in the optical range, or use two-dimensional models for treating a three-dimensional setup. Despite the fact that scattering of evanescent waves is essential to near-field optical experiments [40, 42, 99, 100], only little theoretical work has so far included an analysis of the near field. In the framework of scattering of evanescent waves, the authors have mostly calculated the far-field properties (extinction and scattering cross sections) of a sphere close to a planar surface, using different methods. For example, Fukuzawa *et al.* used point matching [101], Chaumet *et al.* used the coupled-dipole approximation, and Girard *et al.*

investigated the role of the electric *versus* magnetic field using Green's dyadic technique [102]. Quinten/Wannemacher *et al.* [103,104] found an excellent agreement of the MMP results with an analytical extension of Mie's theory [39], which was presented by Chew *et al.* [105] and later corrected by Liu *et al.* [106].

The investigation for a free ellipsoid placed in the evanescent field was already presented in Sec. 3.3, however without accounting for the role of the interface. In the case that the particle is placed in the evanescent field above a glass surface, the particle senses the evanescent field by getting polarized. This oscillating polarization results in a scattering of light into both half-spaces, a process commonly known as attenuated total internal reflection (ATR). The waves reradiated by the particle are reflected and refracted at the interface. In the theoretical analysis this modification of the electromagnetic field is accounted for by satisfying the boundary conditions at the interface. For the investigations of both the optical near and far fields, again the setup displayed in Fig. 3.4 and in the inset of Fig. 5.2 was used with an ellipsoid having an axis ratio of 100 nm : 30 nm.
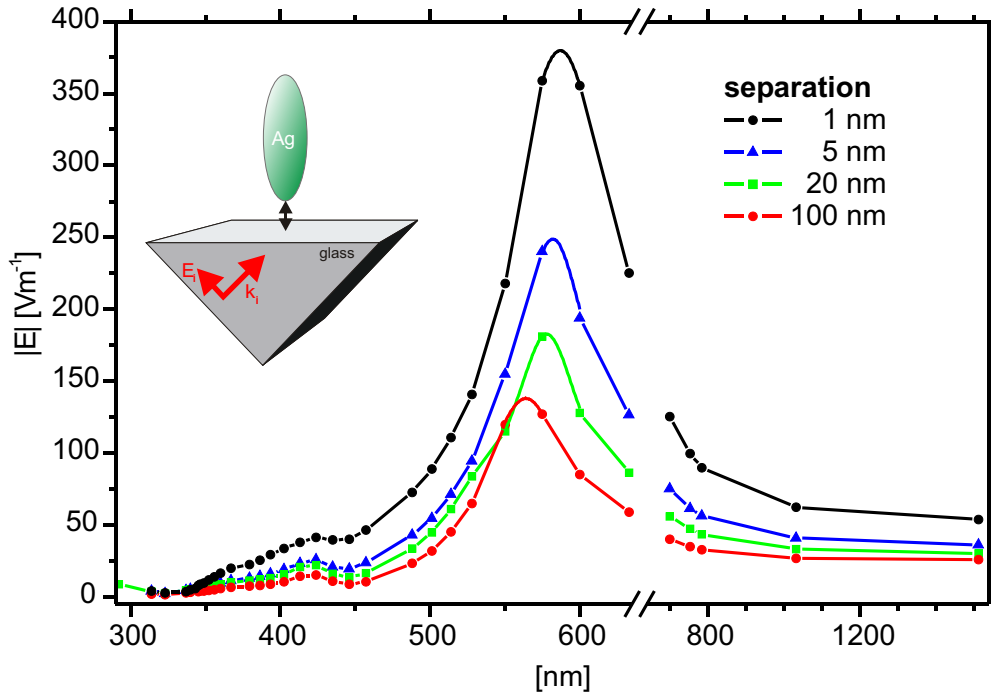
Figure 5.2   *Electric field amplitude at the front apex for different separations Δ between the ellipsoid and the glass surface. The presence of the glass leads to a slight redshift of the main resonance for smaller separations. A spline interpolation was used between the calculated points (marked by the symbols).*

5.1.1 Near-field behavior

The presence of the glass interface changes the boundary conditions of the electromagnetic problem. This is accompanied by a modified polarization of the particle and by surface charge distributions at the surface which modify the near field and the scattered light. To illustrate the influence of the interface, the MMP results for different tip-sample separations Δ for the 100-nm-long particle are plotted in Fig. 5.2. The spectral response at $\Delta = 100$ nm is identical to the case without any interface (see Fig. 3.5) with respect to both the position and shape of the spectral features. For smaller separations Δ of 1, 5, or 20 nm, the particle is subjected to a stronger field. Accordingly, the electric field strength at the front end of the ellipsoid increases in amplitude. Beside this, the influence of the glass boundary becomes more obvious, showing up as a redshift of the main resonance by approximately 15 nm to 575 nm for a separation of $\Delta = 5$ nm, and more than 25 nm to 585 nm for $\Delta = 1$ nm. A modification of the higher-order mode around 413 nm is hardly visible.
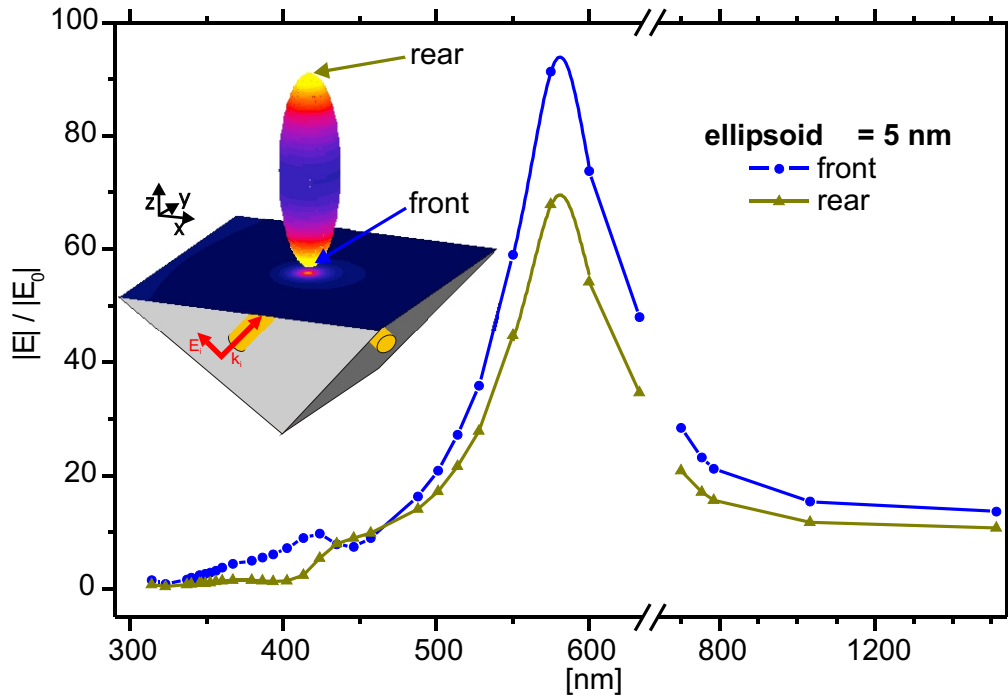
Figure 5.3 *Field enhancement near a 100-nm-long ellipsoid placed 5 nm above the glass interface. At the dipole resonance, the interaction with the glass results in different amplitudes at the front and rear ends of the particle, whereas it becomes uniformly polarized without the glass surface. The inset shows the |E| field at the surface of the particle and at the substrate at the SPR ($\lambda = 575$ nm). The large |E| field underneath the ellipsoid at the substrate is highly confined laterally.*

The field enhancement, defined in an analogous way as in Fig. 3.5, is displayed in Fig. 5.3. In

contrast to Fig. 3.5, the interaction with the glass surface causes the enhancement to become different at the front and rear ends of the particle. Fig. 5.3 clearly shows that the main resonance occurs at the same wavelength at the two ends of the ellipsoid. The higher value of the enhancement factor of approximately 90 in the presence of the interface compared to 60 in the case without any interface (see Fig. 3.5) is understandable within the quasi-electrostatic picture: The polarized particle near the interface induces a mirror dipole whose field acts back on the particle. Thereby, the effective polarizability is increased. The difference between the front and rear end, which was not observed without the interface (Fig. 3.5), arises due to the different distances of the points on both sides of the particle to the image dipole and due to retardation effects. The retro-acting reflected field falls off more rapidly and is more strongly phase-shifted at points farther away from the interface, leading to a lower total field at the rear end.

This enhancement due to the reflected field and the shift of the resonance are the main two differences compared to the case without any glass surface. These changes are rather small but become significantly larger for non-dielectric substrates [92].

5.1.2   Far-field behavior

The near-field behavior is strongly related to the local properties, such as the local radius of curvature. The electromagnetic field in the vicinity of the particle is the superposition of all local contributions and, hence, it contains strong evanescent parts besides the propagating modes. At larger distances, several wavelengths away, these rapidly decaying fields become vanishingly small and only the propagating modes are detectable with conventional far-field optics [107]. The question arises to what extent such far-field measurements also reflect the near-field properties. To answer this question, the intensity scattered to the far field by an ellipsoid having a length of 100 nm and a width of 30 nm located 5 nm above the interface was calculated. The investigated setup shown in Fig. 5.4 assumes the detector to cover the full acceptance angle of $2 \times 40.5°$ (numerical aperture NA = 0.65) in the upper vacuum half-space. The power impinging on the detector is displayed in Fig. 5.5. The calculation was performed for three different detector positions in the interface plane covering the backward, forward, and sideward directions, by integrating the Poynting vector over the detector area. In order to take only the power radiated to the vacuum half-space into account, the integration was restricted to that half of the detector area lying above the interface. For the sake of comparability, the corresponding power for the same ellipsoid not sensing the interface is also plotted in Fig. 5.5. The highest power is detected at the dipole resonance at 575 nm for the case with the glass surface, or at 550 nm without the boundary. The detectable power at the dipole resonance decreases when the particle is placed close to the surface. Furthermore, the small maximum around 413 nm, which was clearly visible in the $|E|$ plot in Figs. 5.2 and 5.3, does not give rise to any clear feature in Fig. 5.5.
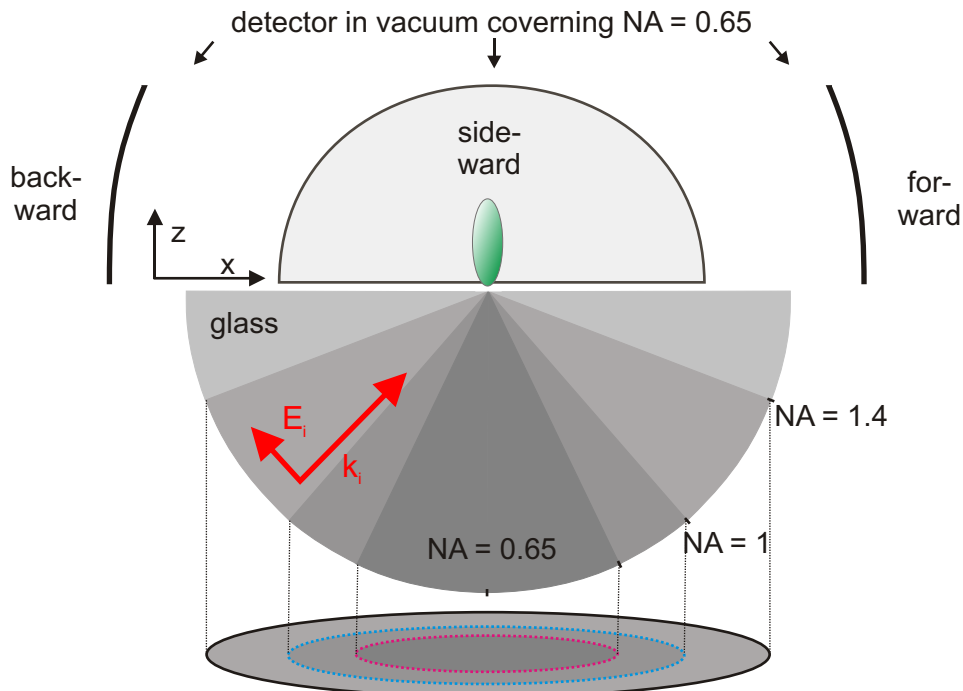
Figure 5.4 *The optical power scattered by the ellipsoid into the far field, impinging on a detector with a numerical aperture NA = 0.65, is investigated for the backward, forward, and sideward directions in the vacuum region. Similarly, the power scattered into the glass substrate was calculated for different NA's. The disc indicates the area plotted in the inset in Fig. 5.6.*

This different behavior can be understood from basic scattering theory (see e.g. [108, pp. 729]). The far-field signature of a particle is related to the polarization at all points in the particle. Hence, for modes that exhibit a uniform polarization over the whole particle, such as dipole modes, the scattered far-field intensity is maximized. For higher-order modes the inhomogeneous polarization across the particle leads to a partial cancellation of the radiated field due to dephasing effects.

The curves calculated for the three different detector positions indicate only minor differences. Only for shorter wavelengths, the detected power differs significantly between forward and backward scattering. The power radiated into the forward direction is considerably larger in the spectral range between 340 and 400 nm. The power radiated to a detector positioned sideways lies between the forward and backward signals.

Finally, it is worthwhile looking at the signal intensity scattered into the glass half-space. This corresponds to a very common setup where the photons are collected in the far field by means of a microscope objective. For this investigation, we use the configuration in Fig. 5.4 and calculated the scattered power for different acceptance angles corresponding to
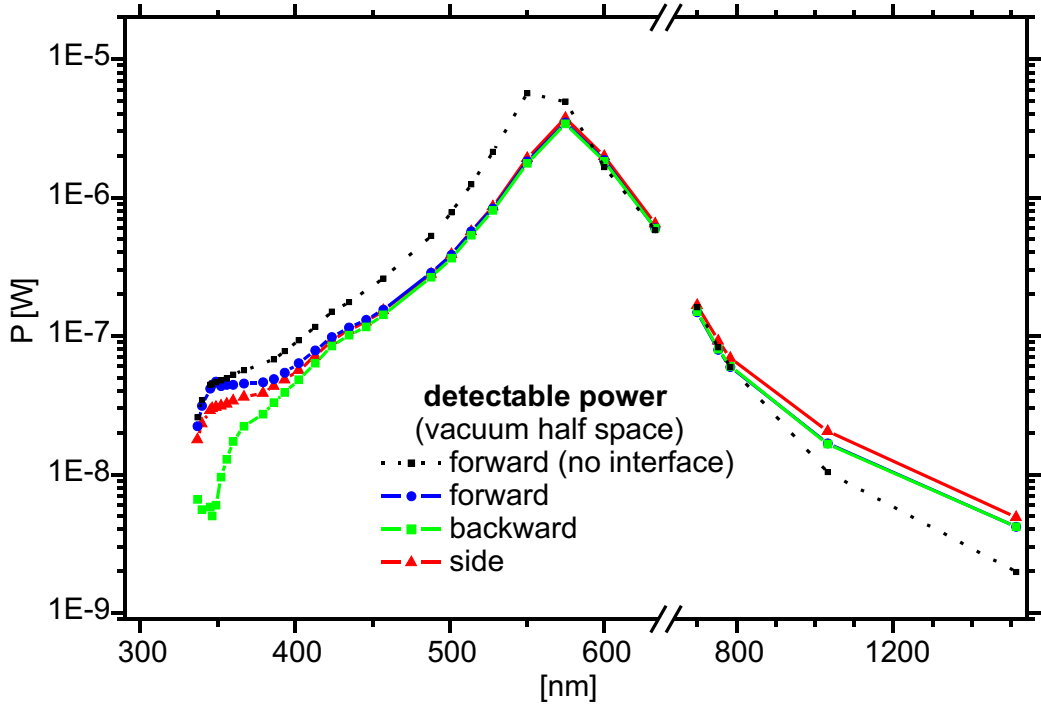
Figure 5.5   *The far-field power impinging on a detector positioned at 3 different locations for a 100-nm-long Ag ellipsoid* $\Delta = 5$ *nm above a glass surface, as well as for the same particle without any interface. The most efficient scattering corresponds to the highest field enhancement at the main SP resonance, whereas the resonance at 413 nm is barely visible.*

microscope objectives with NA = 0.65, 1.0, and 1.4. Fig. 5.6 displays the corresponding spectral dependence. At the dipole resonance around 575 nm, as expected, all curves show a maximum in the detected power, but differ in magnitude by more than a factor of 25. The insets in Fig. 5.6 show the angular dependence of the scattered power on a glass half sphere for the largest NA investigated here. The magnitude measured at the sphere surface is projected onto the xy plane. This exactly corresponds to the discs in Fig. 5.4 where larger radii represent larger acceptance angles. As seen from the insets the maximal power is scattered around the critical angle (NA = 1). Note that the measured power decreases again in the forbidden-light [109,110] regime for angles much larger than NA = 1. Therefore, the experimental sensitivity may be improved by collecting photons from the angular range around the critical angle as shown experimentally by Hecht *et al.* [111].

The higher-order mode around 420 nm, which was visible as a small shoulder in Fig. 5.5, is too tiny to be seen in Fig 5.6. If the power radiated into the smallest angular section (NA = 0.65) is detected, a second small maximum is seen around 347 nm. That peak corresponds to the dipole mode of the ellipsoidal particle having a polarization parallel to the glass interface. Such modes do not lead to a concentration of the electrical field at the particle apex, but rather radiate predominately normal to the interface.
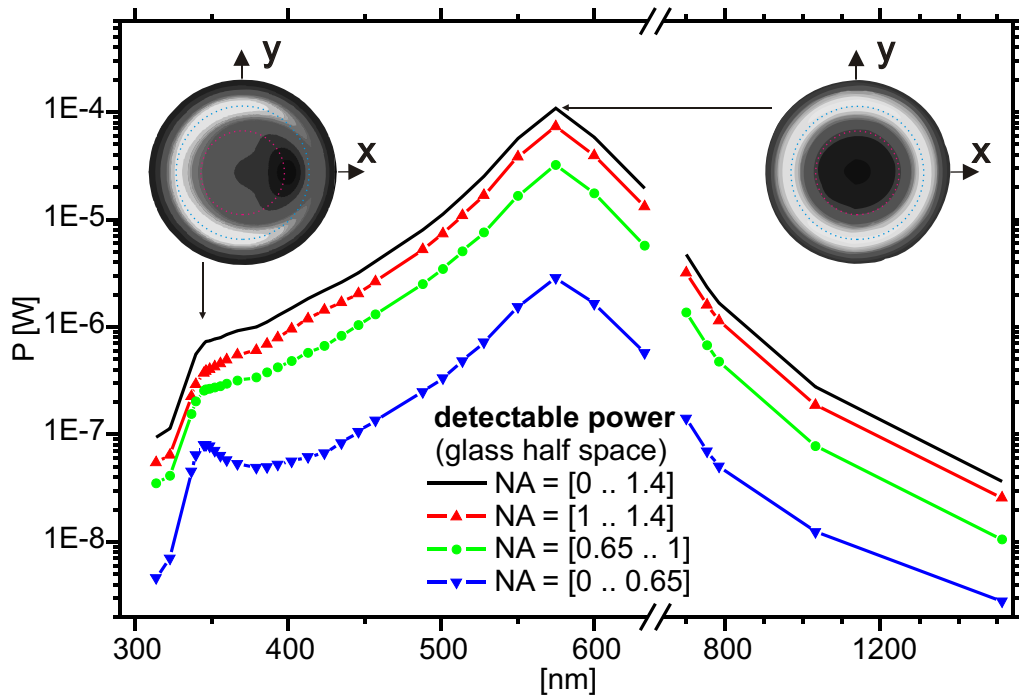
Figure 5.6 *The far-field power radiated by a 100-nm-long Ag ellipsoid with $\Delta = 5$ nm, as collected with a detector inside the glass half-space covering different numerical aperture ranges. The insets show the angular dependence of the scattered light at 575 nm and 347 nm projected on a plane. The dotted circles indicate the portions collected by objectives with NA = 0.65 (magenta circle), NA = 1 (cyan circle), and NA = 1.4 for the whole area. Most of the energy is scattered at angles around and larger than the critical one.*

5.2   Resonant substrates - platinum probe close to SiC

In the ongoing intense discussion on nanooptics, much attention is devoted to surface plasmon polaritons as a source of resonant field enhancement in the optical near field of metallic films and nanostructures [10, 48, 112]. Such resonances occur under the condition that the real part of the dielectric constant ε takes an appropriate negative value. This is fulfilled in metals because of the free conduction electrons, and the resulting resonances of noble-metal nanoparticles mostly appear in the visible portion of the spectrum. It is much less known that surface plasmon polaritons have a counterpart in the infrared (IR) spectral region for some polar materials, caused by optical-phonon resonances. Here, $\mathrm{Re}[\varepsilon]$ is negative in the so-called *reststrahlen* band between the transverse (TO) and longitudinal (LO) optical-phonon frequencies, which gives rise to the existence of so called surface phonon polaritons (SPhPs). SPhPs offer attractive prospects for IR near-field optics. Their damping as characterized by $\mathrm{Im}[\varepsilon]$ can be much weaker than for plasmons. The pronounced sharpness of the resonance opens the door to interesting applications in, for example, high-sensitivity sensorics, and various novel phonon-photonic devices have been conceived [113]. Furthermore, the influence of SPhPs on the near field of thermal emission was discussed in a theoretical paper [107].

Recently, Hillenbrand *et al.* used a s-SNOM to study the scattering of infrared light at the metal-coated tip of an atomic force microscope in close proximity to a phonon-active silicon carbide (SiC) surface [115]. To single out the scattering caused by the near-field interaction between the tip and the sample, the distance was modulated and the resulting oscillation of the scattered field amplitude was demodulated at the second-harmonic frequency of the tip vibration. A typical result of such a s-SNOM measurement is displayed in the inset of Fig. 5.7 for two different wavenumbers. The observed signal contrast exhibited a clear resonance at wavenumbers around 930 cm^{-1}, indicating the excitation of a SPhP at the SiC surface via the near-field of the illuminated tip. The experiment provided evidence that IR spectroscopy with superb spatial resolution $\Delta x < \lambda/100$ is possible.

The experimentally observed spectral response was in fair agreement with the simple dipole model of s-SNOM developed by Knoll and Keilmann [116]. This model describes the apex of the tip as a small polarizable sphere and uses electrostatics for calculating the modification of its dipole field caused by reflection at the sample surface (see Eqs. (5.1) and (5.2)). The model is appealing by its simple analytical treatment, but a number of approximations made can be expected to limit its validity. Due to the near-field interaction with the sample, the probe is expected to acquire higher multipole moments not taken into account in the dipole model. Furthermore, the quasi-electrostatic treatment neglects all retardation effects. Finally, the reduction of the tip to a sphere represents a very crude approximation to the true tip geometry.

Earlier research on such sphere-plane structures has been carried out by P. K. Aravind and H. Metiu [92, 117] and R. Ruppin [118, 119], who solved the nonretarded electrostatic problem analytically.
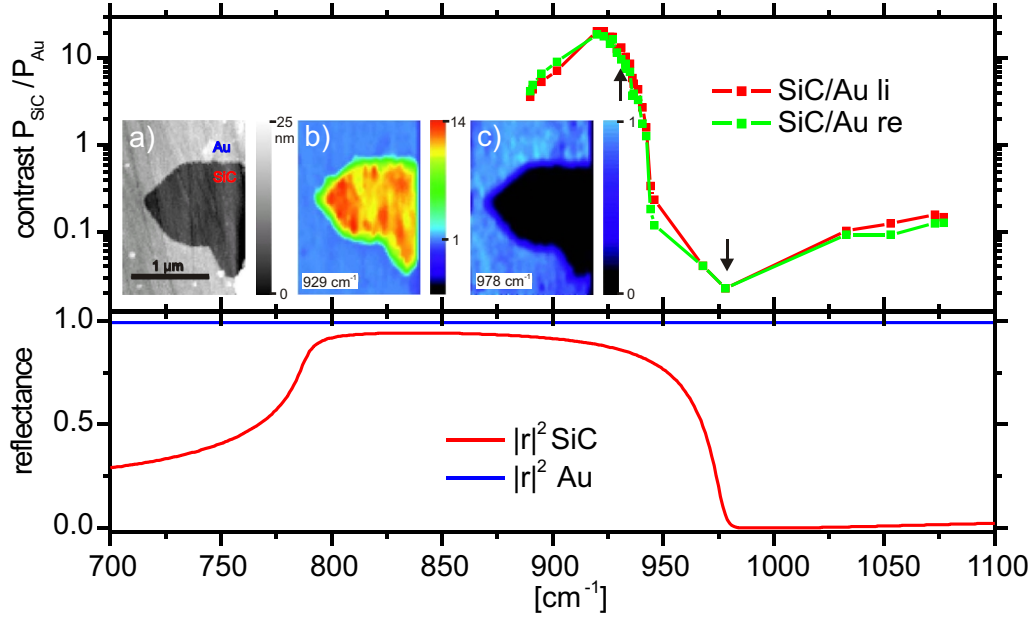
Figure 5.7 *(top) Experimental s-SNOM measurement of the tip-induced optical phonon polariton resonance at two different locations on the SiC sample. The large contrast in the infrared spectrum arises because of the excitation and scattering of localized surface phonon polaritons (SPhPs) by the tip. The s-SNOM measurement insets display (a) the topography of the SiC island surrounded by gold and the optical contrast near the resonance (b), and at higher frequencies (c). (bottom) The reflectance spectra of a SiC and gold substrate reflect the fact that the SPhPs cannot be excited by plane waves because of the momentum mismatch. (s-SNOM pictures and measured data reproduced with kind permission of R. Hillenbrand [113, 114])*

In this section, the validity of the quasi-electrostatic dipole model is analyzed by comparing its predictions with the results of a fully electrodynamic three-dimensional simulation of a situation which comes close to the experimental arrangement of Ref. [115]. But before looking at the complex tip-sample system, it is worth to study the properties of a planar SiC interface.

5.2.1 Optical properties of SiC

The dielectric function of SiC in the interesting spectral region around 900 cm^{-1} is dominated by resonant phonon modes and may to a good approximation be described by a single Lorentzian-shaped resonance [120]:

$$\varepsilon_{\text{SiC}}(\nu) = 6.49 + \frac{3.23}{1 - (\frac{\nu}{\nu_0})^2 - i\frac{\gamma\nu}{\nu_0^2}} \tag{5.3}$$

with the wavenumber $\nu = \frac{1}{\lambda}$, $\nu_0 = 788$ cm^{-1} and $\gamma = 6.8$ cm^{-1}. Illumination is assumed to happen by a p-polarized plane wave incident at an angle θ. Hence, the light will be partially reflected with a reflection coefficient $r_\parallel$ simply given by Fresnel's formula:

$$r_\parallel(\varepsilon_i, \varepsilon_{\mathrm{SiC}}, \theta) = \frac{\varepsilon_{\mathrm{SiC}}\cos\theta - \sqrt{\varepsilon_i \varepsilon_{\mathrm{SiC}} - \varepsilon_i^2 \sin^2\theta}}{\varepsilon_{\mathrm{SiC}}\cos\theta + \sqrt{\varepsilon_i \varepsilon_{\mathrm{SiC}} - \varepsilon_i^2 \sin^2\theta}}, \tag{5.4}$$

with ε_i being the dielectric constant of the surrounding medium ($\varepsilon_i = 1$ in the following). The spectral reflectance $|r|^2$ is plotted in the bottom graph in Fig. 5.7 for $\theta = 45°$. SiC is highly reflective between $\nu_0 = 780$ cm^{-1} and $\nu_0 = 960$ cm^{-1} and the resonance in the s-SNOM signal has no equivalent in the reflectance spectrum of a planar interface.

The electric fields above the SiC are worth being examined more closely: The superposition of the incident electric field $\boldsymbol{E}_{\mathrm{in}}$ and the field $\boldsymbol{E}_{\mathrm{r}}$ reflected off the sample surface constitutes the exciting field $\boldsymbol{E} = (E_x, E_y, E_z)$ to which the probe particle is subjected. $\boldsymbol{E}_{\mathrm{in}}$ and $\boldsymbol{E}_{\mathrm{r}}$ are given by:

$$\boldsymbol{E}_{\mathrm{in}} = E_0 \begin{pmatrix} \cos\theta \\ 0 \\ \sin\theta \end{pmatrix} e^{i(k_x x + k_z z)} e^{-i\omega t}, \tag{5.5}$$

$$\boldsymbol{E}_{\mathrm{r}} = r_\parallel E_0 \begin{pmatrix} -\cos\theta \\ 0 \\ \sin\theta \end{pmatrix} e^{i(k_x x - k_z z)} e^{-i\omega t}, \tag{5.6}$$

where E_0 is the incident amplitude, and $r_\parallel$ denotes the Fresnel reflection coefficient for p polarization defined by Eq. (5.4).

Figure 5.8 shows the electric-field components $|E_z|$ and $|E_x|$ above the interface as a function of incident angle θ and wavenumber ν. $\mathrm{Re}[\varepsilon_{\mathrm{SiC}}]$ is large and negative like in a metal in the frequency region between 800 cm^{-1} and 900 cm^{-1}, and hence the electric field is essentially normal to the interface. For small incident angles θ, however, $|E_z|$ decreases due to the $\sin\theta$ term in $\boldsymbol{E}_{\mathrm{in}}$. Conversely, around $\nu = 964$ cm^{-1}, where $\mathrm{Re}[\varepsilon_{\mathrm{SiC}}]$ passes through zero, the parallel component $|E_x|$ dominates (for $\varepsilon_{\mathrm{SiC}} = 0$ the continuity of the normal component of the dielectric displacement at the interface requires $E_z = 0$). Figure 5.8 clearly shows that the dielectric response of the substrate gives rise to a strong frequency dependence of both the strength and ratio of the field components normal and parallel to the interface in the investigated frequency regime. The value of θ is set to 45° in the following investigation.
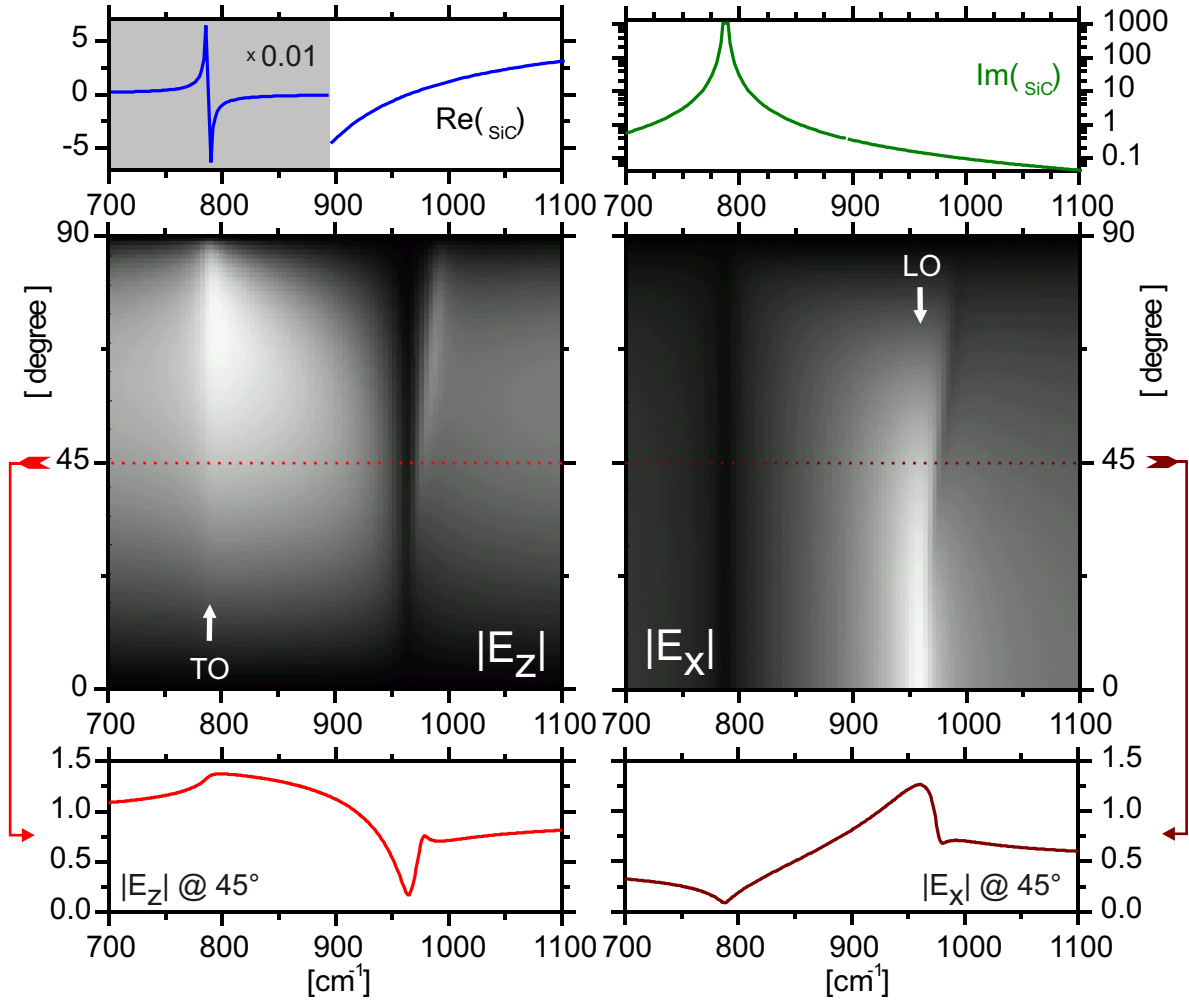
Figure 5.8 *The temporally averaged electric field components $|E_z|$ normal and $|E_x|$ parallel to the SiC interface plotted as a function of incident angle θ and wavenumber ν. The gray scale ranges from 0 (black) to $1.5 \times |E_0|$ (bright). The upper graphs display the dielectric function of SiC. The pronounced variation of $\varepsilon_{\mathrm{SiC}}(\nu)$ is caused by a phonon resonance. $\mathrm{Re}[\varepsilon]$ is negative in the reststrahlen band between the transverse and longitudinal optical-phonon frequencies indicated by TO and LO, respectively. This leads to the clear spectral dependence of $|E_z|$ and $|E_x|$ as seen in the gray-scale maps.*

5.2.2 Contrast in the quasi-electrostatic dipole model

The quasi-electrostatic theory [18] presented at the very beginning of this chapter is applied now to the model scheme displayed in Fig. 5.9. The complex scattering tip is replaced by
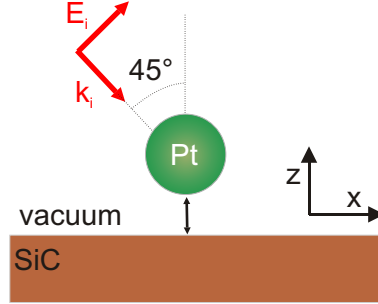
Figure 5.9   *Schematic of the model used for describing the near-field interaction between a metallic probe and a phonon-active sample.*

simple sphere made of platinum. Assuming a frequency-independent dielectric constant of the probe with a value applying to Pt around 900 cm^{-1}, $\varepsilon_{\mathrm{Pt}} = -1249 + 727i$ simplifies the interpretation of the results. Within the quasi-electrostatic picture, the polarizable sphere is described by a single dipole located at its center. The dipole moment of a sphere having a radius a is determined by its polarizability α:

$$\alpha = 4\pi a^3 \frac{\varepsilon_{\mathrm{Pt}} - \varepsilon_i}{\varepsilon_{\mathrm{Pt}} + 2\varepsilon_i}. \tag{5.7}$$

In the vicinity of an interface, the dipole field generated by the sphere is reflected and reinteracts with the sphere. The result can conveniently be written in terms of an effective polarizability α_{eff} given by Eq. (5.1). The computation of the total scattered power P_{tot} (Eq. (5.2)) also requires the electric field:

$$\boldsymbol{E} = \boldsymbol{E}_{\mathrm{in}} + \boldsymbol{E}_{\mathrm{r}} \tag{5.8}$$

above the interface at the position of the dipole. To facilitate an easy comparison with experiments, the power P_{SiC} scattered by the Pt probe above the SiC substrate is normalized to the power P_{Au} scattered when SiC is replaced by gold with $\varepsilon_{\mathrm{Au}} = -5000 + 1000i$. This material contrast V defined as

$$V = \frac{P_{\mathrm{SiC}}}{P_{\mathrm{Au}}} \tag{5.9}$$

can easily be determined and is not distorted by the ν^4 dependence of the total scattered power in the Rayleigh limit.

Figure 5.10 displays the spectral dependence of V as obtained from the quasi-electrostatic theory for a Pt sphere with radius $a = 20$ nm. At large separation $\Delta = 20$ nm, the curve is
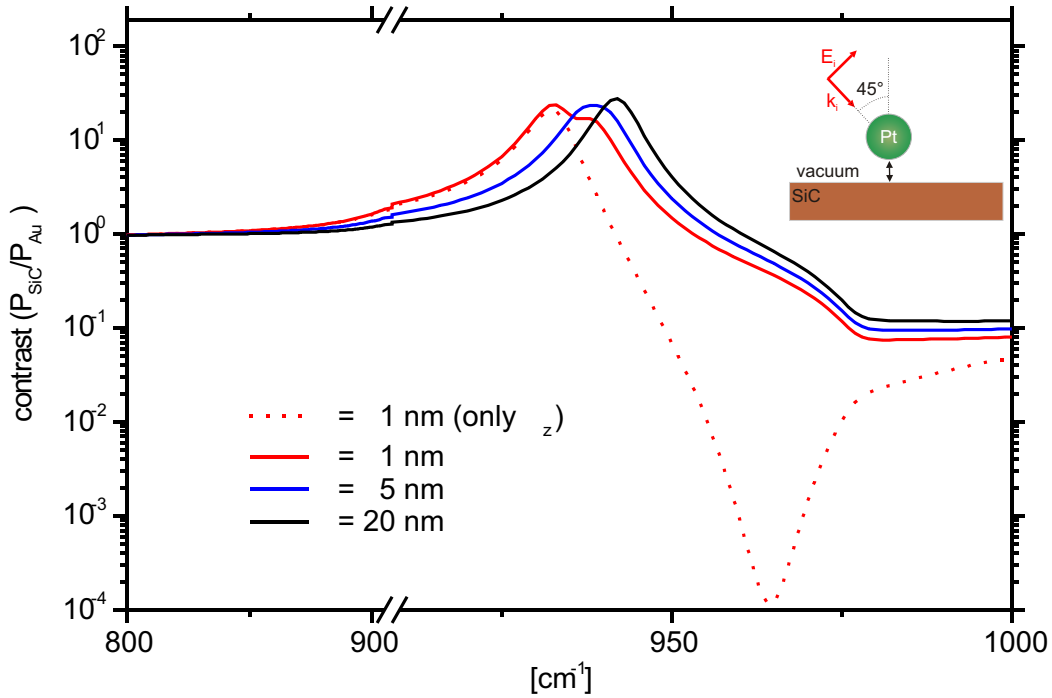
Figure 5.10 *Power scattered by a spherical Pt probe above a SiC surface, normalized to the power obtained for a Au substrate. For large separation ($\Delta = 20$ nm), scattering is strongest around 942 cm^{-1} corresponding to $\mathrm{Re}[\varepsilon_{\mathrm{SiC}}] \approx -1$. When the probe is moved toward the sample, this maximum broadens and shifts to 939 cm^{-1} ($\Delta = 5$ nm), and finally splits into two peaks at 933 cm^{-1} and 938 cm^{-1} ($\Delta = 1$ nm). The dotted curve was calculated for a purely vertical exciting field and exhibits a single maximum at 933 cm^{-1}.*

dominated by the pole of β, which leads to a maximum of the effective polarizability close to 942 cm^{-1}, where $\mathrm{Re}[\varepsilon_{\mathrm{SiC}}] \approx -1$. At smaller distances, the near-field interaction between probe and sample, as represented by the denominators of $\alpha_{\mathrm{eff,z}}$ and $\alpha_{\mathrm{eff,x}}$ in Eq. (5.1), becomes more important. Consequently, the maximum shifts differently for the two field components parallel and normal to the interface. As a result, the maximum broadens and shifts to 939 cm^{-1} for $\Delta = 5$ nm. Finally, close to contact at $\Delta = 1$ nm, the peak splits into two separate modes. The different origin of the two maxima becomes clear when E_x is set to zero in the calculation of V. Then, only the more pronounced maximum at 933 cm^{-1} remains (see dotted curve in Fig. 5.10). Hence, this resonance, which is shifted to a frequency for which $\mathrm{Re}[\varepsilon_{\mathrm{SiC}}] \approx -1.5$, is excited by the normal field component, whereas the less shifted peak at 938 cm^{-1} originates from the parallel component. Around 964 cm^{-1}, the suppression of E_x leads to a deep minimum of V, caused by an almost complete vanishing of E_z in this frequency range (see Fig. 5.8). In the following, the two modes are referred as the normal and the parallel mode, respectively.

5.2.3   Scattering signature of a sphere

The electrodynamic problem for the same system was solved using MMP in order to check the results of the quasi-electrostatic description and to highlight its main deficiencies.

Again, we start the discussion by considering the situation for a fairly large separation
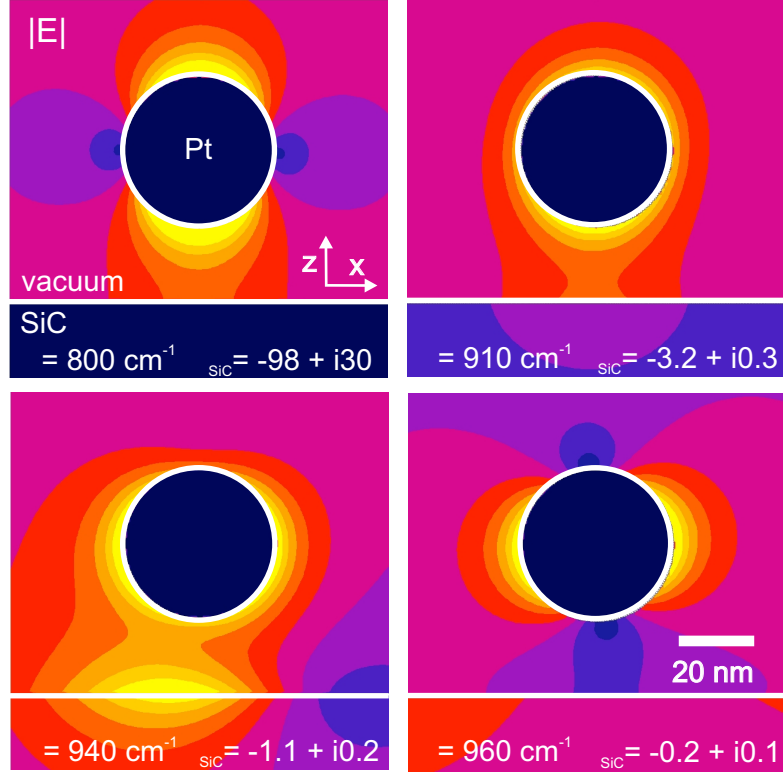
Figure 5.11   *Electric field amplitude $|E|$ around a Pt sphere 20 nm above a SiC surface at four different frequencies. The spectral dependence of the sphere polarization mainly follows the frequency dependence of the exciting field (see Fig. 5.8). The metal-like behavior of the substrate at 800 cm^{-1} results in a polarization normal to the interface. The parallel component dominates at higher frequencies. Around 940 cm^{-1} ($\mathrm{Re}[\varepsilon_{\mathrm{SiC}}] \approx -1$) localized surface waves are excited. Bright colors correspond to high $|E|$.*

$\Delta = 20$ nm between the spherical Pt scatterer and the SiC surface. Figure 5.11 displays the electric-field distribution $|E|$ surrounding the sphere for various frequencies ν. Around 800 cm^{-1} the SiC substrate behaves metal-like. Therefore, the electric field above the sample is dominated by the normal component (see Fig. 5.8) resulting in a polarization of the sphere along the z axis. For higher ν (less metallic behavior) this situation changes. Near 910 cm^{-1} $|E_z|$ and $|E_x|$ are comparable in size and phase-shifted by $\approx \pi/2$ with respect to each other, so that they produce an almost circularly polarized electric field leading to a rotating dipole in the sphere. Therefore, $|E|$ is almost uniform along the circumference of the sphere in the

xz plane. Around 940 cm^{-1} (Re[ε_{SiC}] ≈ -1), the excitation of SPhPs becomes resonant. For large k values in the surface plane the SPhP dispersion relation asymptotically approaches the frequency for which Re[ε_{SiC}] $= -1$. Therefore, close to this frequency a localized SPhP wave-packet made up of essentially standing waves with short wavelengths can be excited. The necessary large k vectors are provided by the near field of the polarized sphere. Due to momentum conservation, this process is forbidden if the scatterer is absent. This excitation leads to a pronounced field distortion with a strong field near the sample surface. Beyond this surface resonance, at 960 cm^{-1}, the sphere becomes polarized along the x axis, in accordance with the electric field being essentially parallel to the interface as illustrated in Fig. 5.8.

In summary, the interaction between the sphere and the SiC substrate is rather weak if they are separated by some ten nanometers. The probe polarization is more or less directly determined by the exciting field above the sample given by Eq. (5.8). This picture changes only when excitation of SPhPs becomes possible, which leads to an appreciable probe-sample interaction. Such near-field properties are important for all processes that are sensitive to the local electric field such as Raman scattering and surface-enhanced infrared absorption (SEIRA) [121]. In the context of surface-enhanced spectroscopy, the excitation of the surface polariton via a conducting sphere was also considered in an earlier work by Aravind and Metiu, who introduced the name "gap mode" for the resulting resonance of the coupled system [117].

To compare our numerical findings with the dipole model, the normalized ratio V, which reflects the signature to be expected in a s-SNOM experiment where the radiated power is detected in the far field was calculated. Figure 5.12 depicts the spectral dependence of V as derived from the numerically calculated far-field distribution for different separations Δ. This plot may be directly compared with the results of the dipole model displayed in Fig. 5.10. Due to excitation of surface waves and their scattering by the sphere, the spectrum exhibits a maximum around 940 cm^{-1} for $\Delta = 20$ nm. Moving the scatterer closer to the interface shifts this resonance to 932 cm^{-1} for $\Delta = 5$ nm. At an even smaller distance of $\Delta = 1$ nm the maximum splits into two clearly separated peaks at 910 cm^{-1} and 932 cm^{-1}.

There is a satisfactory overall agreement between the results of the accurate numerical model and the predictions of the quasi-electrostatic dipole model. The latter reproduces the SPhP resonance in a qualitatively correct way. However, there are clear quantitative discrepancies for small probe-sample separations in the spectral region of the resonance. For $\Delta = 1$ nm the splitting and shift of the two modes as well as their enhancement are much less pronounced in the dipole model (splitting $\Delta\nu \approx 5$ cm^{-1}, see Fig. 5.10) than in the MMP results ($\Delta\nu \approx 22$ cm^{-1}, Fig. 5.12). Furthermore, V is three times smaller at 910 cm^{-1} than at 932 cm^{-1} according to the numerical treatment, whereas the dipole model predicts the lower-frequency normal mode to be the stronger one.

The inspection of the electric-field distribution at the maxima provides some insight into the nature of the two resonant modes (Fig. 5.13). As seen in the snapshots depicted in the lower part of the figure, the electric field directly underneath the probe points predominantly along
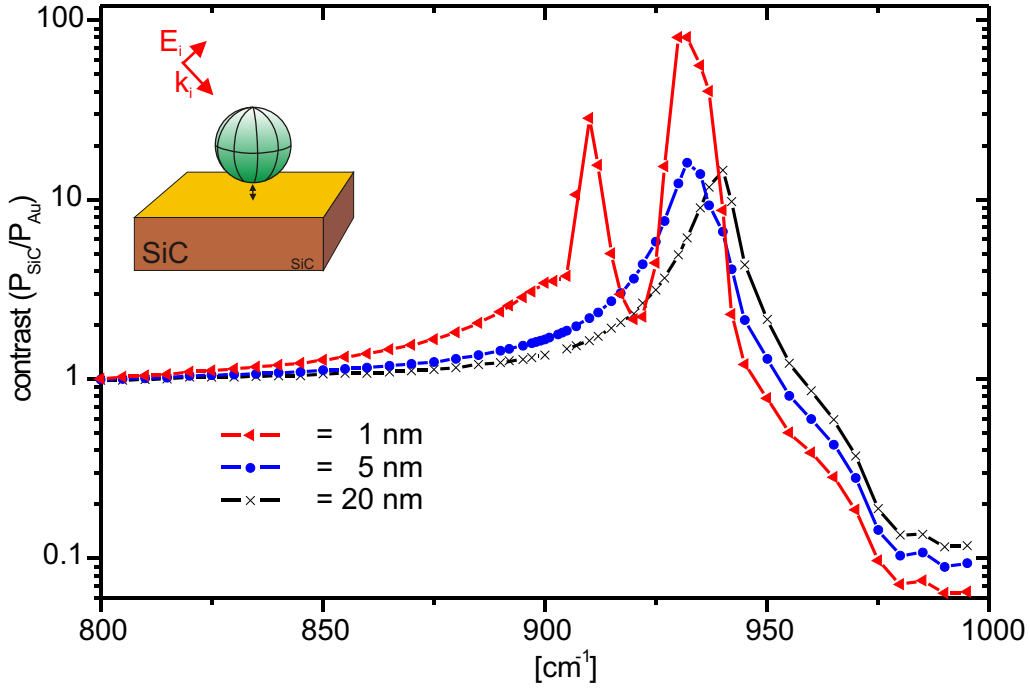
Figure 5.12   *Power scattered by a spherical Pt probe above SiC, normalized to the power obtained with a Au substrate. For large $\Delta = 20$ nm, the scattering is resonantly enhanced near 940 cm^{-1} corresponding to $\mathrm{Re}[\varepsilon_{SiC}] \approx -1.1$. At smaller distances, this maximum shifts to 932 cm^{-1} for $\Delta = 5$ nm, and additionally splits into two peaks at 910 cm^{-1} and 932 cm^{-1} for $\Delta = 1$ nm.*

the z direction in case of the normal mode (910 cm^{-1}), in accordance with the vertically oriented dipole moment of the sphere . The parallel mode, on the other hand, shows a more complicated field pattern. To accommodate the horizontal dipole moment of the sphere, the field has to reverse its direction over a very short distance along the x axis. This corresponds to excitation of surface waves with very high k vectors, which explains why this mode is higher in frequency (932 cm^{-1}).

To conclude this section, one should remember that reduction of the scattering sphere to a simple point dipole at the center of the sphere, as assumed by the dipole model, is a rather crude approximation for small separations, especially close to the substrate-induced resonance. At this point, a closer look at the physics/electrodynamics is advisable. The mirror dipole used in the quasi-electrostatic model is only a mathematical aid to fulfill the boundary conditions. The mirror dipole simply "creates" the surface charge density distribution ρ at the SiC/vacuum interface necessary to meet the continuity of the normal component of the dielectric displacement at the boundary. Analogously, the polarization of the sphere originates from surface charges distributed all over the particle rather than from a dipolar source at the
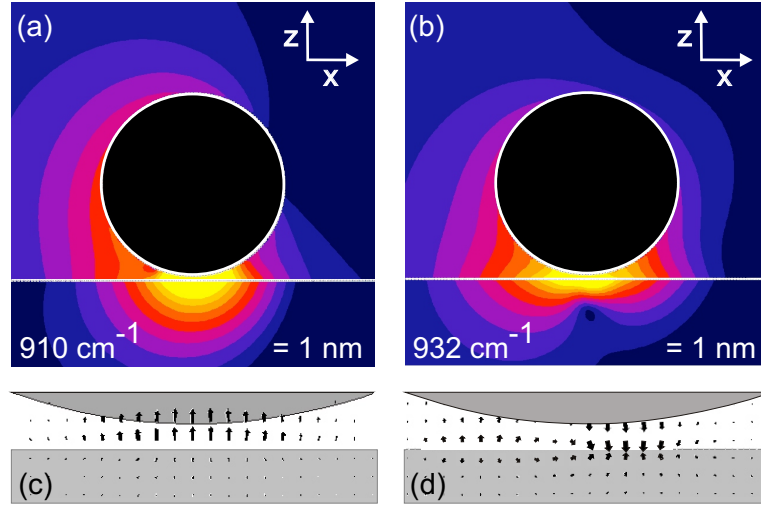
Figure 5.13   (a), (b) Electric-field amplitude $|E|$ around a Pt sphere 1 nm above the interface. The data are displayed on a logarithmic color scale with successive hues differing by a factor of two. The electric-field patterns in (c), (d) (reflecting one specific moment in time) reveal the different field directions for the two resonances. At 910 cm^{-1} the field underneath the tip is more or less uniformly oriented along the z direction, whereas at 932 cm^{-1} the field reverses its direction from $-z$ to $+z$ across a short distance along the x axis.

center. The local value of ρ may be obtained from the discontinuity of the normal component of the electric field at the interface:

$$\frac{\rho}{\varepsilon_0} = \boldsymbol{n}(\boldsymbol{E}_{\mathrm{Pt}} - \boldsymbol{E}), \qquad (5.10)$$

where $\boldsymbol{E}$ and $\boldsymbol{E}_{\mathrm{Pt}}$ denote the fields outside and inside the sphere.

Figure 5.14 illustrates the variation of the surface charge density on a Pt sphere placed as close as 1 nm above the SiC surface. The geometrical center (indicated by the dotted white lines) does not coincide with the center of charges anymore. Most of the surface charges are located at the lower "end" of the sphere pointing to the substrate. The field produced by the charges strongly interacts with the SiC substrate by inducing surface charges at this interface which in turn reinteract with the sphere and so on.

However, the validity of the dipole approximation can in fact be restored to some extent if the position of the dipole is shifted from the center of the sphere towards the interface. This effective displacement becomes increasingly pronounced with decreasing separation Δ between sphere and interface. For example, at $\Delta = 1$ nm, a shift of the dipole by 4.3 nm makes the resonances predicted by the analytical model coincide within ~ 1 cm^{-1} with those found numerically. However, the amplitude ratio of the two peaks is still not reproduced correctly. This confirms that also higher-order multipoles have to be taken into account in a refined model, as pointed out by Porto *et al.* [98].
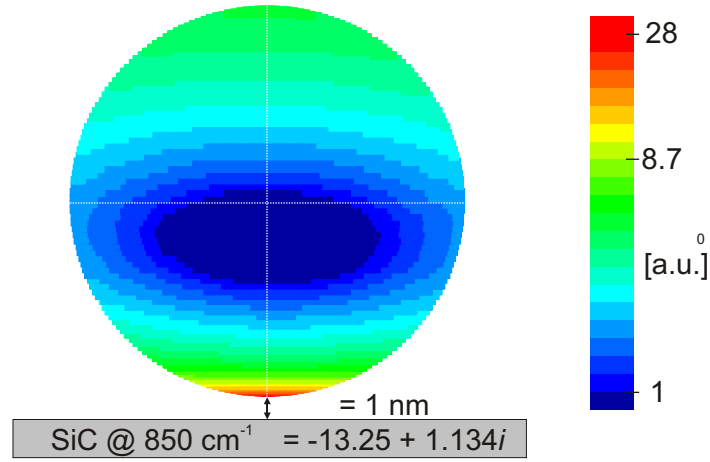
Figure 5.14   *The strongly interacting surface charges on the planar SiC/vacuum and the curved vacuum/platinum interfaces cause a displacement of the center of charges from the geometrical center.*

For a separation between the particle and the interface of some ten nanometers the resonance is centered around the frequency where $\mathrm{Re}[\varepsilon_{\mathrm{SiC}}] \approx -1$. For smaller separations the near-field interaction arising from the stronger coupling between the polarized sphere and the SPhPs causes a shift toward more negative ε values. Finally, below a distance of 5 nm, the resonance splits into two modes coupling to different field components. This behavior is reproduced qualitatively also by the quasi-electrostatic dipole model which, however, underestimates both the spectral shift and splitting, and also provides the wrong intensity ratio of the two modes. Off resonance, the quasi-electrostatic and the numerical model produce nearly identical results.

The main weakness of the analytical model is not the electrostatic approximation, which is actually well fulfilled in the wavelength regime under consideration. It is rather the replacement of the scatterer by a point dipole at its center that becomes invalid at small distances. Then, the dipole is effectively displaced from the center of the probe and, additionally, higher-order multipoles begin to play a role. In fact, the experimental data in [115, 122] confirm that the shift is stronger than predicted by the dipole model. With an effective reduction of the distance of the probe dipole from the surface, the stronger shift of the resonance can, however, still essentially be understood within the dipole model. The pronounced dependence of the resonant frequency on the distance at small separations has a clear impact on experiments in which the distance is modulated. To take most advantage of the SPhP resonance and to achieve the highest spatial resolution, one should choose the wavelength such that it fits the resonance at the inner turning point of the probe vibration.

5.2.4 Scattering signature of an ellipsoid

Modelling the s-SNOM probe by a sphere represents the simplest approach only and may be too far from the real experiment, in which probing is realized by scattering the near field at a sharp metallic tip [6–8]. Such a probe is highly anisotropic with respect to its polarizability parallel and normal to the sample surface. To investigate the influence of the probe geometry on the spectral response, we replaced the sphere by a prolate Pt ellipsoid having a length and width of 100 nm and 30 nm, respectively. The larger volume of the
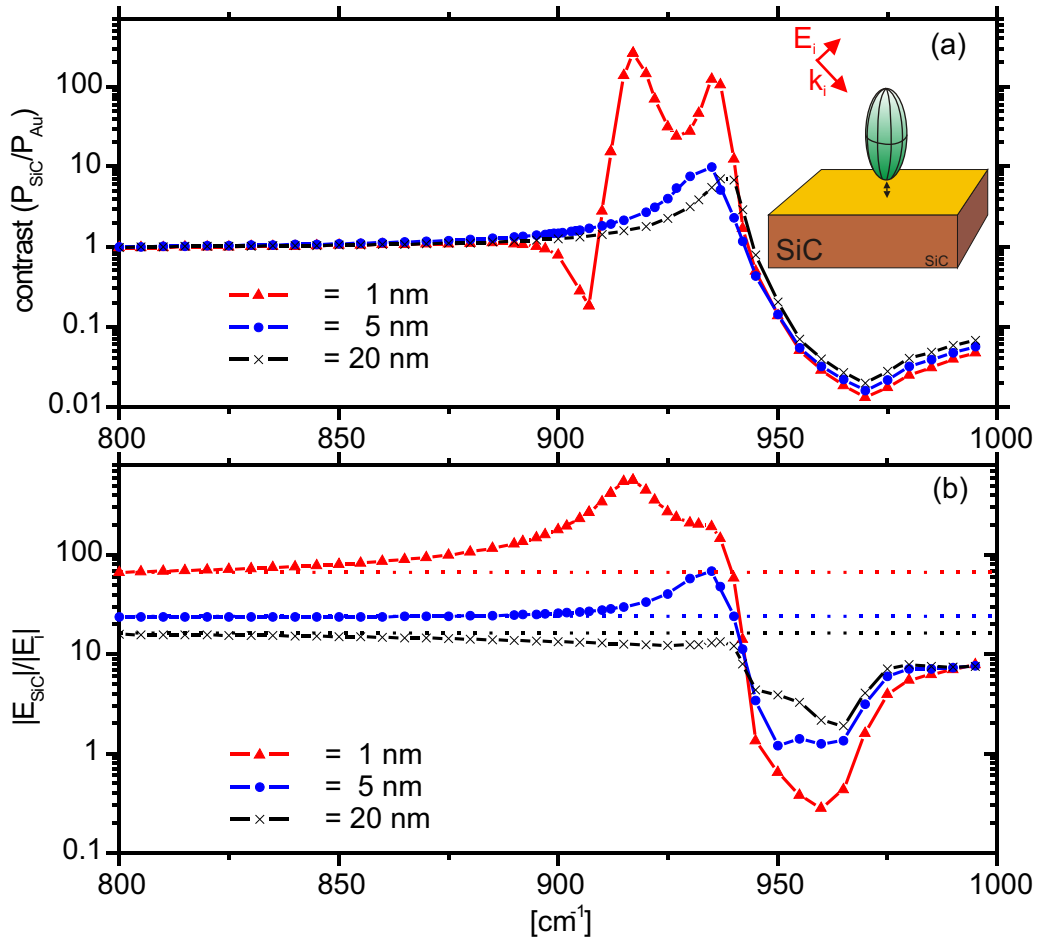
Figure 5.15 *(a) Scattered power for a 100-nm-long and 30-nm-wide ellipsoidal Pt probe above SiC, normalized to a Au substrate. The spectra show a similar splitting of the resonance for small separations like in the case of a spherical probe (Fig. 5.12), however with a slightly smaller shift of the maxima to 917 cm^{-1} and 935 cm^{-1} for $\Delta = 1$ nm, and to 935 cm^{-1} for $\Delta = 5$ nm. (b) Electric-field enhancement at the lower end of the ellipsoidal probe above a resonant SiC substrate (solid curves) compared with the behavior of the same particle above a nonresonant Au substrate (dotted lines).*

ellipsoid results in a larger scattered power in absolute numbers, but again the consideration of the relative contrast V versus a gold sample (see Fig. 5.15 (a)) is preferred. If the ellipsoid and the substrate are separated by $\Delta = 20$ nm, the resonance is centered around 937 cm^{-1}. Getting closer to $\Delta = 5$ nm shifts the resonance toward 935 cm^{-1}, while for $\Delta = 1$ nm the modes appear separated at 917 cm^{-1} and 935 cm^{-1}. Because of the higher polarizability along the long axis (see Sec. 3.3), the resonance peak at 917 cm^{-1} (normal mode) is now the more pronounced one with an amplitude twice as high as the maximum at 935 cm^{-1} (parallel mode). The normal mode is significantly less frequency-shifted than for a spherical probe. This can be attributed to a larger effective distance between the sample and the probe dipole for the elongated ellipsoid as compared to the sphere. In the frequency range above the resonance, where E_z becomes small and the field is dominated by E_x (see. Fig. 5.8), the smaller polarizability along the short axis leads to a minimum of V, which was not present in the previously considered case of a sphere unless E_x was artificially set to zero (see Fig. 5.10). We can easily treat the interaction between the ellipsoid and the substrate in the quasi-electrostatic model by replacing the isotropic polarizability α in Eq. (5.1) by the polarizability along the corresponding semiaxis as given by Eq. (3.2). The outcome of this calculation strongly differs from the MMP results plotted in Fig. 5.15. The resonance of the parallel mode is much weaker than for the normal mode, because of the strongly decreased polarizability along the short axis compared to that along the long axis (nearly a factor of 40). Therefore, the parallel mode is nearly completely suppressed in the quasi-electrostatic model, whereas the more accurate MMP modelling reveals a much stronger contribution of this mode. This behavior reflects the fact, that the resonance originates in the near-field interaction of the surface charges between the probe and the sample, which is dominated by those parts of the probe being closest to the sample. In contrast, surface charges located at the rear end of the probe contribute much less. The last statements are underpinned by a recomputation of an arrangement having a further increased aspect ratio of the probe. This was done by inserting a 250 nm long cylinder having a diameter of 30 nm between the upper and lower halves of the ellipsoid. The system (data not shown) still shows a pronounced resonance of the parallel mode (being comparable to the normal mode) but drastically different polarizabilities along the axes of this prolate particle.

Finally before closing this paragraph, we take a closer look at the enhancement of the electric field strength at the very end of the ellipsoid, representing the tip apex. Figure 5.15(b) displays the field enhancement $|E_{\mathrm{SiC}}|/|E_0|$ with respect to the incident field. If, for comparison, the SiC sample is replaced by Au, the field enhancement takes on the values indicated by dotted lines. For the latter system, consisting of two nonresonant materials (Au substrate and Pt probe), $|E|$ increases by a factor of 1.5 when the distance Δ is reduced from 20 nm to 5 nm, and by another factor of 2.8 upon further reduction of Δ to 1 nm. The resonance produced by the SiC surface leads to a further enhancement that is higher by as much as a factor of 8.4 for the smallest separation. This increased electric field very close to the interface may be

used to gain sensitivity and lateral resolution, e.g., in surface enhanced infrared absorption (SEIRA) [121] measurements. For larger separations, the factor in favor of SiC drops to 2.9 at $\Delta = 5$ nm and to <1 at $\Delta = 20$ nm. The reason for this behavior is that at larger distances Δ the favorable influence of the surface resonance in SiC becomes weaker. Under these circumstances, the resulting field turns out to be stronger for a gold sample, simply because of the higher reflectivity of the metal surface.

In summary, the shape of the probe has a clear influence on the spectral dependence of the scattering. However, as the resonance originates from the sample, this influence is not as dramatic as it would be if the resonance had its origin in the polarizability of the probe. In this latter case of a particle polariton, frequently considered in the literature as a means of enhancing the scattering, the probe geometry is one of the key parameters determining the resonant frequency. In real experiments, the shape of the probe is often rather ill defined, which makes it difficult to fulfill the resonance condition of such a probe polariton in a reproducible way. A resonance residing in the sample, as treated in the present section, offers the advantage of being much more robust versus variations of the geometry and material composition of the probe. Furthermore, the analytical model treats the probe as a sphere, far from the real shape of s-SNOM probes. The MMP results obtained for an ellipsoidal scatterer show that variation of the probe geometry leaves the coarse signature of the resonance unchanged but has a clear influence on the details of the spectral response. In particular, a vertically elongated probe tends to favor the resonant mode related to the normal field component. Note that considering the contrast versus a gold sample suppresses the overall ν^4 frequency dependence of the scattered power, thereby emphasizing the spectral features arising from the tip-sample interaction. Therefore, the main trends should remain valid also for probes with a more realistic conical shape, even though such a geometry leads to a much weaker overall frequency dependence [123].

5.2.5 Comparison to experiments - influence of the demodulation

The material contrast displayed in Fig. 5.10, Fig. 5.12, and Fig. 5.15 was calculated for a fixed separation Δ, whereas the experimental data shown in the top graph in Fig. 5.7 were recorded using an AFM tip that vibrated normal to the interface at its mechanical resonance frequency ω_{res}:

$$h_{\text{tip}}(t) = h_0 + A\cos(\omega_{\text{res}}t), \qquad (5.11)$$

with an oscillation amplitude A typically in the order of some tens of nanometers. The back-scattered light was detected interferometrically and demodulated at $2 \cdot \omega_{\text{res}}$ in order to discriminate the background from the near-field signal. Hence, the second Fourier component of the scattered electric field has to be taken in the models for an oscillating probe with $h_{\text{tip}}(t)$. This analysis would require the computation at all frequencies and for all separations. This is a tremendous effort for the MMP modelling. But with the restrictions of the analytical sphere

model in mind, we may use the quasi-electrostatic theory as presented before (see Eqs. (5.1) and (5.2)) for a qualitative analysis of the problem.

Displacing the dipole slightly away from the geometrical center of the sphere towards the
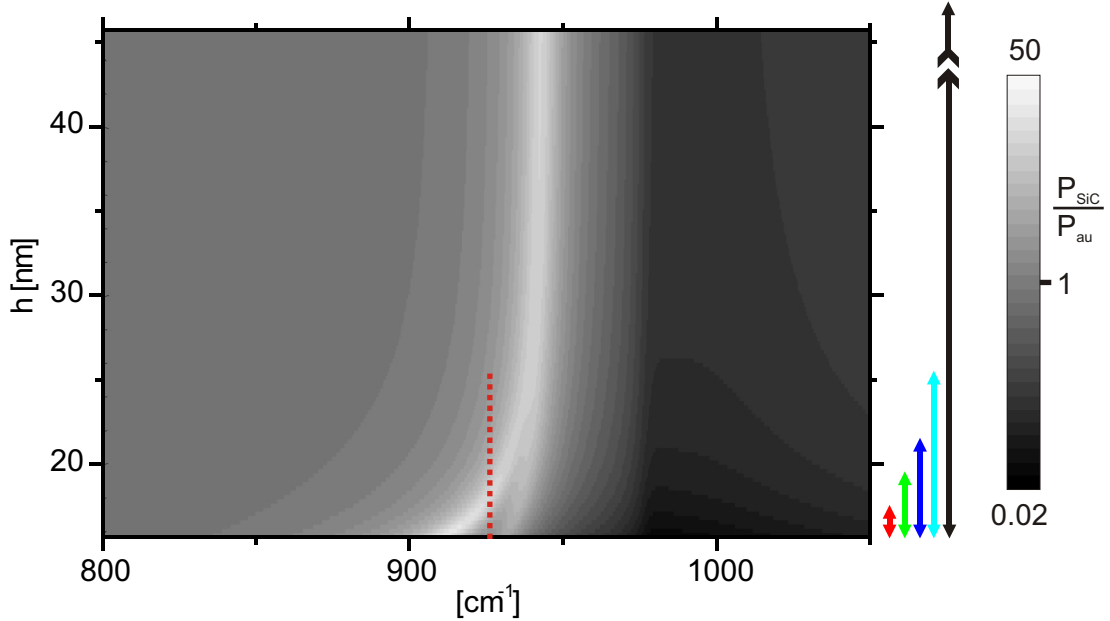
Figure 5.16   *The contrast calculated using the quasi-electrostatic model reflects the substrate-induced resonance shifts for small separations. The mode where the polarization of the particle is normal to the interface is shifted more strongly than the parallel mode. The colored arrows indicate the different probe oscillation amplitudes $2A = 2, 4, 6, 10, 60$ nm discussed in Fig. 5.17.*

substrate for small separations compensates for the underestimation of the shift of the resonance frequency. The lowest height of the dipole $h_{min} = 15.7$ nm in Fig. 5.16 was chosen in order to reproduce the shift and splitting calculated by the MMP method for a sphere having $r = 20$ nm separated by $\Delta = 1$ nm from the SiC substrate (see Fig. 5.12).

Both effects (shift and splitting) are a consequence of the strong near-field interaction at small h and vanish nearly completely for $h > 25$ nm as shown in Fig. 5.16. Hence, a height variation during the measurement may crucially alter the signal close to a resonance because of the presence of the two gap modes. Approaching the sphere from $h = 26$ nm to h_{min} (see red dotted line in Fig. 5.16) at $\nu = 925$ cm^{-1} for example, makes the contrast increase till $h = 18$ nm is reached. Finally, at smaller distances, V[1] decrease again.

The mechanical oscillation of the probe during a s-SNOM measurement corresponds to a variation of the height of the dipole above the surface as indicated by the vertical colored

---

[1]It is worth noticing that the same mechanism may be effective when resonant particles are used instead of resonant substrates.
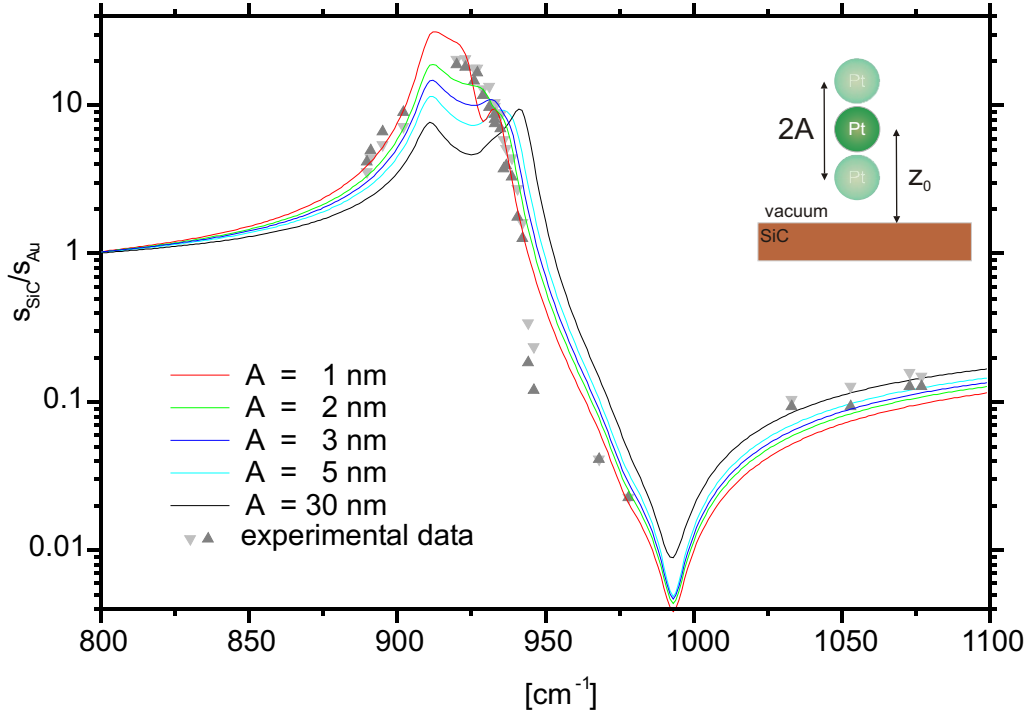
Figure 5.17   *The resonance frequency of the Pt sphere above the SiC surface changes because of the mechanical oscillation of the s-SNOM probe normal to the substrate. Therefore, the measured signal spectra recorded at $2 \cdot \omega_{\mathrm{res}}$ vary depending on the mechanical oscillation amplitude 2A. The experimental data were reproduced from Ref. [114].*

arrows in Fig. 5.16. Hence, the near-field interaction and therefore $P_{tot}(h_{\mathrm{tip}}(t))$ vary during each single oscillation cycle, leading to signal components not only at ω_{res} but also at higher harmonics of the probe oscillation, e.g. $2 \cdot \omega_{\mathrm{res}}$. The contrast variation at $2 \cdot \omega_{\mathrm{res}}$ can be measured with lock-in technique, as shown in Ref. [113, 114].

Now, the signal can be extracted from $P_{tot}(h_{\mathrm{tip}}(t))$ as given by the quasi-electrostatic dipole model by calculating the Fourier component at $2 \cdot \omega_{\mathrm{res}}$ numerically. The response at $n \cdot \omega_{\mathrm{res}}$ for very small values of A is proportional to the nth derivative with respect to the probe height [124]. The spectral variation of the contrast when such a demodulation scheme is used, is displayed in Fig. 5.17 for different values of A and a fixed lower turning point. The response for very small A is dominated by the strongly shifted normal mode. Larger oscillation amplitudes cause a strong change of the position of the resonance as shown in Fig. 5.16. This leads to a blurring of the peak and a reduction of V.

This analysis shows that the mechanical oscillation amplitude of the probe crucially influences the measurable contrast. Hence, the value A has to be carefully controlled and kept constant during the experiment in order to prevent artifacts [125] in the optical signal which could originate from a different damping of the s-SNOM probe close to the sample.

Recently, similar resonance shifts were observed experimentally by s-SNOM probing of SiC
by Taubner *et al.* [122] in the mid-infrared spectral range. They used a Pt-coated AFM tip
to measure the Fourier component at $2 \cdot \omega_{\mathrm{res}}$ for different separations $h_0 = 9, 24, 40, 55$ nm and
a small oscillation amplitude $A = 5$ nm. The observed shift of the peak was roughly 9 cm^{-1}.
However, only one resonance was observed [115, 122]. This might indicate that the antenna
properties of a real cone-shaped probe lead to an even stronger enhancement of the normal
mode as compared to a prolate spheroid. Furthermore, in [122] the SiC sample was highly
doped and therefore exhibited larger damping. An analysis within the dipole model shows
that such an increase of Im$[\varepsilon]$ affects the parallel mode more strongly than the normal one.
A definitive answer to the question as to which role the parallel mode plays in the case of
conical probes and under what conditions it may become visible in the experiment requires a
numerical treatment of the conical geometry.

The high sensitivity of light scattering to the local dielectric properties of the substrate
around the surface phonon polariton frequency ($\varepsilon \approx -1$) also allows the distinction of differ-
ent ε components along orthogonal orientations in optically anisotropic samples. Very recent
measurements on ferroelectric barium titanate (BaTiO$_3$) by S. Schneider *et al.* [126] support
this finding. Microscopically, the ferroelectric polarization originates in the displacement of
the Ti^{4+} ion and the O^{2-} ions within the BaTiO$_3$ unit cell. Hence, the formerly isotropic
permittivity ε of the substrate has to be replaced by the permittivity tensor $\widehat{\varepsilon}$, which ac-
counts for the tetragonal symmetry and the nonuniform dielectric properties, arising through
the splitting of the vibrational (phonon) modes along the different crystal directions. The
corresponding dielectric values of ε_a and ε_c are assigned to two orthogonal directions a and
c in the unit cell, and differ within the investigated wavelength range as specified by the top
axis in Fig. 5.18 (a) and the bottom axis in Fig. 5.18 (c), respectively. Furthermore, the ori-
entations of the domains, i.e. parts of the crystal having the same (ferroelectric) polarization,
with respect to the surface have to be accounted for.
In [126], the investigated ferroelectric perovskite BaTiO$_3$ single crystal consisted of two dif-
ferently orientated domains having the switchable ferroelectric polarization orientated either
normal to the surface (c domain) or parallel to the surface (a domain) as indicated by the
red arrows in the sketch of Fig. 5.18. The sample and the tip were illuminated from the side
using mid-infrared light in the spectral region of the free-electron laser at the FZ Rossendorf
($4 \ldots 22$ μm). Similarly to the previously described setup, the near-field signature was ex-
tracted by demodulating the scattered intensity at higher harmonics of the mechanical oscil-
lation of the AFM cantilever using lock-in technique. The response s_4 at $4 \cdot \omega_{\mathrm{res}}$ recorded while
the oscillating probe (with amplitude $A \approx 20$ nm) slowly approached the BaTiO$_3$ crystal is
displayed for both domains in Fig. 5.18. Similar to the isotropic case, reducing the tip-sample
separation causes a shift of the resonance to larger wavelengths, which arises due to the exci-
tation of and interaction with the near-field-induced SPhP. The different orientations of the
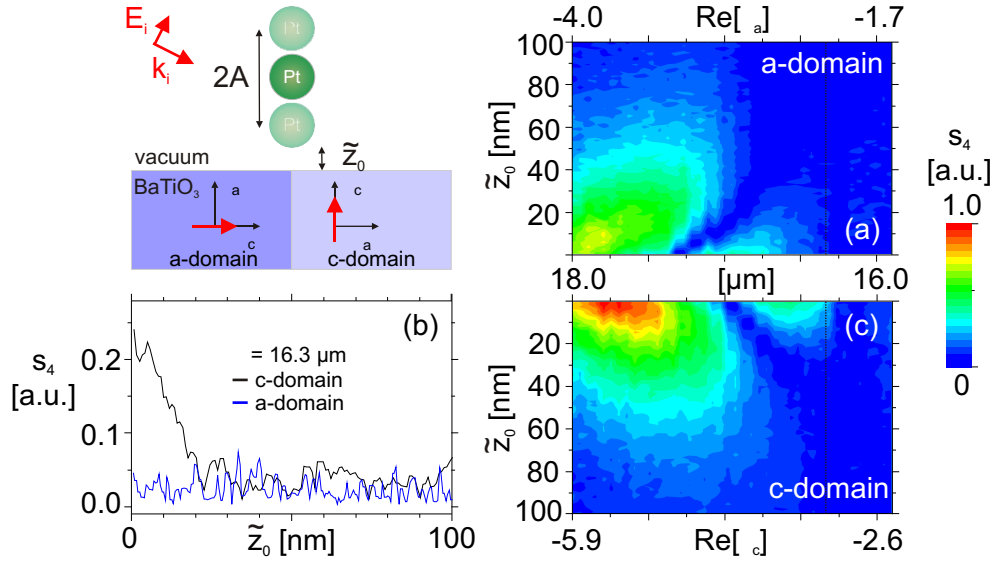
Figure 5.18 *Domain mapping of a ferroelectric BaTiO$_3$ crystal by s-SNOM approach scans in the mid-infrared spectral region. The surfaces of the two domains differ in the SPhP states resulting in different shifts of the maxima in (a) and (c) for a- and c-domains when the probe is approached towards the BaTiO$_3$. Note: The vertical $\widetilde{z}_0$ axis in (c) is flipped for comparison reasons. (b) Approach scan at $\lambda = 16.3$ μm, s_4 increases during the approach only for c-domains. The experimental data are reproduced with kind permission of S. Schneider [126].*

unit cells in the a and c domains with respect to the BaTiO$_3$ sample surface result in different SPhP states, corresponding to the two values ε_a and ε_c along and perpendicular to the surface, respectively. The comparison of Fig. 5.18 (a) and (c) reveals the resulting variation of the near-field coupling between the polarized probe and the substrate.

Beside the distinct difference in spectral position of the maxima, the maximum of s_4 is larger by a factor of 1.5 in the case of a c domain compared to a a domain. The larger spectral redshift in the case of an a domain can qualitatively be understood within the framework of the isotropic model if only the out-of-plane component of the permittivity is taken into account: ε_a is less negative compared to ε_c in this spectral range and, hence, the maximum is located at larger wavelengths.

A more detailed theoretical investigation needs to account for tip and sample anisotropies. This complicated task remains for the future. However, already a modified quasi-electrostatic effective dipole model [127] is able to reveal the underlying mechanism qualitatively.

5.3   Summary: tip-sample interaction

To prevent confusion by the discussion of all the details, we should summarize the main statements of this chapter before leaving the world of localized polaritons:

- Small particles can be used to probe the electromagnetic field locally at optical frequencies in the visible as well as in the infrared spectral region. The probe senses the local electric field $\boldsymbol{E}_{\mathrm{loc}}$ by getting polarized, which leads to a detectable scattering signature. As long as the separation is not very small compared to λ and to the radius at the apex, $\boldsymbol{E}_{\mathrm{loc}}$ is simply given by the incident and reflected, or transmitted waves, respectively. Therefore, $\boldsymbol{E}_{\mathrm{loc}}$ depends on $\varepsilon_{\mathrm{sample}}(\lambda)$, the angle of incidence, and on the polarization.

- The polarized particle induces surface charges at the sample surface which then reinteract with the particle, and so on. This near-field interaction strongly increases for small separations Δ and causes a shift of the resonance frequency of the coupled probe-sample system to lower frequencies.

- The normal mode exhibits a larger shift than the parallel one. This may lead to a mode splitting for particles that are isotropically polarizable in the absence of the interface.

- The different shift and the splitting can be qualitatively well described within the quasi-electrostatic effective dipole model. The reduction of the polarized particle to an effective dipole at the center leads to an underestimation of the spectral shift for small separations Δ. This discrepancy is more pronounced for prolate particles.

- In the case of a probe close to a resonant substrate, e.g. a polar crystal close to the surface phonon frequency, the excitation of localized surface phonon polaritons leads to a strong enhancement of the electric field at the surface.

- The light scattered into the far field is dominated by the dipole radiation of the different modes. Higher-order modes may significantly contribute to the near field for resonant probes, but hardly to the far field. The presence of the substrate strongly modifies the radiation pattern of the dipolar modes. For modes where the probe is polarized normal to the dielectric substrate most light is scattered around the critical angle of total internal reflection. Therefore, high-NA oil-immersion objectives have to be used in the experiments.

- Last but not least, the strong distance dependence of the near-field interaction has to be carefully accounted for, but it also opens up the possibility to discriminate the near field from the background.

The last sentences of this chapter are devoted to excitation issues - not only for the sake of completeness but rather because of its strong impact on the measurement. The symmetry

and geometry together with the dielectric properties define the modes (eigensolutions) of the system, whereas the strength of the partial modes can be controlled by properly choosing the incident wave. For this, the mode overlap has to be considered in general. Comparing the field pattern of the excitation and the one of the mode may help at first glance. In order to excite modes with the polarization normal to the surface, the excitation needs field components along this direction. This cannot be fulfilled at normal incidence (to the interface) in the center of a linearly polarized focused Gaussian beam or by a plane wave. Therefore, one has to go off-axis (see Fig. 5.8), use total internal reflection configurations, or use inhomogeneous polarization modes, for instance focused radially polarized light [128]. The latter features a strong longitudinal electric field component in the focus, which is necessary to excite the modes having the polarization normal to the interface, and therefore, provides high electric fields underneath the tip.

Chapter 6

Excitation and guiding of surface plasmon polaritons

The phenomenon of collectively oscillating charge carriers coupled with photons is not restricted to the localized surface plasmon resonances of nanoparticles studied in the preceding chapters. Longitudinal polarization waves may occur inside the bulk at the plasma frequency ($\varepsilon = 0$) of the material. For $\varepsilon \leq -1$ similar waves exist that decay exponentially perpendicular to the interface, which results in a highly confined field at the boundary. In the visible spectral range, these surface wave solutions of the wave equation are commonly called surface plasmon polaritons *(SPP) if the polarizability of the material originates mainly from the conduction electrons, e.g. in metals or n-doped semiconductors. The detailed knowledge and investigation of these surface states are essential for instance to understand the optical properties of molecules near metal layers in organic light-emitting diodes [17, 129] as well as for novel two-dimensional plasmon-optical (plasmonic) devices [130]. Because of the strong concentration of electromagnetic energy close to the interface, a broad range of surface-sensitive applications have been proven or proposed, such as sensing of surface irregularities [131] and (bio-)chemical sensing.*
The following sections are devoted to the basic properties of SPP needed to construct plasmonic devices, such as excitation, propagation, and scattering of these surface waves present at the interface between two semi-infinite domains.

6.1   Surface plasmon polaritons at planar interfaces

The history of the investigation of electromagnetic surface waves dates back to the beginning of the 20th century. Zenneck [132] in 1907 and Sommerfeld [133] in 1909 demonstrated theoretically that radio-frequency electromagnetic surface waves occur at the boundary of two media if one medium is either a "lossy"dielectric or a metal, and the other is a loss-free

dielectric medium. The first experimental evidence that SPPs contribute to the energy loss of fast electrons in thin-film transmission experiments was found by Powell and Swan [134] in 1960 after the theoretical work by Ritchie [135] published three years before. The coupling of electromagnetic radiation to SPPs was pointed out theoretically again in 1958 by Ferrell [136], including the first published SPP dispersion relation. Later, SPP excitation by light was shown by Otto in 1968 [137] using an attenuated-total-reflection (ATR) setup as well as by Kretschmann and Raether [138] in a similar setup. This Kretschmann-Raether configuration (see Fig. 6.1 (a)) is nowadays widely used for SPP launching in thin metal films.

After this brief historical review we direct our attention back to the physics: Electromagnetic waves propagating in an infinite isotropic medium are transverse ($\varepsilon \boldsymbol{E} \perp \mu \boldsymbol{H} \perp \boldsymbol{k}$) and there are no polarization charges. This situation may change in the case of two different media separated by a planar boundary because the discontinuity of the normal component of the electric field implies the presence of surface charges at the boundary. The continuity of the parallel components of the electric and magnetic fields at the interface leads to solutions [139] of the wave equation having a purely imaginary component $k_\perp$ of the wavevector normal to the interface in the case of adjacent media with permittivities ε_1 and ε_2 having opposite signs. These evanescent surface waves are called surface plasmon/phonon polaritons, depending on the origin of the negative permittivity close to a resonance of the polarizability of the material. The parallel component of the wavevector $k_{\parallel,\mathrm{SPP}}$ has to be continuous for these waveguide modes due to the translational symmetry along the boundary, whereas the decay constant normal to the interface $k_{\perp,i}$ differs drastically for the two different media:

$$k_{\parallel,\mathrm{SPP}} = \frac{\omega}{c} \left[\frac{\varepsilon_1 \varepsilon_2}{\varepsilon_1 + \varepsilon_2} \right]^{\frac{1}{2}} = k_x, \tag{6.1}$$

$$k_{\perp,i} = \left[\varepsilon_i \left(\frac{\omega}{c} \right)^2 - k_\parallel^2 \right]^{\frac{1}{2}} = k_{z,i}. \tag{6.2}$$

The field modulation period (Λ_{SPP}) of the SPP given by:

$$\Lambda_{\mathrm{SPP}} = \frac{2\pi}{k_\parallel}, \tag{6.3}$$

is smaller than the wavelength λ of the light in the dielectric. Consequently, the resulting dispersion relation of the SPPs lies to the right of the light line for frequencies below the surface plasma frequency ω_{SP} as shown in Fig. 6.1 (b) by the blue solid curve. Hence, the momentum of the plasmon is larger than that of propagating plane waves. Therefore the direct excitation of SPPs at planar surfaces is prohibited because of the requirement of both energy and momentum conservation (at a translationally invariant interface).

The two slightly different SPP dispersion relations displayed in Fig. 6.1 (b) are worth being examined more closely. The blue solid curve corresponds to the one displayed in many text-books assuming a purely real $\varepsilon_{\mathrm{metal}}$, whereas the blue dotted curve accounts for the imaginary part as well, resulting in a "back-bending" at ω_{SP}. None of them is wrong as proven by ATR
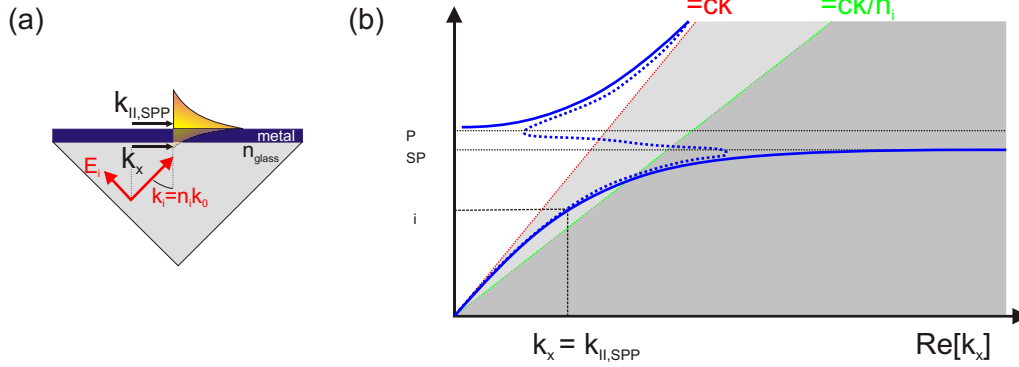
Figure 6.1 *(a) Kretschmann-Raether configuration: The incident light partially penetrates through the metallic thin film and may excite the SPP at the vacuum/metal interface if $k_{\parallel,\mathrm{SPP}} = k_x = n_{\mathrm{glass}}k_0 \sin(\phi)$. (b) The SPP behavior is similar to that of transverse light waves for small k_x and changes towards mainly longitudinal character at large k_x. The SPP dispersion shows a back-bending (blue dotted curve) depending on whether k_x or ω is assumed to be real.*

experiments for silver performed by Otto [137] and Arakawa *et al.* [140]. Both are even in accordance with Fresnel's equations [141]. Therefore, the result of the measurement at any lossy material ($\mathrm{Im}[\varepsilon_{\mathrm{metal}}] \neq 0$) is influenced by the way the experiment is performed. Either the frequency dependence of the reflectivity ($\mathrm{R}(\omega)$) is measured at a fixed angle of incidence (fixed k_x/k_0), or $\mathrm{R}(\phi)$ is observed at a fixed frequency during an angular scan [141, 142]. In the latter case, a back-bending is observed in the frequency range between the bulk plasma frequency $\omega_{\mathrm{P}}(\varepsilon_{\mathrm{metal}} = 0)$ and $\omega_{\mathrm{SP}}(\varepsilon_{\mathrm{metal}} = -1)$ where no "true"surface modes exist [142, p. 29].

Coming back to a more application-driven question: How efficiently can light be transported by SPPs? The propagation length δ_{SPP}, characterizing the distance of the $1/e$ decrease of the energy, is determined by the imaginary part of $k_{\parallel}$ and can be calculated [10, 143] from the dielectric functions of the metal, $\varepsilon_1 = \varepsilon_1' + i\varepsilon_1''$, and of the nonabsorbing dielectric, ε_2:

$$\delta_{\mathrm{SPP}} = \frac{1}{2\,\mathrm{Im}[\mathrm{k}_{\parallel}]} = \frac{c}{\omega}\left(\frac{\varepsilon_1'\varepsilon_2'}{\varepsilon_1' + \varepsilon_2}\right)^{\frac{3}{2}}\frac{(\varepsilon_1')^2}{\varepsilon_1''}. \tag{6.4}$$

The attenuation of the SPP along the propagation direction (along the interface) is caused by the losses (absorption) in the metal[1] if a lossless dielectric is assumed. Fig. 6.2 displays the propagation length δ_{SPP} for some metals from the ultraviolet (UV) to the near-infrared spectral range. The surface plasma frequency of the metal limits the existence of SPPs in

---

[1]The system under consideration consists of two different semi-infinite half-spaces separated by a planar interface, hence scattering of the SPP or conversion to a leaky mode (see chapter 7) are not possible.
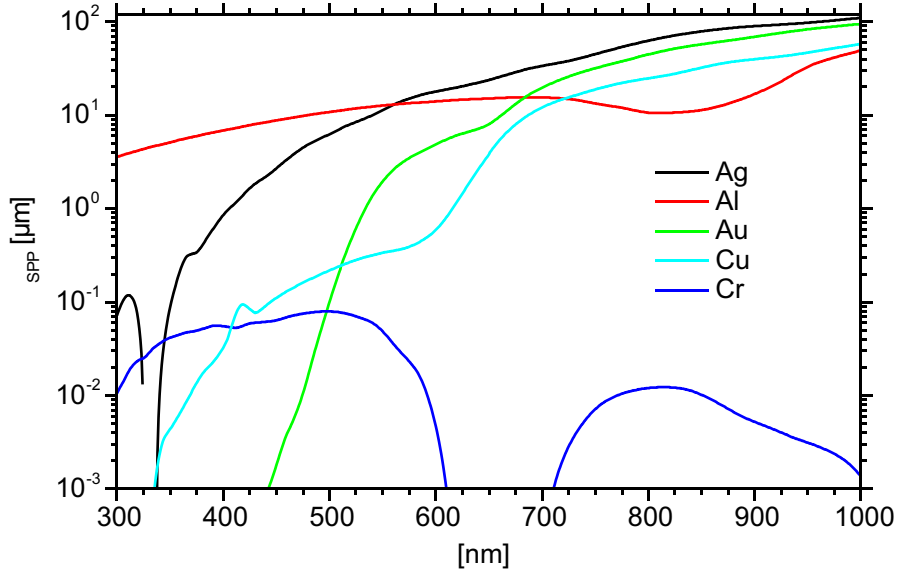
Figure 6.2 *The propagation length of SPPs at a planar metal surface assuming $\varepsilon(\lambda)$ for Ag, Al, Au, Cu, and Cr from Ref. [45]. The SPPs are strongly damped close to the plasma frequency of the metals (blue, UV spectral region), but their propagation length increases to micrometer dimensions towards the (infra-) red spectral range because of the longer wavelength and the smaller damping. For highly absorbing metals such as chromium the SPPs are nearly suppressed.*

the blue and ultraviolet region for noble metals. For lower frequencies and in the absence of interband transition, the value of δ_{SPP} increases and goes up to mesoscopic values in the red and infrared range. Especially noble metals such as Ag and Au have low internal losses at long wavelengths and are suitable for SPP devices. Materials having high losses, such as Cr, strongly suppress SPP propagation. Hence, Cr is more often used for lithography masks to block the light by reflection and absorption.

Several possibilities to overcome the problem of the momentum mismatch have been proposed and already proven, namely the above-mentioned ATR [137] or Kretschmann-Raether [138] method as well as grating coupling. These methods can be used to excite the SPP on large areas by plane waves, beams with a finite width [144] or slightly focused beams [145], but the minimum spatial extension of the SPP excitation "spot" is typically in the order of some tens of micrometers [145, 146]. That value is comparable with δ_{SPP} in the visible spectral range and not appropriate for nano-optical devices. Instead of exactly matching the momenta, it is also possible to overcome the requirement of momentum conservation simply by destroying the translational symmetry along the interface by introducing edges and steps or by placing particles nearby. The local near fields at the discontinuity consist of a broad momentum range rather than a fixed value like at a planar interface. Illuminating the end face of metallic

waveguides by a focused beam can be used for SPP excitation [147]. Therefore, the excitation can be confined to sub-micron areas determined by the diffraction-limited focus diameter.

6.2 Excitation of SPPs at a finite number of grooves

Let us look at the possibility and the quantitative efficiency of SPP excitation at patterned metallic interfaces in the case of rectangular grooves. The translational symmetry is now broken by these structures, which allows the excitation of SPPs similar to SPP excitation at the end face of a metallic waveguide. In contrast to the end face problem in Ref. [147], the incident electric field is now assumed to be parallel to the interface.

The questions that are addressed in the following are: How does the excitation efficiency depend on the geometry, e.g. width and depth of the groove? Is it possible to further increase this value by additional structures that are placed close by?

6.2.1 Single groove

The investigation starts with a single rectangularly shaped groove in a metallic half-space made of aluminum ($\varepsilon_{\mathrm{Al}}(\lambda = 633\,\mathrm{nm}) = -56 + 21i$ [45]), which is illuminated by a TM-polarized plane wave having an angle of incidence of 90° measured in respect to the horizontal metal surface as schematically drawn in Fig. 6.3 left panel. The symmetry of both the geometry and excitation was used to speed up the calculation of this essentially two-dimensional problem. Furthermore, all edges occurring in Fig. 6.3 left panel were rounded ($\rho = 15$ nm).

  The efficiency of the excitation of the surface wave strongly depends on both geometrical parameters w and d, as displayed in Fig. 6.3 right panel. The color scale represents the SPP excitation cross section σ defined as the ratio of the power carried by the outgoing SPP (only one direction) to the power incidents on the horizontal surface per nanometer.

Looking at the dependence on w at a fixed small d (corresponding to a horizontal cut in Fig. 6.3) reveals a minimum in the energy coupled to the SPP slightly below $\lambda = 633$ nm around 600 nm and maxima below $\frac{\lambda}{2}$ as well as near $\frac{5}{4}\lambda$. This dependence on w can be understood from the surface charges induced by the time-harmonic incident wave. The surface vectors normal to the vertical sides of the rectangular groove point in opposite directions. Hence, the induced surface charges near the edges are always signed oppositely. Therefore, the electromagnetic fields radiated by the two edges are phase-shifted by π, and on the way to the other edge they undergo an additional phase shift Φ_{path} depending on w. For $w \approx \lambda$, the phase shift is $\Phi_{\mathrm{path}} \approx 2\,\pi$ leading to a destructive overall interference ($\Phi_{\mathrm{path}} + \pi$) and a poor efficiency. The corresponding minimum at $w \approx 600$ nm occurs at w slightly smaller than the wavelength, most probably because of the finite field penetration into the (good but not perfect) metal, which has a finite conductivity (skin depth). A smaller value of w around $\frac{\lambda}{2}$ results in a phase shift $\Phi_{\mathrm{path}} \approx \pi$ and constructive interference and, hence, efficient SPP excitation. A further decreasing of w reduces the phase shift Φ_{path}, resulting in an overall
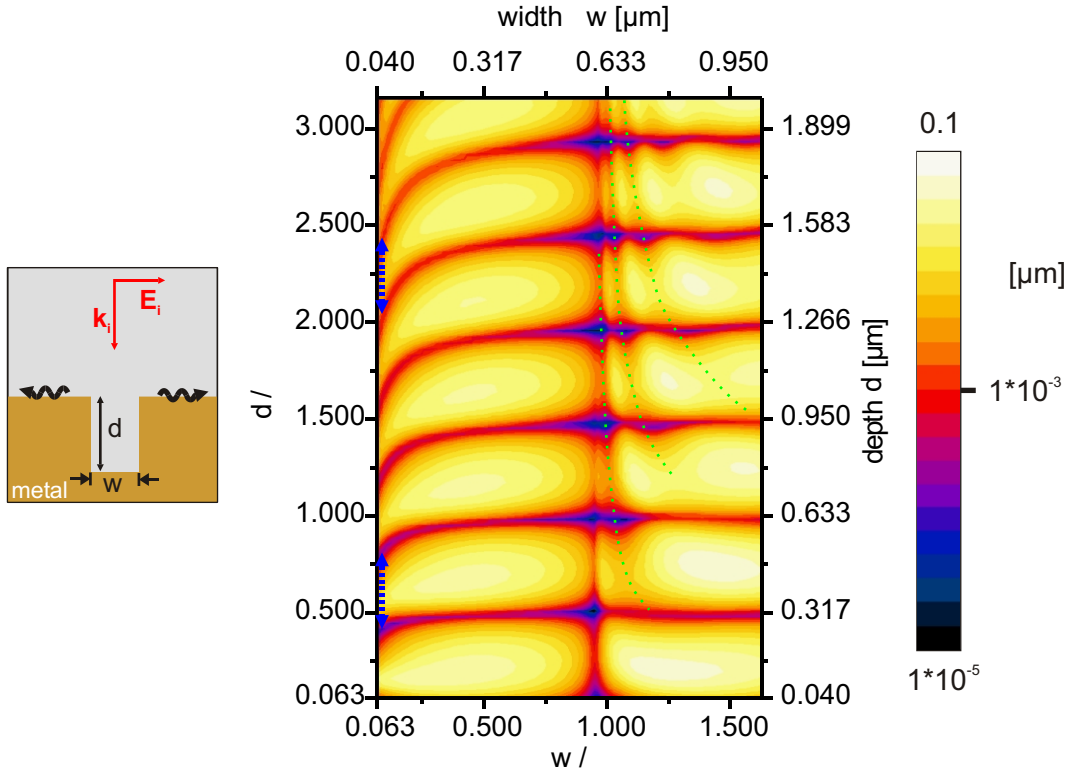
Figure 6.3 *SPP excitation cross section σ for a rectangular groove illuminated by a plane wave. Successive colors differ by a factor of 1.5 in energy. For $w < 600$ nm only the fundamental mode in the groove can be excited. The propagation constant of this mode increases for decreasing w, resulting in a reduced distance between the minima along the d axis as illustrated by the blue arrows. The contribution of the higher-order modes can be seen for $w > 600$ nm. All of them become more and more evanescent when w is reduced towards 600 nm. The green dotted lines emphasize the resulting modulation of σ.*

phase difference closer to π.

The dependence on the depth further complicates the situation owing to two effects:

- The incident field which enters into the groove excites waveguide mode(s) inside the groove, which are mostly back-reflected at the bottom, building up a cavity characteristic. The superposition of the counterpropagating modes may result in a minimum of the field at the edge, hence minima in σ at multiples of $d \approx m\frac{\Lambda_{\mathrm{gap},0}}{2}$ with $m = [1, 2, ..]$ can be seen[2].

- The value $\Lambda_{\mathrm{gap,i}}$ for the different modes inside the groove is close to Λ_{SPP} (SPP at a

---

[2]$\Lambda_{\mathrm{gap},0}$ is defined according to Eq. (6.3) using the propagation constant of the fundamental TM_0 cavity mode $k_{\mathrm{gap},0}$ instead of $k_{\parallel}$. The complex values of $k_{\mathrm{gap,i}}$ are the (numerical) solutions of the waveguide eigenvalue problem (see Fig. 6.4).

planar interface) only for $w \geq \frac{\lambda}{2}$ and far away from the cut-off width of the mode. The fundamental TM_0 mode does not have a cut-off width, but both the real and the imaginary parts of the propagation constant increase when w is reduced, resulting in a higher damping and smaller $\Lambda_{\text{gap},0}$ as illustrated in Fig. 6.4. Hence, the maxima of σ are more closely spaced for $w \ll \frac{\lambda}{2}$ as can be seen in Fig. 6.3. For $w > \lambda$ higher-order modes occur. All of them become evanescent around $w \approx \lambda$. The real part of the propagation constant goes to zero, whereas the imaginary part strongly increases for $w \to \lambda$. This different behavior of the propagation constants of the higher-order modes as compared with the fundamental mode can easily be seen as an opposite upward "bending" of the minima in Fig. 6.3 for $w \to 600$ nm, as emphasized by the green dotted lines.
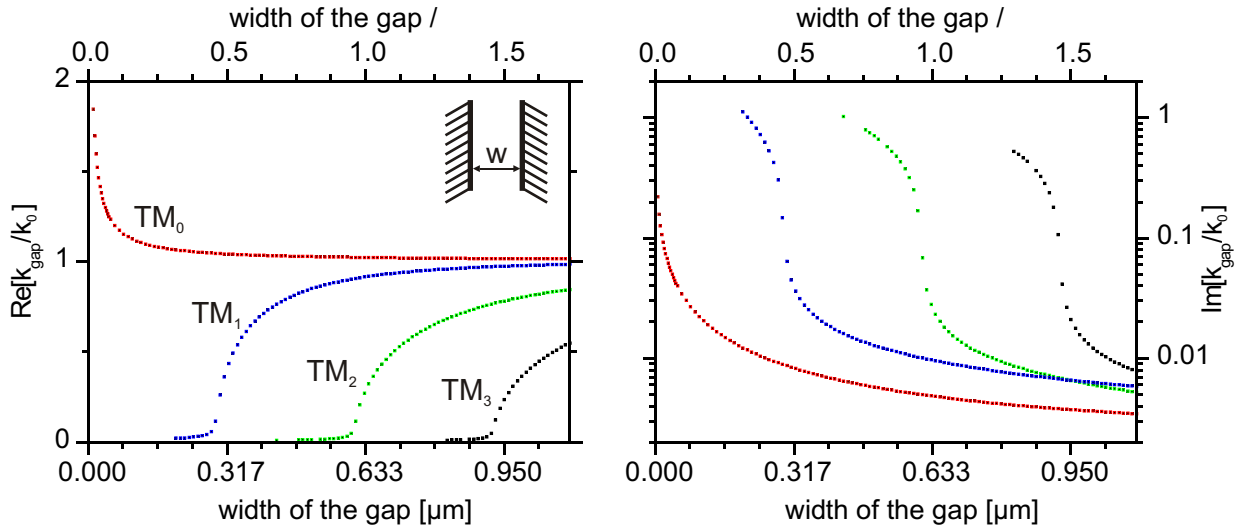
Figure 6.4 *The propagation constant $k_{gap,i}$ calculated for a small vacuum gap w between two thick Al plates ($\varepsilon_{\text{Al}}(\lambda = 633 \ nm) = -56 + 21i$). The higher-order modes exhibit a cut-off behavior ($\text{Re}[k_x]\downarrow$, $\text{Im}[k_x]\uparrow$ for $w \downarrow$), whereas for the fundamental TM_0 mode no cut-off exists ($\text{Re}[k_x]\uparrow$, $\text{Im}[k_x]\uparrow$ for $w \downarrow$). The odd-numbered modes cannot be excited using the setup of Fig. 6.3 because of the symmetry of the incident wave and the geometry.*

The maximum of the SPP excitation magnitude for small and shallow grooves occurs for a groove being 240 nm wide and 120 nm deep. The corresponding coupling cross section is $\sigma \approx 65$ nm for each of the two possible SPP propagation directions. Hence, roughly 55 % of the light incident onto the 240-nm-wide groove is converted into SPPs.

For grooves having larger w and d, the value of σ can be even higher but they are less efficient with regard to the ratio of energy of the surface wave to the one incident onto the groove.

6.2.2   Multiple grooves

The SPP excited at a single groove may be further enhanced by placing additional grooves beside the first one only if the surface waves excited at the individual steps interfere constructively. Therefore, the discontinuities have to be separated by precise distances as investigated by Ditlbacher *et al.* [148] for the slightly different case of stripes of gold (instead of grooves) on a gold film.

In the present simulation, the distance between two or three equi-shaped grooves in the Al surface was varied. The rounded, rectangularly shaped cross section ($w = 240$ nm, $d = 120$ nm, $\rho = 15$ nm) of the grooves was adjusted to nearly fit the maximum of σ (see Fig. 6.3).
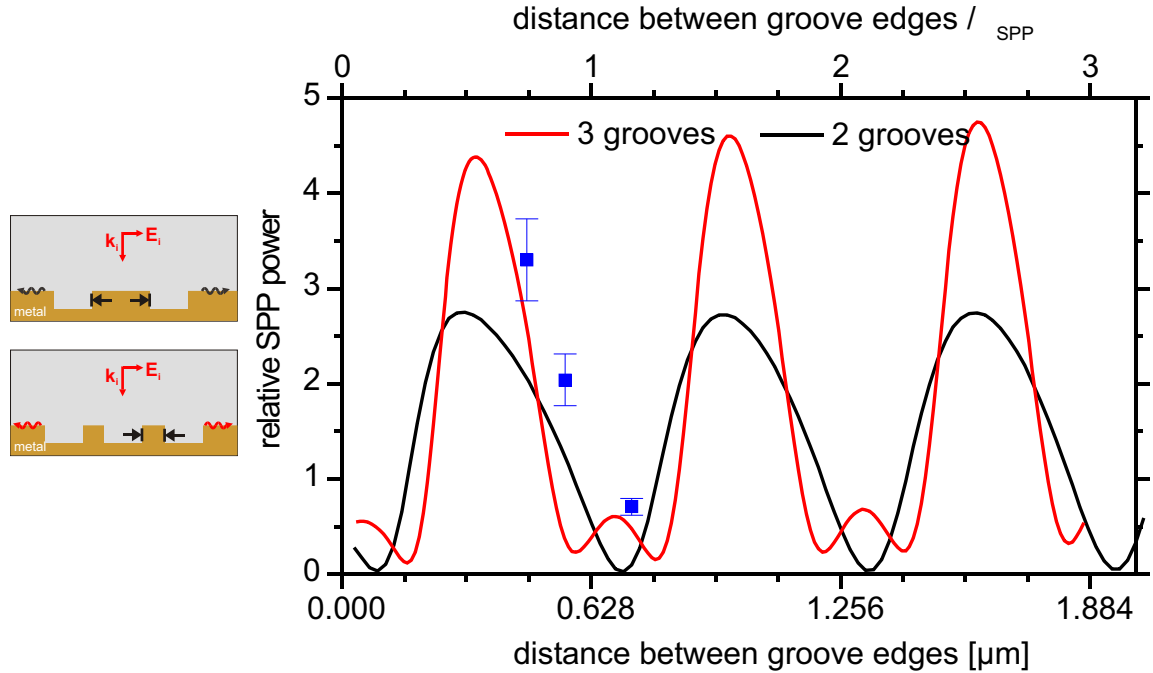
Figure 6.5   *The SPP excitation efficiency obtained when a finite number of equishaped grooves is illuminated peaks at a separation of the edges $\Delta \approx \Lambda_{\mathrm{SPP}}/2$ and odd multiples thereof. These resonant structures couple 2.7 (double groove) or 4.5 (triple groove) times more efficiently than a single groove. The points marked in blue represent the wavelength-scaled experimental data taken from Ref. [148] for a triple stripe on gold arrangement.*

The relative SPP energy plotted in Fig. 6.5, defined as the power carried by the SPP in the multiple-groove arrangement divided by the power of a single groove, shows an oscillation period close to Λ_{SPP}. At the maxima close to $\Delta \approx (2l - 1) \cdot \Lambda_{\mathrm{SPP}}/2$ with $l = [1, 2, 3 \ldots]$, the SPPs excited at every single slit interfere constructively in a similar manner as presented in the former section. Therefore, the SPP is stronger in intensity by a factor of 2.7 (double groove) or 4.5 (triple groove), respectively. This gain obviously exceeds the doubled or

tripled geometrical "active" area, reflecting the fact that the electromagnetic field near the groove edges is modified because of the presence of the neighboring groove. This leads to a more "plasmon-like" surface charge distribution at the multiple grooves. Hence, the light-to-SPP coupling increases. The smaller local maxima in the triple-groove setup at $\delta \approx 0.68$ μm and 1.315 μm originate from a constructive interference of the two outer slits.

The efficiency of local light-plasmon coupling measured by Ditlbacher *et al.* [148] for an illuminated single gold stripe ($h = 60$ nm, $w = 200$ nm) on a thin gold film with a thickness $h = 43$ nm was 4.5 % at $\lambda =$800 nm. The coupling efficiency in a triple-stripe arrangement was increased up to three times or even reduced below one as indicated by the blue points in Fig. 6.5. For the sake of comparability, the distance between the stripe edges was normalized to $\Lambda_{\mathrm{SPP}} =$783 nm in order to account for the different wavelength $\lambda = 800$ nm used in the work of Ditlbacher *et al.* The experimental data are in fair agreement to the theoretically predicted ones and the remaining differences may be attributed to the different geometry (stripes instead of grooves) and uncertainties in the values of the separation (no confidence range noted in Ref. [148]). The SPP intensity could be further increased if the spacing between the centers of the grooves/ridges ($= \Delta + w$) is decreased to 600 nm, at least theoretically. On the other hand, the sharpness of the maxima requires the grooves to be manufactured with a tolerance of less than 5 % of Λ_{SPP} for the triple-groove arrangement, which poses a serious experimental challenge.

6.3 Interaction of SPPs with edges, grooves, and barriers

The SPP excitation at multiple points discussed in the preceding subsection is only one part of the whole plasmonics story. Another important point is: How do SPPs interact with nanopatterned surfaces, e.g. grooves or barriers etc. placed in their path of propagation? Furthermore, patterned plasmonic surfaces may alter the density of electromagnetic surface states. Especially in a plasmonic bandgap, the reduced density of surface states can be used to suppress the energy loss of excited molecules to SPPs as shown by Barnes *et al.* [129]. Therefore, one may improve the performance of thin-film devices such as organic light-emitting diodes by such nanoengineered plasmonic surfaces. Furthermore, SPPs attract a lot of attention because of their inherent high sensitivity to surface irregularities and because of potential sensing applications based on it.

The following investigation picks up several important points from the huge plasmonic playground, aiming to elucidate the basic physical mechanisms rather than to present a complete survey of all different effects. Starting from the most simplest geometrical features such as edges and walls, we proceed to the SPP interaction with steps, barriers, and grooves. The detailed discussion below presents the transmission (t) and reflection (r) coefficients for different configurations. The amplitudes of t and r have been corrected with respect to internal losses for the various geometries. More explicitly: $t^2 = 1$ means 100 % transmission, and $r^2 = 1$ is

equal to 100 % reflection independent of the size of the groove/barrier. The majority of calculations have been carried out assuming aluminum at $\lambda = 633$ nm as the material of choice from a practical point of view as will be explained later. The permittivity at this wavelength is $\varepsilon_{Al} = -56 + 21i$ [45]. Therefore, the results should also be representative for other spectral ranges where the material is still a good but not perfect conductor or even other materials such as Au, Ag, or Cu in the near infrared region around $\lambda = 1100$ nm, where $\mathrm{Re}(\varepsilon_{\mathrm{metal}})$ is comparable to the value assumed here.

6.3.1   Edge and step interaction

SPP hitting an end face

A SPP propagating along an planar interface that abruptly ends by a 90 degree wall or precipice is one of the most basic situations imaginable. This non-trivial problem was the scope of certain earlier investigations in the eighties [149, 150] using shortening planes to simplify the problem (finite number of modes instead of infinite number). Later, in 1985, a more rigorous numerical analysis presented by Jamid and Al-Bader [151] revealed that an additional SPP is excited at the vertical boundary (labelled SPP_{trans} in Fig. 6.7). They used the method of lines (see Ref. [151] and references therein) to solve the problem and assumed a lossless material (real ε) and a sharp corner at the edge. The more realistic situation characterized by a rounded edge of radius ρ, or more generally spoken, the propagation of SPPs on curved surfaces was studied recently by Hasegawa *et al.* [152] in the short-wavelength limit ($k\rho \gg 1$) on the basis of the known analytical solution for SPP propagation around a cylinder [153]. The SPP propagation at non-planar interfaces is not only interesting from an academic point of view. It also sets fundamental limits to the energy transport on the nanoscale in non-planar plasmonic devices.

SPP at an end face - precipice

In the first case, let us focus at the setup sketched on the left side of Fig. 6.6. The SPP incident from the left hits the 90° end face of an aluminum ($\varepsilon_{Al}(\lambda = 633$ nm$) = -56 + 21i$) block. At this precipice, most of the surface wave is forward scattered into the vacuum because the oscillating surface charges at the edge form an efficient radiation source in the absence of translational symmetry [150]. As displayed in Fig. 6.7, a small reflected portion SPP_{ref} ($r^2 < 0.2\%$) was found only for sharp corners ($\rho \ll \Lambda_{SPP}$). This backward-propagating SPP is clearly weaker than the SPP excited at the vertical boundary, SPP_{trans}, but both portions decrease for increasing radius of the edge. The decreasing reflection coefficient for large radii can be understood as a result of a smeared-out potential barrier, but the likewise decreasing value of SPP_{trans} even at $10 \cdot \Lambda_{SPP}$ is surprising. This partially counterintuitive weak guiding is caused by the absence of a second boundary as present in the case of a dielectric slab waveguide. Therefore, the oscillating surface charges at the edge can radiate very efficiently
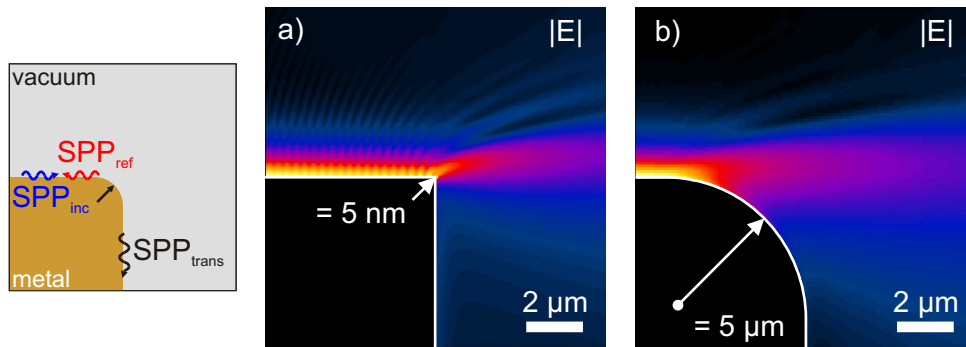
Figure 6.6 *The interference visible in the* $|E|$ *pattern a) originates from the superposition of the incident SPP and the reflected portion. The latter is present only at a sharp corner, e.g.* $\frac{\rho}{\lambda} = \frac{5 \ nm}{633 \ nm}$, *whereas* SPP_{ref} *vanishes for larger radii* ρ *as shown in b) for* $\frac{\rho}{\lambda} = \frac{5 \ \mu m}{0.633 \ \mu m}$.

into the vacuum, which provides a continuum of electromagnetic modes rather than a set of discrete modes like in a dielectric slab waveguide.

Analyzing the dependence of the transmission and reflection on the radius of curvature of the edge is only one cut through the multidimensional parameter space needed to characterize the edge problem. The value of $\varepsilon_{\mathrm{metal}}$ is another important parameter, which can be optimized to a certain degree in practice either by changing λ or the material used. In order to illustrate the role of $\varepsilon_{\mathrm{metal}}$, let us for the sake of simplicity assume an artificial metal characterized
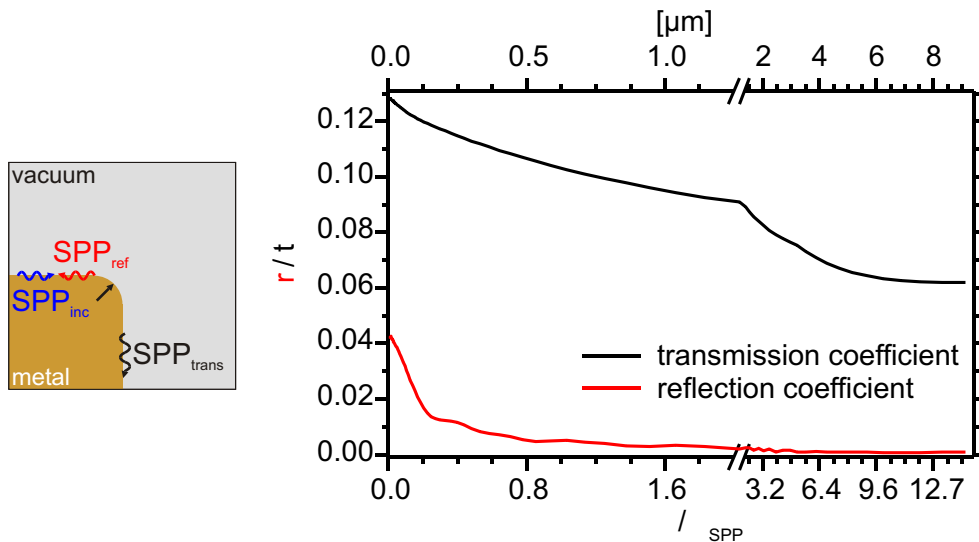

Figure 6.7 *A SPP hitting an end face at a precipice radiates very efficiently into the vacuum. Only a minor portion is reflected at very sharp edges or propagates around the edge.*

by a purely real permittivity $\varepsilon_{\mathrm{metal}}$ ($\mathrm{Im}[\varepsilon_{\mathrm{metal}}] = 0$). In this case $k_{\parallel}$ is purely real, too, and the SPP will propagate without damping. Looking at the reflection and transmission coefficient for the two extreme cases displayed in Fig. 6.8 reveals the main dependencies. The amplitude of the reflected SPP for a smooth edge having $\frac{\rho}{\lambda} = \frac{4\ \mu\mathrm{m}}{0.633\ \mu\mathrm{m}}$ is negligible as expected, except close to the surface plasma frequency ω_{SP} ($\varepsilon_{\mathrm{metal}} = -1$). In the case of a very sharp edge $\left(\frac{\rho}{\lambda} = \frac{5\ \mathrm{nm}}{633\ \mathrm{nm}} \right)$, the SPP is much more strongly reflected at the edge. Far away from ω_{SP}, the fraction of the SPP power propagating inside the metal decreases towards more negative values of $\mathrm{Re}[\varepsilon_{\mathrm{metal}}]$ as displayed by the blue curve in Fig. 6.8. Hence, most of the electromagnetic energy propagates in the vacuum, while only little energy is transported inside the metal for $\mathrm{Re}[\varepsilon_{\mathrm{metal}}] \ll -1$. Therefore, the metal end is of minor importance leading to a decrease of the reflection for $\mathrm{Re}[\varepsilon_{\mathrm{metal}}] \ll -1$. The crossing of the two transmission curves at $\mathrm{Re}[\varepsilon_{\mathrm{metal}}] \approx -12$ implies that, for frequencies corresponding to $\mathrm{Re}[\varepsilon_{\mathrm{metal}}] < -12$, the SPP propagation around a sharp 90° bend is more efficient than around a smooth one. The behavior closer to ω_{SP} is much more complicated because the SPP may couple resonantly to the modes of the cylinder at the edge [152]. Their impact can also be seen in the transmission behavior. The ε values (spectral positions) at which the different modes of a metal cylinder in vacuum are in resonance change depending on the value of $k\rho$ [153]. The MMP solutions displayed in Fig. 6.8 reveal the resonance in $\mathrm{SPP}_{\mathrm{trans}}$ for
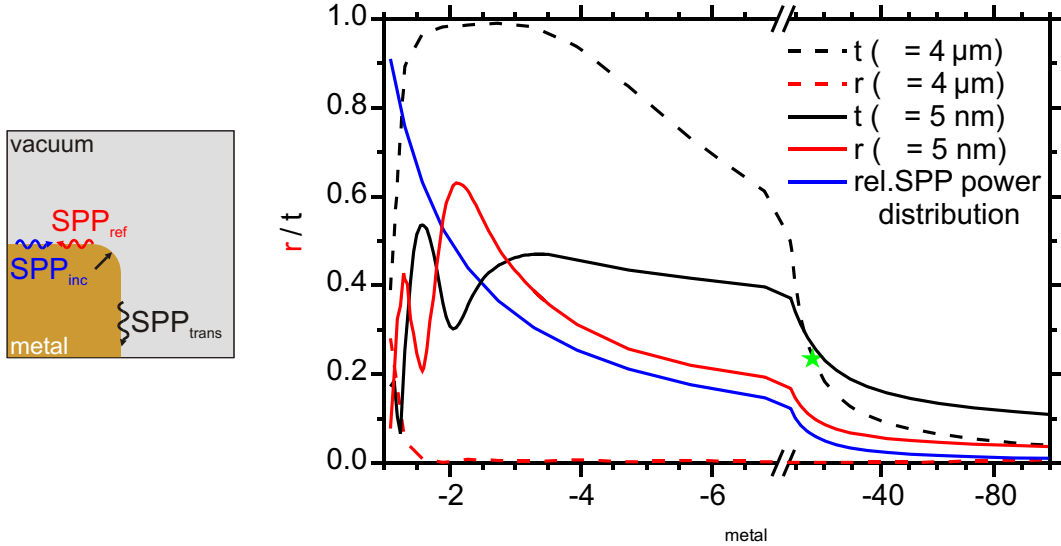
Figure 6.8 *SPP reflection and transmission at a sharp ($\rho = 5$ nm) edge (solid curves) is dominated by the coupling to the cylinder modes at the edge for $\mathrm{Re}[\varepsilon_{\mathrm{metal}}] = -1 \ldots -3$. For smooth edges, r nearly vanishes and t reaches 100 % for $\mathrm{Re}[\varepsilon_{\mathrm{metal}}] = -2.7$. The blue curve represents the power distribution between both half-spaces defined as $\sqrt{\frac{P_{\mathrm{metal}}}{P_{\mathrm{vacuum}}}}$. The value of t reported in Ref. [151] is indicated by the green asterisk.*

$\rho = 5$ nm at $\varepsilon_{\mathrm{metal}} = -1.6$, whereas SPP$_{\mathrm{ref}}$ has a minimum at this point. On either side of this resonance, SPP$_{\mathrm{ref}}$ shows a maximum and conversely there are two minima in SPP$_{\mathrm{trans}}$. In the other case of a smooth edge having $\rho = 4$ μm, the transmission has a broad maximum around $\varepsilon_{\mathrm{metal}} \approx -2.7$, where $t > 0.99$, instead of a sharp resonance. This difference has to be attributed to the smaller damping of the higher-order modes of the cylinder for larger ρ. Additionally, these modes become more and more degenerate for $k\rho > 1$ [153], resulting in an improved mode matching between the incident SPP and the mode propagating around the cylinder.

The values of the reflection and transmission coefficients are strongly dependent on $\varepsilon_{\mathrm{metal}}(\lambda)$ and the geometry of the edge, as illustrated by the last three figures. As shown, large SPP transmission around bends requires that a significant amount of the SPP resides in the metal. This is a dilemma from a practical point of view: A strong localization of the SPP within the metal is synonymous to a short propagation length δ_{SPP} because of the intrinsic absorption within the metal. Therefore, one has to use more sophisticated arrangements that suppress the forward radiation by imposing additional boundary condition similar to photonic crystals. At this point, the further discussion of SPP reflection at the edge of a precipice will be stopped. Especially the comparison to experiments is postponed to section 7.2.1 because there, mostly thin metal films are used rather than metal half-spaces.

SPP at an end face - metal wall

The complementary situation to a precipice will now be investigated, namely a SPP running against a wall as sketched in Fig. 6.9 left panel. The SPP incident from the left hits the 90° aluminum ($\varepsilon_{\mathrm{Al}}(\lambda = 633$ nm$) = -56 + 21i$) end face. In contrast to the former case, the reflected portion plotted in Fig. 6.9 is very large for small radii and decreases monotonically for larger ρ. The high reflectivity at low ρ can be explained by the power distribution displayed in Fig 6.8. Placing a wall into the vacuum half-space causes a strong reflection because most of the SPP propagates within this domain for the chosen value of $\varepsilon_{\mathrm{Al}}$ and senses the strong contrast of the permittivity. The amount of SPP$_{\mathrm{trans}}$ propagating into the 90° bent direction shows several resonances instead of a monotonic increase in this mesoscopic regime where $\rho \gtrsim \Lambda_{\mathrm{SPP}}$.

SPP hitting a tiny step

After studying the simplest configurations of an abrupt end of the metal surface or a metallic wall, a step-like change in the profile of the SPP-active interfaces will be considered now. Such a step may unintentionally result from a tiny misalignment, a substrate irregularity, or partial etching during a lithography process. The importance of flat surfaces for an undisturbed propagation of the SPP will be illustrated now for the case of two slightly shifted metal surfaces as sketched in the insets of Fig. 6.10. The SPP is incident from the left and hits
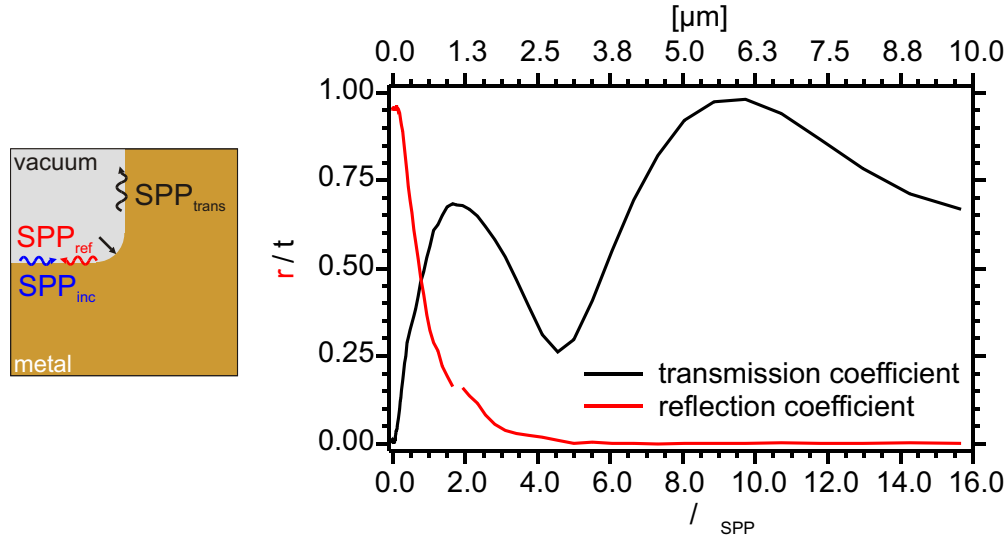
Figure 6.9 *A SPP which hits a wall is mostly back-reflected for sharp edges. The transmission around the edge is not a monotonically increasing function for larger radii and shows resonances in this mesoscopic regime.*

the step. Irrespective of whether it is an upward or downward step, an increase of the step height $|h|$ always decreases the transmitted portions t_{up} and t_{down} in a similar way. But the reflection coefficients r_{up} and r_{down} behave differently:

- For the downward step, r_{down} stays nearly constant, showing only a small oscillation which is caused by the SPP excited at the edge which propagates along the vertical boundary and gets mostly back-reflected at the bottom surface. Therefore, these SPPs obey a cavity characteristic as a function of h. For increasing h, the portion scattered into the vacuum also increases as indicated by the difference between the dotted blue curve in Fig. 6.10 (which nearly coincides with t) and unity.

- A SPP which hits an upward step is reflected much more strongly - even at moderate h. The oscillation is much less pronounced than in the former case because the amplitude of the SPP excited at the vertical boundary is negligible in the case of a wall rather than a precipice (see Fig. 6.7 and Fig. 6.9). The gentle oscillation of t_{up} and r_{up} is most probably a consequence of the upper edge still partly sensing the incident SPP. Hence, a SPP propagating at the vertical boundary is excited that modifies t_{up} and r_{up}. The amount of the SPP scattered into the vacuum is reduced because of the dominant reflection for increasing h.

The results displayed in Fig. 6.10 are in good qualitative agreement with the simulation results obtained by Jamid and Al-Bader [154] using the method of lines. The small quantitative differences arise most probably from the different dielectric properties assumed. They assumed
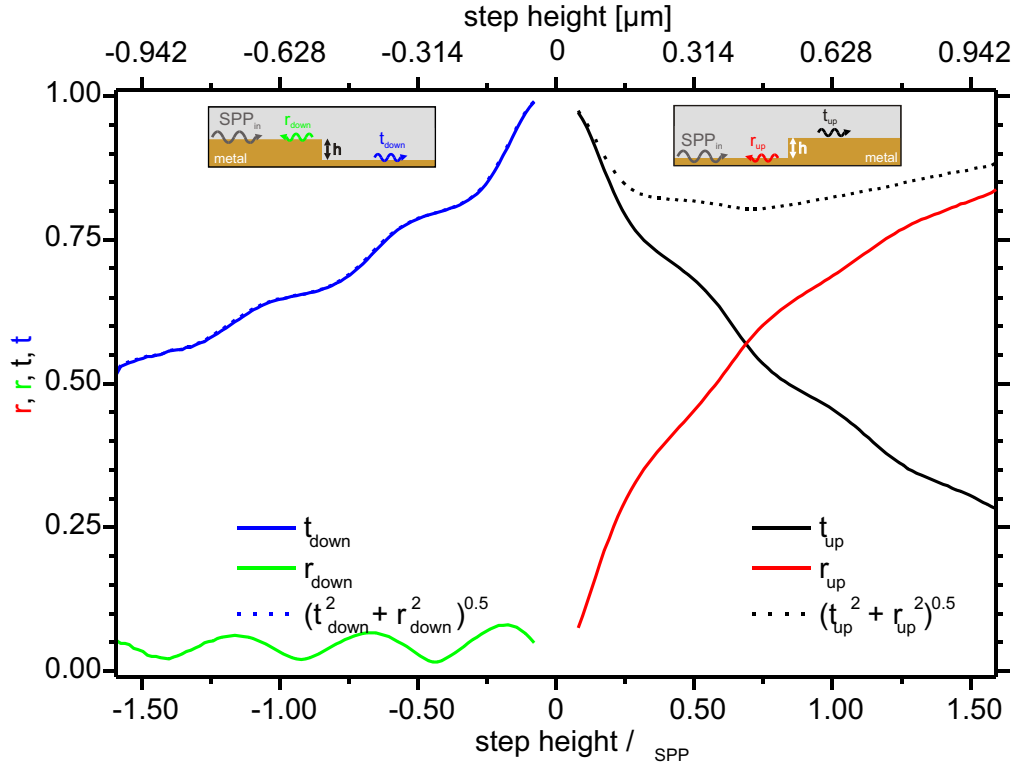
Figure 6.10 *The SPP transmission and reflection coefficients across a tiny step depend on the direction of the incident SPP. This lack of reciprocity is caused by the mismatch of the fields across the step.*

a purely real permittivity of silver ($\varepsilon_{\mathrm{Ag}}(\lambda = 633$ nm$) = -16$). Consequently, the portion of the SPP propagating inside the metal is slightly higher for Ag than for Al (see Fig. 6.8). Hence, in the case of a downward step, the reflected portion was higher than displayed in Fig. 6.10. Similarly, the different $\varepsilon_{\mathrm{Ag}}$ and, hence, $k_\parallel$ affects also the decay of the field normal to the interface according to Eqs. (6.1) and (6.2). Consequently, the transmission reported in Ref. [154] falls more rapidly with increasing $|h|$.

In conclusion: The correct alignment of plasmonic surfaces is very critical for an undisturbed SPP propagation, because the larger the mismatch of the SPP fields on the two sides (due to the shift in height), the smaller is the transmitted portion of the SPP. The dependence on the direction (step up- or downward, respectively) was explained by Maradudin *et al.* [150] as a non-reciprocity because of the generation of both radiative and non-propagating modes contributing to the transmission and reflection phenomenon.

6.3.2   Barrier interaction

The geometrical features studied above can be superimposed on each other to form a partial barrier having a rectangular cross section with a finite height as depicted in the inset in Fig. 6.11. Related investigations assuming a Gaussian-shaped surface defect were published by Sánchez-Gil and Maradudin [158, 159], revealing a crucial dependence of SPP_{ref}, SPP_{trans}, and the far-field-scattered portions on the geometrical features. Therefore, tuning of the individual portions is possible by properly choosing the geometry of the barrier. The following calculations were carried out for a thin Al barrier ($w = 110$ nm) at $\lambda = 633$ nm. The width was deliberately chosen well below $\Lambda_{SPP}/2$ in order to prevent a strong impact of the precise value of w, but thicker than the skin depth to prevent tunneling. The transmission is not
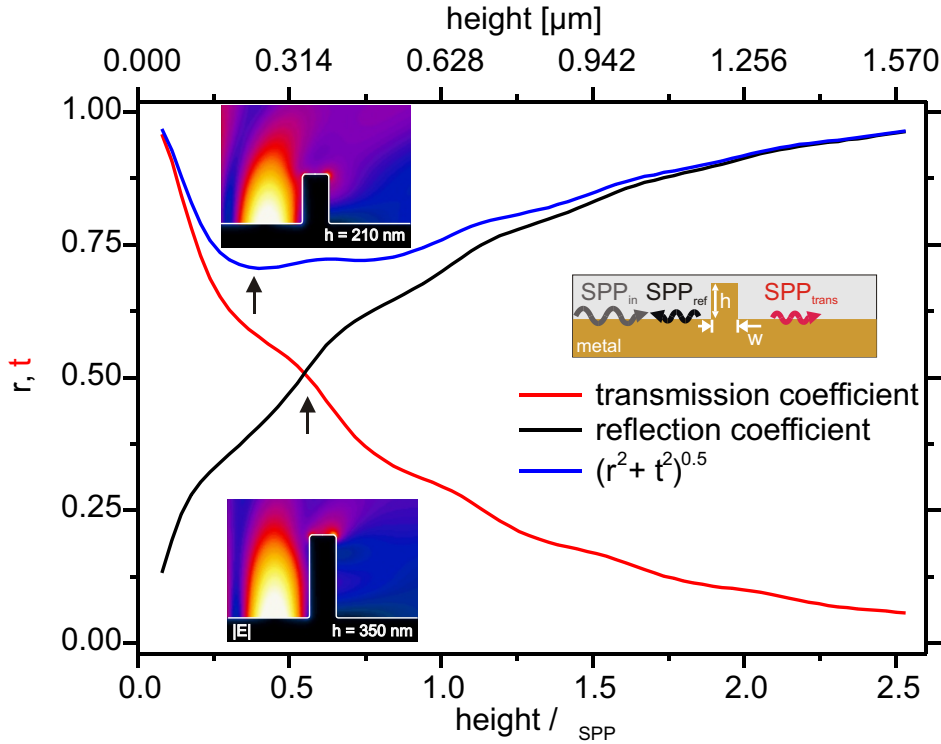
Figure 6.11 *Depending on the height of the barrier ($w = 110$ nm), either the transmission or reflection coefficient dominates. The radiated power is only significant in the intermediate region between heights of $0.1 \cdot \Lambda_{SPP}$ and $2 \cdot \Lambda_{SPP}$ as indicated by the difference between the blue curve and unity. The two insets show the mean electric field on a linear color scale. The bright colors correspond to high intensities, as found at the edges having small radii ($\rho = 15$ nm) of curvature as well as in the maxima of the standing wave.*

only characterized by an exponential dependence on the barrier height ($\approx e^{-1.5k_{z,vac}h}$), but also a slight oscillation known from the previously studied case of the upward step (see Fig. 6.10). Analogously, the incident SPP excites a plasmon at the top of the barrier which

is scattered into the forward direction and forms SPP_{trans} by exciting the surface charges behind the barrier. The quantitative value of SPP_{trans} is identical to the product $t_{up} \cdot t_{down}$ for $h < 1.5 \cdot \Lambda_{SPP}$. Similarly, the value of the reflected SPP is mainly given by r_{up} for the upward step studied in Sec. 6.3.1. Therefore, more complex geometries might be described to a very good approximation by the transmission characteristics of the individual features presented before. Such an analysis is naturally restricted to situations in which the transmitted field has only a minor influence on the field on the incident side.

6.3.3 Groove interaction

Let us now focus on a system in which the barrier is replaced by a groove. A SPP is much less reflected by a downward step than by an upward step as pointed out before in section 6.3.1. Therefore, the transmission is expected to be higher in the case of a groove instead of a barrier, which can be advantageous in plasmonic devices. The question remaining is: How sensitive is the amplitude of SPP_{trans} to the geometry of the groove? Is it possible to construct wavelength-sensitive components by such geometries, such as filters or dichroic SPP mirrors?

The problem of grooves in metals has been in the focus of former research. For example, Maradudin *et al.* studied theoretically a dielectric gap of varying width w between two surface-active media. A Fabry-Perot-like behavior or poles were found depending on whether this gap was filled by a dielectric having $\varepsilon = 4$ or vacuum. Later, Sánchez-Gil and Maradudin [159] reported that SPP propagation across a single Gaussian-shaped indentation results in a more Fabry-Perot-like behavior. Therefore, it is advisable to shed some light (or better a SPP) on a rectangular-shaped groove in order to illuminate the underlying mechanisms. For the sake of clarity, the two geometrical parameters, namely the width and the depth of the groove, are investigated separately first.

Dependence on the width of the groove

A shallow groove placed in the path of a SPP leads to a modulation of the transmitted (same propagation direction) and the reflected (reverse propagation) portions depending on the width of the groove as plotted in Fig. 6.12. The $|E|$ plot c) in the same figure, reveals the process happening: Most of the SPP propagates across the first edge ($t^2 = 0.978$, $r^2 = 0.0025$ for a downward step having $h = -50$ nm), travels at the bottom of the shallow groove and is mostly transmitted when hitting the second, upward step ($t^2 = 0.944$, $r^2 = 0.0056$ for a upward step having $h = 50$ nm). The superposition of the backward-propagating wave and the one reflected at the left edge results in the cavity-like behavior of t and r as displayed. The oscillation period is equal to $\Lambda_{SPP}/2$. The additional offset originates from the phase shift caused by the reflection.
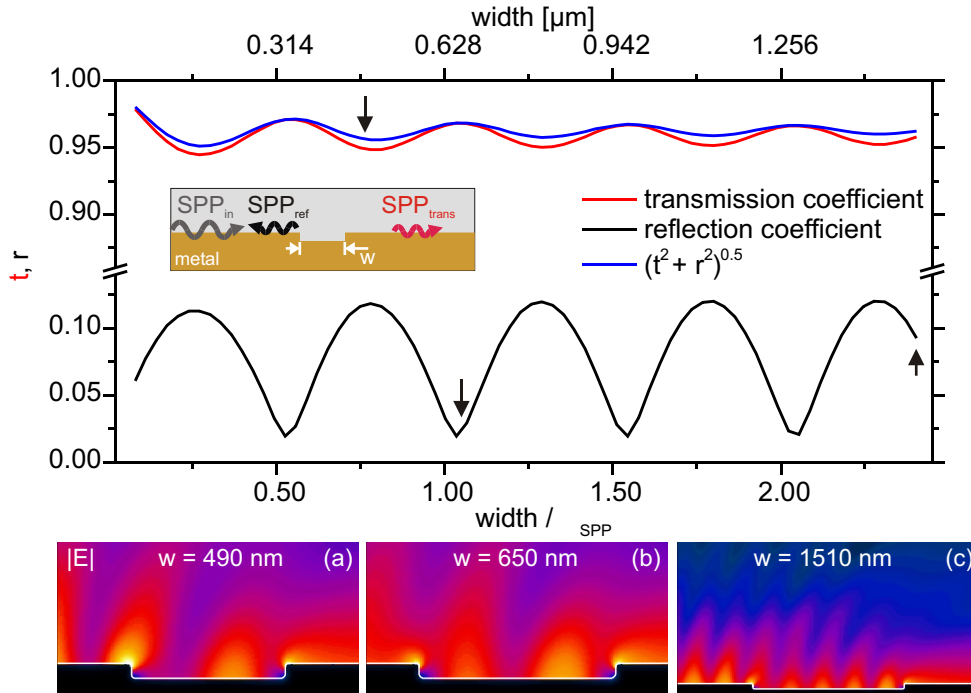
Figure 6.12   *The SPP transmission across a groove having a constant depth $d = 50$ nm shows an oscillation as a function of the width of the groove. The modulation period is equal to $\Lambda_{\mathrm{SPP}}/2$ and is caused by a cavity mode at the bottom of the groove. The reflection has minima at transmission maxima. A certain part of the incident SPP energy is scattered into the vacuum as indicated by the difference between the blue curve and unity. The arrows indicate the groove widths to which the near-field $|E|$ pictures displayed in the lower part of the figure apply.*

Dependence on the depth of the groove

There is also a modulation of the transmitted (same propagation direction) and the reflected (reverse propagation) portions as a function of the depth of the groove. At certain depths, resonances (cavity modes) along the narrow groove can be found similar to the previously studied case (see Fig. 6.12). In contrast to that case, the resonances inside the groove lead to reduced transmission and high reflection. The maxima are shifted because of the strongly varying propagation constant of the modes in the confined vertical cavity as shown in Fig. 6.4 and no longer located at multiples of $\Lambda_{\mathrm{SPP}}/2$ [160]. For example, the propagation constant for the TM_0 mode between two aluminum plates separated by a 30-nm-wide vacuum gap is $k_{\mathrm{gap},0}(w = 30 \text{ nm})/k_0 = 1.369 + 0.006024i$, while all higher modes are much more damped (see Fig. 6.4). That value was used to rescale the bottom abscissa. Now the transmission maxima can be found at multiples of $\Lambda_{\mathrm{gap},0}(w = 30 \text{ nm})/2$ as expected. At these depths, the standing-wave cavity mode is not excited efficiently as shown in the $|E|$ pattern for $d = 460$ nm
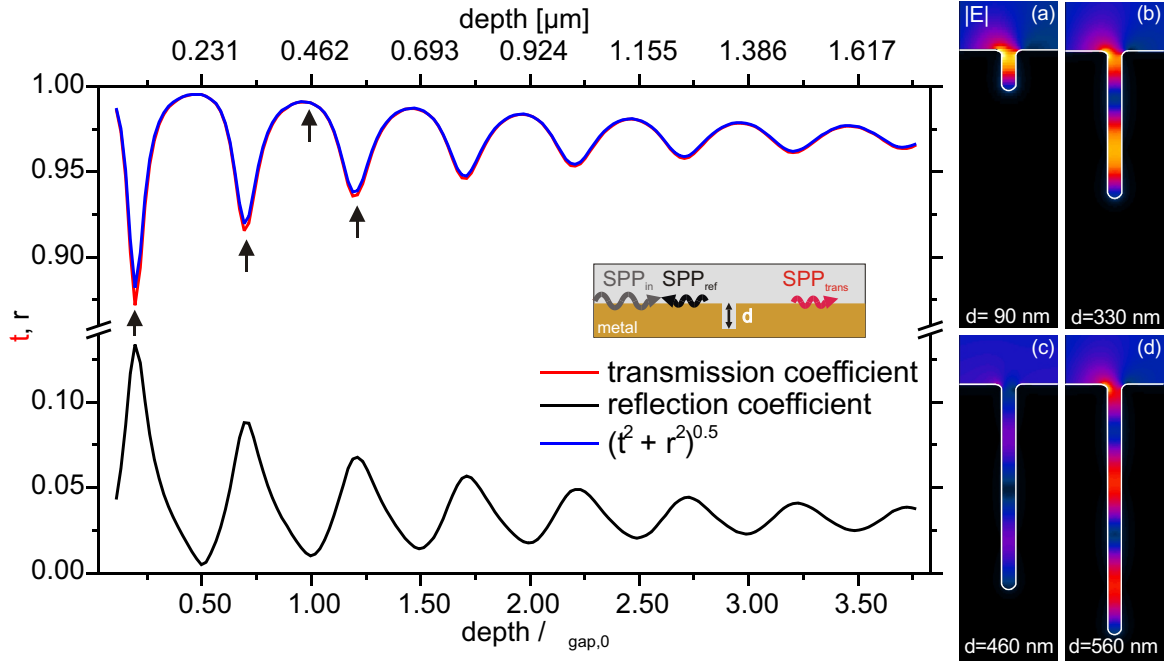
Figure 6.13 *The SPP transmission across a groove having a constant width $w = 30$ nm shows an oscillating dependence on the depth of the groove. The units at the bottom abscissa have been normalized to the propagation constant in a 30-nm cavity between two Al plates, $\Lambda_{\text{gap},0}(w = 30\ nm) = \lambda/1.37$. The modulation period corresponds to $\Lambda_{\text{gap},0}(w = 30\ nm)/2$ and is caused by the excitation of cavity modes inside the groove. A certain part of the incident SPP energy is scattered into the vacuum as indicated by the difference between the blue curve and unity. The arrows indicate the depths to which the $|E|$ pattern displayed on the right side of the graph apply.*

in Fig. 6.13 (c). Between the transmission maxima, the cavity mode is excited much more strongly. Hence, the reflection exhibits maxima, whereas the transmission has minima.

The blue curve in Fig. 6.13 represents the square root of the sum of the energies carried by the transmitted and reflected SPPs. Therefore, the missing part to unity is either scattered into the vacuum or absorbed inside the cavity. The fact that the first transmission dip around $d = 90$ nm is much stronger than the later ones, and the steady decrease of both the mean transmission as well as the depth of the dips leads to the conclusion that absorption is more important for deep structures, as the energy scattered into the vacuum should only be proportional to the square of the local fields at the edges of the groove.

Dependence on the depth and width of the groove

In general, for grooves having varying depth and width, the situation gets more and more complicated – but can be comprehended as a superposition of the cases discussed above. Fig. 6.14 displays the transmission coefficient as a function of d and w. For the sake of easy comparability, the two graphs at the bottom and on the left represent $\text{SPP}_{\text{trans}}$ as studied above for a fixed depth $d = 50$ nm and varying w, displayed before in Fig. 6.12, as well as for a constant width $w = 30$ nm and varying d, shown in Fig. 6.13.

For $w < \Lambda_{\text{SPP}}/2$ the transmission properties are dominated by the fundamental mode, similar to SPP excitation at a single slit (see Fig. 6.3). The reduction of the width of the groove causes an increase of the real and imaginary parts of $k_{\text{gap},0}$ (TM$_0$). Therefore, the minima in t appear less spaced. Just above $\lambda/2$, a formerly strongly damped evanescent mode can now be excited, resulting in a sharp minimum. Similarly, another additional mode can be excited for $w > 0.5 \cdot \lambda_{SPP}$ and $d > 0.8 \cdot \lambda_{SPP}$. In contrast to the excitation of SPPs at slits discussed in Sec. 6.2.1, the higher-order modes start to contribute at $w > \lambda/2$ (rather than $w > \lambda$ as in Fig. 6.3). The modes contributing for $\lambda/2 < w < \lambda$ are prohibited by symmetry for a slit illuminated by a plane wave at 90°. The symmetry is now broken when the groove is illuminated with a SPP from only one side, and therefore the excitation of modes having other symmetries is no longer prohibited.

In conclusion, nanoscale rectangular indentations can be used to control the SPP propagation by adjusting the geometry of the groove. But the accuracy that one must achieve when producing these geometrical features needs to be $\ll \Lambda_{gap}/2$, especially if one operates close to multiples of $\Lambda_{gap}/2$. The two parameters w and d can be used to control the cavity-like behavior, resulting in a Fabry-Perot-like transmission characteristic rather than in poles as presented in Ref. [161]. A further improvement of the filter characteristic may be achieved by using multiple structures instead of only a single one as pointed out by Pincemin and Greffet [162] who studied the propagation and localization of SPPs across a finite grating.
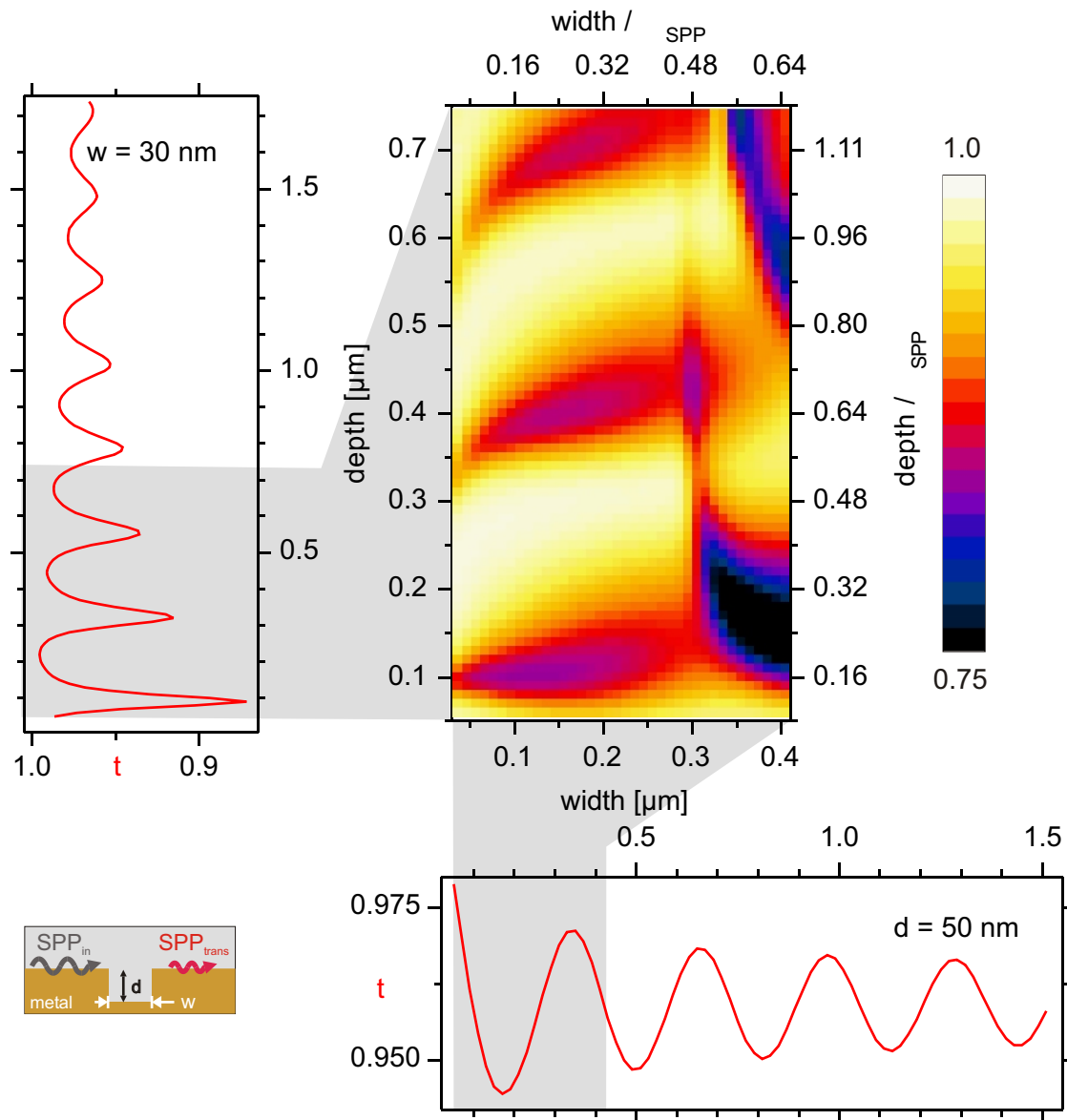
Figure 6.14 *The transmission coefficient across a small groove depends strongly on the width as well as on the depth. The color-coded 2D plot displays the amplitude of SPP_{trans} on a linear scale. The two graphs (top left and bottom right) represent the formerly studied cases in which only one parameter was varied. For $w < \lambda/2$, only the fundamental TM_0 mode inside the groove contributes to the response. At larger w, higher-order modes (of the groove) can also be excited. All of them become evanescent near $\lambda/2$ where the real part of their propagation constant vanishes and the imaginary part increases strongly.*

6.4   Summary: excitation and guiding of SPP at metal surfaces

Breaking the translational symmetry by nanoscale structures at an otherwise planar interface allows SPPs to be launched locally by plane or focused waves. The SPP excitation efficiency σ is strongly related to the excitation of modes inside the indentation and can be tuned by optimizing the width w and the depth d of a rectangular groove. In general, for narrow grooves, a large cross section σ can be achieved with w slightly below $\Lambda_{\mathrm{gap},0}/2$ (and odd multiples thereof) and for $d = (\frac{1}{2} + m)\frac{\Lambda_{\mathrm{gap},0}}{2}$ with $m = [0, 1, \ldots]$. The value of $\Lambda_{\mathrm{gap},0}$ significantly decreases for $w \ll \lambda$. Higher-order modes may also contribute in the case of wider grooves. Similarly, a SPP propagating across a groove will excite the same modes but also additional modes having different symmetry.

The propagation of SPPs at structured surfaces is strongly influenced by the energy distribution normal to the interface, which is determined by $\varepsilon_{\mathrm{metal}}(\lambda)$. Only if most of the energy resides inside the metal, it can be guided with low losses at a curved surface. Otherwise the weakly guided surface wave will be converted into propagating waves which are no longer interface bound (scattered).

Metallic protrusions extending into the dielectric cause reflection of the SPP, whereas indentations into the metal lead to less reflection. All effects reported can be used to construct plasmonic components, such as beam splitters, local in- and out-couplers, wavelength-selective filters etc., and to modify the local density of surface states at the interface [129]. One may suppress the SPP excitation and propagation by creating a photonic (plasmonic) bandgap.

The above-presented analysis of the excitation, propagation, and scattering of SPPs propagating at the interface between a metal and a vacuum half-space highlights the basic physical mechanisms – but most experiments and applications use thin metallic films. The modifications as well as additional effects arising in that case will be discussed in the following.

Chapter 7

Surface plasmon polaritons on thin-film metal waveguides

This chapter is devoted to the optics of SPP waveguide modes on asymmetrically embedded metallic slabs. Particular attention is directed to the excitation and interaction of these modes at / with interruptions of the waveguide and the differences to the previously studied case of a semi-infinite metallic half-space. The slabs provide confinement only normal to the interfaces, but if their width is small, they also allow a two-dimensional confinement of the light. This superb property will be illustrated by means of SNOM experiments.

Thin metallic films, sometimes called metal slab waveguides, consist of two metal-dielectric interfaces in contrast to the formerly studied case of a semi-infinite metal half-space. The waveguide modes are commonly characterized by their complex propagation constants γ_i, similar to the value $k_\parallel$ used previously to describe the propagation of surface waves. The values of γ_i depend on the frequency, the slab thickness h, and the dielectric constants of both the metal and the adjacent media. In the case of thick films, or more precisely for h being much larger than the field penetration/skin depth in the metal, $\delta_{\text{skin}} = \frac{\lambda}{4\pi\text{Im}[n]}$ [163, p. 128], the value of γ_i is nearly identical to $k_\parallel$ given by Eq. (6.1). But, for decreasing h the field of the modes at the individual interfaces penetrates through the metal, modifying the field at the opposite boundary. The resulting waveguide modes can be either interface-bound or leaky [164] (radiating into one dielectric) depending on whether γ_i is larger than the nk_0 or not, where n is the refractive index of the dielectric and k_0 is the wavevector in vacuum. For instance, a metal film supported by the glass prism in the Kretschmann-Raether configuration as displayed in Fig. 6.1 (a) has a purely interface-bound mode with $\text{Re}[\gamma_i]$ lying to the right of the light line in glass $\omega = ck/n$, drawn in green in Fig. 6.1 (b). Complementary, the leaky mode has γ_i between the light line in vacuum $\omega = ck$ and the light line in glass.

The presence of the two interfaces close to each other has much more pronounced conse-

quences in the case of ultra-thin metal films, leading to a drastic change of γ_i and the field patterns of the modes. In the case of a symmetrically embedded slab with the same dielectric at both metal interfaces, the modes are degenerate for "large" h and split into a symmetric and antisymmetric mode in respect to their transverse field components [165] for decreasing h. The symmetric mode guides significantly more energy in the dielectric than in the metal, hence the propagation length δ_{SPP} is increased as predicted by Fukui [166] in 1979 and Sarid *et al.* [167] in 1981 for this so-called *long-range SPP*, which was first observed in 1984 by Dohi *et al.* [168]. They reported a "macroscopic" propagation length $\delta_{\text{SPP}} \sim 200 \ \mu$m at $\lambda = 633$ nm for a nearly symmetrically embedded silver film with $h = 15.6$ nm. The situation is quite different in the case of an asymmetrically embedded metal slab as pointed out by Berini [169] in that, below a certain cutoff thickness of the film, the long-ranging mode does no longer propagates with low losses [169].

The excitation of such waveguide modes is commonly done by using the field overlap of the light incident onto the end-face of the waveguide and the waveguide mode [131, 147] (end-fire coupling), by adjusting the momentum of the incident field via gratings, or by attenuated-total-reflection arrangements such as the ones proposed by Kretschmann and Raether [138] and Otto [137]. The Kretschmann-Raether configuration is restricted to the excitation of leaky waves, whereas the Otto configuration also allows the excitation of fully bound modes[1].

After this short introduction, let us move our attention away from the long-range SPP case and focus on 60-nm-thick silver films illuminated at $\lambda = 633$ nm ($\varepsilon_{\text{Ag}} = -17.9 + 0.7i$) and supported by glass having a refractive index $n = 1.515$. Such asymmetrically embedded metallic slab waveguides have been used widely in experiments [146, 170, 171], and therefore it is interesting to compare the MMP results with experiments reported in literature to deepen our insight into the processes happening in the nanoworld of SPPs.

As already mentioned, the propagation constants γ_i for metallic thin-film waveguides with layer thickness well above the regime of long-range SPPs is approx. given by Eq. (6.1) for a vacuum/metal and glass/metal interface, respectively. The numerical solutions γ_i of the corresponding eigenvalue problem were used in order to describe the SPP waveguide modes within the models more accurately:

mode	$k_{\parallel,i}/k_0$ (analytical)	γ_i/k_0 (numerical)
$\text{SPP}_{\text{vac/metal}}$	$1.0291121 + i0.001188742$	$1.0294144 + i0.0017484$
$\text{SPP}_{\text{glass/metal}}$	$1.6223937 + i0.004657730$	$1.6252530 + i0.0050651$

Table 7.1 *Propagation constants γ_i of the SPP modes of a 60-nm-thin silver film on glass.*

---

[1]More precisely, the previously fully bound mode having most of its energy concentrated at the inner glass metal interface can be excited, but the presence of the coupling prism in the Otto configuration causes the mode to become leaky.

The electromagnetic field of these waveguide modes penetrates partially trough the metal into the opposite dielectric space. In the particular problem under investigation, the presence of the additional boundary leads to slightly larger values of $\mathrm{Re}[\gamma_i/k_0]$ compared to $\mathrm{Re}[k_{\parallel,i}/k_0]$. The $\mathrm{SPP_{glass/metal}}$ waveguide mode has most of its energy located at the inner glass/metal interface and is characterized by $\mathrm{Re}[\gamma_i] > nk_0$. Therefore, this mode is purely interface-bound. The energy of the $\mathrm{SPP_{vac/metal}}$ mode is mostly concentrated at the outer vacuum/metal interface. However, the value of $\mathrm{Re}[\gamma_i]$ of this mode lies between the light lines in vacuum and glass ($k_0 < \mathrm{Re}[\gamma_i] < nk_0$). Hence, the portion of the field that penetrates through the film is no longer interface-bound and radiates into the glass half-space. The energy loss due to this leakage radiation contributes to the damping and consequently increases $\mathrm{Im}[\gamma_i]$ by nearly 50 % for this mode. This damping by leakage radiation often suppresses the occurrence of long-ranging waveguide modes in asymmetrically embedded thin metal films.

The two mentioned waveguide modes do not couple to each other when they propagate at an infinitely extended film because of the mismatch in momentum. A coupling may take place at points where the translational invariance is violated, such as the end face or an interrution of a waveguide, which will be discussed later. Before, let us take a closer look at the possibility of exciting the two modes.

7.1 Excitation of SPPs at a single slit

As already mentioned, only the leaky $\mathrm{SPP_{vac/metal}}$ mode having the energy concentrated at the outer vacuum/metal interface may be excited using the Kretschmann-Raether configuration, whereas the larger propagation constant γ_i of the $\mathrm{SPP_{glass/metal}}$ mode is only accessible in the Otto arrangement where an evanescent wave at a prism surface is placed in close proximity to the metal interface. Both methods are restricted to large excitation areas having diameters larger than ten micrometers if classical optical components such as prisms are used, because only slightly focused beams can be applied. Alternatively, a partially illuminated high-NA objective might be used instead of the prism in a Kretschmann-Raether-like arrangement [172], featuring a much more local launching of the $\mathrm{SPP_{vac/metal}}$ mode with a lateral extension down to 1 μm.

A waveguide discontinuity such as a slit cancels the translational symmetry and should allow the direct excitation of the waveguide modes in a similar way as in the previously studied case of excitation of SPPs by plane waves at grooves in metals, analyzed in Sec. 6.2.1. In the case of a groove, the mode excitation cross section σ crucially depends on both geometrical parameters, namely the depth d and width w. Especially the dependence on d requires an accuracy $\ll \Lambda_i$ in the manufacturing, which may be difficult to achieve. On the other hand, the thickness of the metal film can be accurately controlled during the deposition process, leading to a much easier fabrication of the slit arrangement compared to grooves. The dependence of σ on the remaining parameter w is analyzed for a setup as sketched in Fig. 7.1. The 60-nm-

thin silver waveguide is illuminated by a p-polarized plane wave incident at 90° (measured relative to the metal surface) from the vacuum half-space or from the glass half-space using a (free-space) wavelength $\lambda_0 = 633$ nm. The value of σ for both illumination directions, dis-
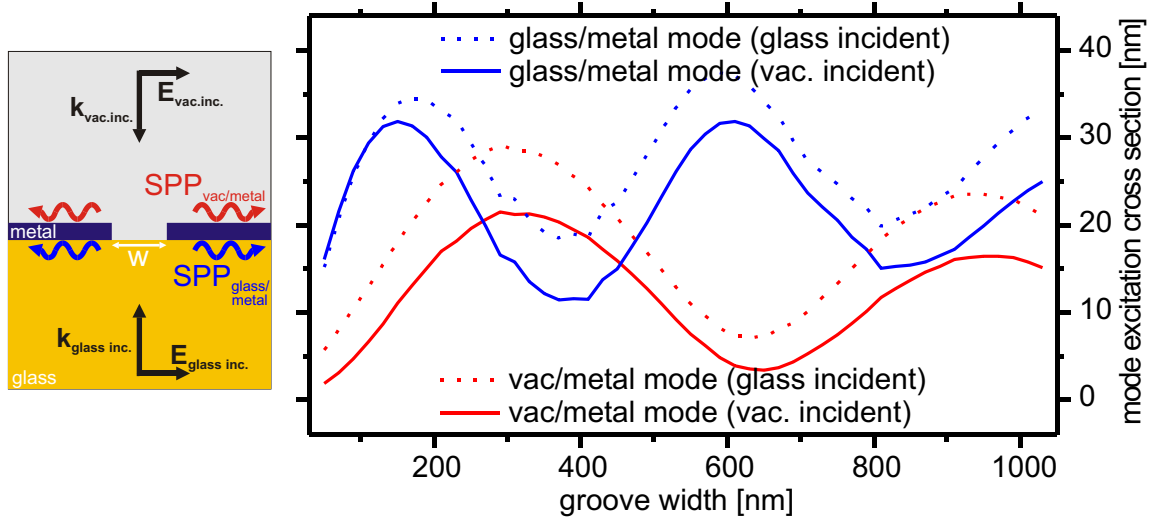

Figure 7.1   *A groove inside a 60-nm-tick Ag film on glass allows SPP excitation by direct illumination with p-polarized light. The excitation cross sections for the two waveguide modes are oscillating functions of the groove width, which allows the preferential excitation of one specific waveguide mode.*

played in Fig. 7.1, shows an oscillatory dependence on w. The different oscillation periods of the two modes corresponds to the wavelengths $\Lambda_{\text{glass/metal}} \approx 389$ nm and $\Lambda_{\text{vac/metal}} \approx 615$ nm of the modes. The position of the minima and maxima in σ_i at multiples of $\Lambda_{\text{glass/metal}}$ and $\Lambda_{\text{vac/metal}}$ or at odd multiples of half of it, respectively, can be explained in analogy to the groove case. The minima are formed by a destructive interference originating from the two fields at the edges being 180° out of phase and the additional phase shift acquired during the propagation across the slit.

The values of σ in the case when the plane wave is incident from the vacuum may be compared to the results reported in Sec. 6.2.1. The value σ_i for the $\text{SPP}_{\text{vac/metal}}$ mode peaks at $w \approx 290$ nm, reaching $\sigma_{\text{vac/metal}} = 21.5$ nm (for each of the two propagation directions $\pm k_{\parallel}$). This value is smaller by a factor of $\approx \frac{1}{3}$ compared to the maximum found for a narrow and shallow groove in a metal half-space (see p. 69).

This is caused by two effects:

Firstly, part of the incident light excites the additional $\text{SPP}_{\text{glass/metal}}$ mode ($\sigma_{\text{glass/metal}} = 17$ nm).

Secondly, the slit has no metallic bottom like the groove. Therefore, the mode propagating in the slit will only be weakly backreflected, leading to less enhanced fields at the edges.

Hence, the SPP is less excited. The impact of the latter point becomes more obvious from an inspection of the total cross section (or energy) summed over all SPP waveguide modes. The maximum of this quantity is roughly $\Sigma\sigma_i = 45$ nm in the case of a slit in a thin film compared to 65 nm for the groove having a metallic bottom.

Comparing the curves for the two different directions of the incident wave, we find a significantly higher σ_i in the case that the plane wave is incident from the glass half-space. Nevertheless, the overall dependence is nearly the same in both cases.

The edges of the slit were rounded for the sake of easier modelling to $\rho = 15$ nm at the vacuum/metal interface and to $\rho = 5$ nm at the glass/metal interface close to the triple points where the three media meet. One may wonder what influence this assumption has. A recomputation of the same problem with both radii of curvature are set to 5 nm does not alter the results reported above. Hence, it is not important to achieve really (atomically) sharp edges which simplifies the fabrication (FIB patterning) drastically.

In conclusion, the excitation process reported in this section can be understood as follows: The incident plane wave excites the SPP mode at the first interface as well as the modes in the slit (similar to the case of a groove in Sec. 6.2.1). The modes in the slit transport the light to the opposite metal film interface[2], leading to an excitation of the surface modes at this interface. The magnitude of the energies coupled to the two individual waveguide modes can be adjusted via the width of the slit. Therefore, it is possible to launch locally even the mode at the inner glass/metal interface.

Similar effects have been studied by other groups in the context of enhanced transmission of light through apertures [174] or slits [175, 176] as well as arrays of them. In that case, structuring the area close by the aperture or slit alters the density of surface modes. This can lead to strongly enhanced transmission if the metal/dielectric interface on the excitation side is structured [177] and/or to a beaming (directional transmission) in the case that the exit face is structured [143, and Ref. therein].

7.2 Interaction of SPP waveguide modes with surface irregularities

Let us focus on more application-related aspects, such as the construction of plasmonic devices or sensors based on thin-film SPP waveguide modes. For that, the following investigation is intended to illustrate the underlying physics for two simple but basic structures, namely the end face of a metallic thin-film waveguide and a groove interrupting the waveguide.

---

[2]This process is sometimes called light tunneling [173].

7.2.1 Thin-film end face

The first and most basic problem is the behavior at the end face of a thin-film silver waveguide supported by glass as displayed in Fig. 7.2. For convenience, the same parameters as in the preceding section for the 60-nm-thin silver film ($\varepsilon_{\text{Ag}}(\lambda = 633 \text{ nm}) = -17.9 + 0.7i$) are assumed. Hence, this asymmetrically embedded metal slab waveguide has the same two eigensolutions. Each of them was used as the excitation in separate computations.

The abrupt end of the silver thin film causes reflection and radiation into both dielectric half-spaces similar to the SPP interaction at an edge studied in Sec. 6.3.1. The additional glass/metal interface in the case of a thin-film waveguide, and therefore the existence of the second mode, allows a conversion of the incident mode into this second mode at the end face, because the translational invariance is broken locally at the waveguide end. The
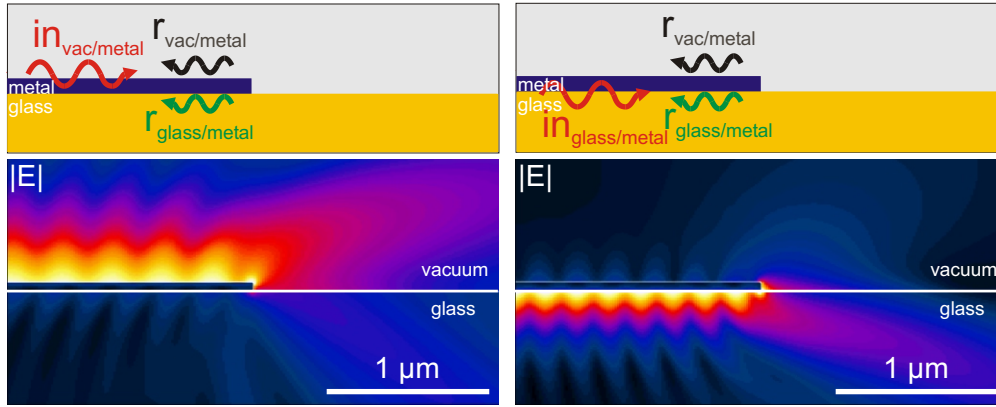

Figure 7.2 *The SPP approaches the end face from the left of a 60-nm Ag thin-film waveguide on glass. The energy of the incident SPP is either located mainly at the upper vacuum/metal interface (left), or at the inner glass/metal interface (right). Beside strong scattering, small amounts are reflected or coupled into the complementary SPP mode. The reflected portions interfere with the incident SPP, forming a pronounced standing-wave pattern on both sides of the metal film.*

$|E|$ patterns displayed in Fig. 7.2 for the two different incident waveguide modes reveal the different (re-)distribution of the light. The relative amounts of energy of these two backward-propagating modes are listed in Tab. 7.2.1.

The superposition of the incident and both counter-propagating modes forms a stationary intensity pattern having modulation periods Λ_i given by the differences of the propagation constants γ_i. The interference of the incident wave and the field reflected into the same waveguide mode forms a pattern with:

$$\Lambda_1 = \frac{2\pi}{|2\gamma_{\text{vac/metal}}|} = 307.5 \text{ nm}, \tag{7.1}$$

incident mode	Reflection	coupled into other mode
$in_{\text{vac/metal}}$	$r^2_{\text{vac/metal}} = 0.6\%$	$r^2_{\text{glass/metal}} = 1.3\%$
$in_{\text{glass/metal}}$	$r^2_{\text{glass/metal}} = 3.3\%$	$r^2_{\text{vac/metal}} = 1.3\%$

Table 7.2 *Reflectivity and mode conversion at the end face of a 60-nm-thin Ag waveguide on glass.*

in the case that $\text{SPP}_{\text{vac/metal}}$ is used as the excitation. Conversely, if $\text{SPP}_{\text{glass/metal}}$ is chosen as the incident wave, we obtain:

$$\Lambda_2 = \frac{2\pi}{|2\gamma_{\text{glass/metal}}|} = 195 \text{ nm}. \tag{7.2}$$

Additionally, a small amount of the SPP is transferred to the complementary waveguide mode. The resulting interference pattern has a period of:

$$\Lambda_3 = \frac{2\pi}{|\gamma_{\text{vac/metal}} + \gamma_{\text{glass/metal}}|} = 238 \text{ nm} \tag{7.3}$$

in both cases. The visibility of this beating is much lower because only a small part of the field of the modes penetrates through the metal. Finally, the remaining beating pattern of both reflected portions gives rise to a much larger modulation period:

$$\Lambda_4 = \frac{2\pi}{|\gamma_{\text{vac/metal}} - \gamma_{\text{glass/metal}}|} = 1062 \text{ nm}. \tag{7.4}$$

The small reflection coefficients in Tab. 7.2.1 imply that the visibility of Λ_4 is much weaker, even compared to Λ_3. This analysis, describing the stationary intensity pattern, is valid only far away from the end face. Close to the end face, the requirement of the continuity of the field within the domains results in a bending/distortion of the pattern in the dielectrics away from the metal as shown in Fig. 7.2. Therefore, a measurement that collects the intensity some ten or hundred nanometers above the surface would indicate larger intensity modulation periods close to the edge.

The $|E|$ patterns in Fig. 7.2 also reveal a different angular distribution of the scattered light depending on which SPP waveguide mode is used as excitation. For the mode having the energy mostly concentrated at the vacuum/metal interface (see Fig. 7.2 left), the majority of the light is scattered into the forward direction at angles close to 30° (measured with respect to the interface) in the vacuum half-space. Additionally, a significant amount of energy is radiated into the glass half-space at angles slightly smaller than 30°. Conversely, the radiation into the glass half-space clearly predominates in the case when the $\text{SPP}_{\text{glass/metal}}$ mode is incident, as illustrated in Fig. 7.2 (right).

At this point, let us compare the reflectivities calculated for the end face of the thin-film metal waveguide and at a metallic edge ($r^2 < 0.2$ % see Sec. 6.3.1) with other calculated

values and experimental observations reported in literature: In 1983, Wallis *et al.* [149] investigated the influence of a dielectric barrier behind the end-face of the metal ($\varepsilon_{\mathrm{metal}} = -15$). In the case of vacuum they reported a reflectivity of less than 2 % and predominant forward scattering. Later, in 1995, Jamid *et al.* [151] studied a 90° metal edge, assuming $\varepsilon = -16$ and $\lambda = 633$ nm and using the method of lines [151, see Ref. therein]. The reported value of the backward-propagating light of 4.3 % includes both the reflected SPP and the backward-scattered light, and therefore represents an upper limit of r^2 only. In 1997, Schroeter *et al.* [178] investigated the interaction of SPPs with sharp and smoothed edges by means of FDTD, but without giving any numbers for the reflectivity. Baida *et al.* [179] modelled the reflection of the SPP$_{\mathrm{vac/metal}}$ waveguide mode at a 53-nm-thick silver ($\varepsilon = -17.9 + 0.7i$) film at $\lambda = 633$ nm. They pointed out that the reflection at the edge is rather weak and comparable to the experimental noise. Similarly, Salomon *et al.* [180] reported for a metal thin-film waveguide of finite width that as long as the width of a waveguide is larger than the SPP propagation length there is no significant reflection at the end.

The reported theoretically predicted reflectivities are always low. Contrary, the numbers observed in experiments vary much more. In the first reported experiment by Dawson *et al.* [145], the SPP$_{\mathrm{vac/metal}}$ mode on 53- and 58-nm-thick Ag films at $\lambda = 633$ nm was excited using the Kretschmann-Raether configuration. The edge interaction caused a reflection of $r^2 = 2$ %. The repetition of the experiment by the same group five years later, revealed no evidence of a reflected beam [181]. More recent measurements, performed by Steinberger *et al.* at $\lambda = 785$ nm [182], yielded up to 20 % reflection and 20 % conversion, the average values being 7 % for both portions. The actual value was strongly sensitive to the edge quality of the EBL-fabricated 50-nm gold films[3]. Similar high values of reflectivity of up to 25 % have also been reported by Seidel [146, p. 52] in the case of a silver film intersected by a groove. Such an arrangement has been investigated before by Bouhelier *et al.* [170] who reported much lower reflectivity $r^2 = 3 \ldots 6$ %.

The broad range of $r^2 = 0 \ldots 25$ % in the experiments in contrast to the rather low theoretically predicted values is surprising. The differences might originate from different geometries, an unintentional collection of backward-propagating scattered light by the uncoated SNOM probe, or an impact of the near-field measurement itself on the reflection. Seidel *et al.* and Steinberger *et al.* observed that the reflection varies strongly from groove to groove and edge to edge, respectively. Therefore, it is plausible to assume that the effect originates from the geometry of the end face rather than from the measurement itself. A simple step or ridge located at the edge, would need to be roughly 0.5 Λ_{SPP} in height in order to produce $r^2 = 25$ % as shown in Sec. 6.3.1. No such "huge" features were found in the experiments. However, smaller geometrical features will always alter the radiated portions. Especially backward-scattered

---

[3]An MMP analysis using parameters adapted to this experiment ($\lambda = 785$ nm, $\varepsilon_{Au} = -21.9241 + 1.36367i$) leads to similar low values of $r^2_{\mathrm{vac/metal}} = 0.4$ % and $r^2_{\mathrm{glass/metal}} = 1.4$ % as in the case of a 60-nm-thick Ag film excited at $\lambda = 633$ nm.

light might be collected by the SNOM probe. The interference with the field collected from the SPP produces a similar interference pattern having a period very close to Λ_1. A variation of the shape of the 2D profile of the slab is only one imaginable situation. A similar variation might occur in the third orthogonal direction (along the surface, perpendicular to the propagation direction). The SPP extends into this direction. The continuity of the fields inside the domains (no surface charge) implies that a different local geometry along the third direction will be sensed by the whole wave and might change the reflectivity. The strong dependence of the reflectivity on $\mathrm{Re}[\varepsilon_{\mathrm{metal}}]$ shown in Fig. 6.8 might point to the following explanation: $\varepsilon_{\mathrm{metal}}$ at the fuzzy end face, which is frayed on a sub-wavelength scale, has to be characterized by an effective medium with ε different from the bulk value. Depending on the actual corrugation, this value might be less negative than $\varepsilon_{\mathrm{Ag}}$. Hence, the reflectivity would be larger than shown in Fig. 6.8. The verification of this hypothesis would require a 3D calculation of the problem.

Bouhelier *et al.* [170] and Seidel *et al.* [146] did their experiments using slits in metal films rather than studying the properties at the end face. This different configuration will be analyzed in the following section.

7.2.2   Groove interaction

The model system under consideration now consists of a 60-nm-thick silver film at $\lambda = 633$ nm, structured by a slit/groove of width w on glass as displayed at the top of Fig. 7.3. The SPP waveguide mode $in_{\mathrm{vac/metal}}$ incident from the left hits the groove on its way. This discontinuity causes a scattering into both dielectric half-spaces, and reflection and transmission into the modes $r_{\mathrm{vac/metal}}$ and $t_{\mathrm{vac/metal}}$ because of the broken translational invariance. Additionally, the excitation of the SPP waveguide modes $r_{\mathrm{glass/metal}}$ and $t_{\mathrm{glass/metal}}$ having their power mostly concentrated at the inner silver/glass interface becomes possible. The $|E|$ field patterns in Fig. 7.3 reveal the different interference/beating patterns resulting from the superposition of the modes. On the left-hand side, the patterns are similar to the ones studied previously in the case that $in_{\mathrm{vac/metal}}$ hits the end face of a thin film (see Fig. 7.2), whereas on the right-hand side of the groove the sole beating pattern arising from the interference of $t_{\mathrm{vac/metal}}$ and $t_{\mathrm{glass/metal}}$ with $\Lambda_4 = 1062$ nm is clearly visible only in the glass. The same stationary intensity modulation is present in the vacuum too, but apparently hidden in the much higher intensity of $t_{\mathrm{vac/metal}}$ when a color scale covering a wide range of $|E|$ is used.

As already mentioned, the power of $in_{\mathrm{vac/metal}}$ is not only redistributed into the waveguide modes at both side of the groove. Additionally, the discontinuity of the film gives rise to scattering into both dielectric half-spaces. This radiated portion increases for wider grooves as indicated by the difference between the cyan curve in Fig. 7.4 and unity. The angular distribution of this radiation also changes depending on w. Especially the backward-scattered light strongly depends on the width of the groove. For instance, for $w = 750$ nm the $|E|$ pat-
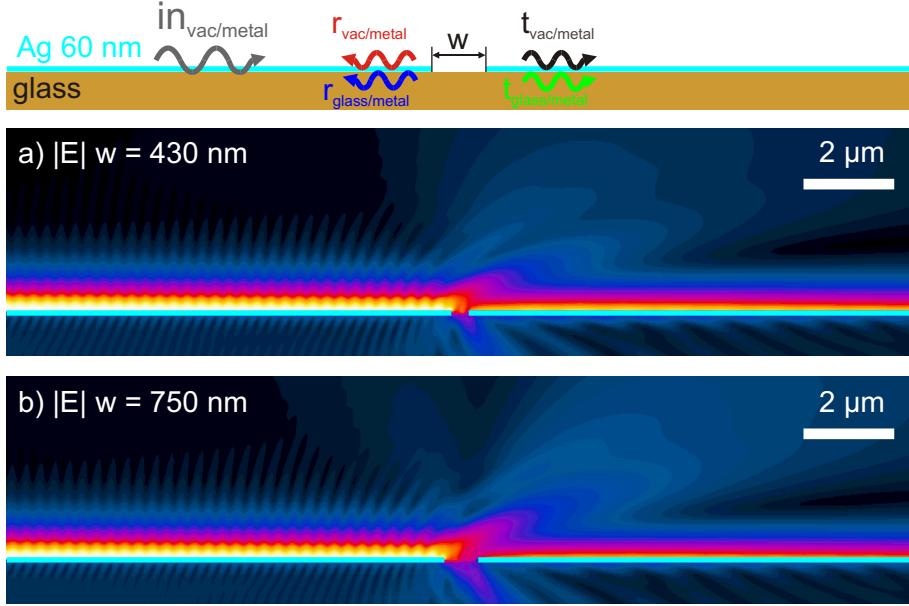
Figure 7.3   *The incident SPP waveguide mode $in_{vac/metal}$ is transmitted across the groove into the same mode $t_{vac/metal}$ and into the second mode $t_{glass/metal}$. These two modes form a beating pattern with $\Lambda_4 \approx 1~\mu m$ clearly visible inside the glass. Additionally, the interference of $in_{vac/metal}$ with the back-propagating modes $r_{vac/metal}$ and $r_{glass/metal}$ creates standing intensity patterns having $\Lambda_1 = 307.5~nm$ and $\Lambda_3 = 240~nm$. The amount and angular distribution of the energy scattered into both dielectrics strongly depends on the width w as displayed in a) and b).*

tern displayed in Fig. 7.3 b) shows pronounced backward scattering into the vacuum, whereas for $w = 430$ nm the backward scattering is significantly smaller, as shown in Fig. 7.3 a). In contrast to the strong dependence of the back-scattered light on the width w, the direction of the pronounced forward scattering into the vacuum seems to remain nearly unchanged.

 Let us now focus on the quantitative values for the distribution of the incident power between the different modes as a function of the groove width. As displayed in Fig. 7.4, the value of $t_{vac/metal}^2$ decreases continuously for increasing w, and only a tiny modulation may be noticed. The presence of the vacuum-glass interface causes the direction of the dominant forward radiation to go out of the vacuum/metal interface plane as displayed in Figs. 7.2 and 7.3, whereas without the vacuum/glass boundary, this radiation is nearly along the interface of the surface as shown in Fig. 6.6. This scattering off the Ag surface causes the transmission to fall off for wider grooves, and consequently, masks the small oscillation of $t_{vac/glass}$. It can be unmasked by (numerically) removing the scattering loss, which exhibits an almost exponential dependence on w. The resulting damped oscillation is similar to the result obtained for a groove in a metal half-space as displayed in Fig. 6.12.
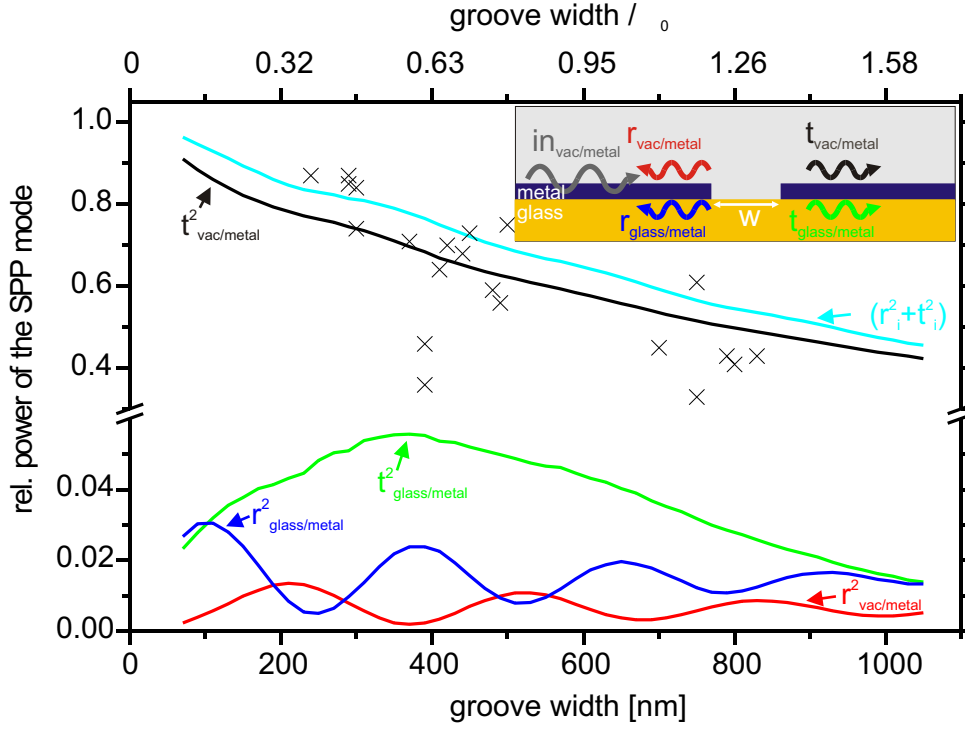
Figure 7.4 *The power coupled to the different modes as a function of the groove width in a 60-nm Ag thin film on glass ($\lambda = 633$ nm). The experimental values of the transmissivity t^2 indicated as crosses ($\times$) are reproduced by courtesy of J. Seidel [146]. For larger w, the radiated power increases as indicated by the difference between the sum of the power of all modes (cyan curve) and unity.*

The power converted into the second waveguide mode on the transmission side, $t^2_{\mathrm{glass/metal}}$, is maximized for $w \approx 370$ nm, which is slightly smaller than $\Lambda_{\mathrm{glass/metal}} \approx 389$ nm. For wider grooves the power decreases – again caused by the strong scattering out of the interface plane.

The incident SPP waveguide mode $in_{\mathrm{vac/metal}}$ will also be partly converted into the back-propagating modes $r_{\mathrm{vac/metal}}$ and $r_{\mathrm{glass/metal}}$. For wide grooves, the reflectivity $r^2_{\mathrm{vac/metal}}$ and the power converted to the second mode, $r^2_{\mathrm{glass/metal}}$, are identical to the values found for an abrupt end of a thin film as investigated before ($r^2_{\mathrm{vac/metal}} = 0.6\%$ and $r^2_{\mathrm{glass/metal}} \approx 1.3\%$, see Sec. 7.2.1). But for widths less than a micron, the values of $r^2_{\mathrm{vac/metal}}$ and $r^2_{\mathrm{glass/metal}}$ are strongly influenced by the interaction of the oscillating surface charges on both sides of the groove, which causes an oscillation around the values obtained for the thin-film end face. The different oscillation periods for the two reflected modes correspond to their wavelengths $\Lambda_{\mathrm{vac/metal}} = 615$ nm and $\Lambda_{\mathrm{glass/metal}} = 389$ nm.

The flexibility of the modelling with respect to the geometrical features assumed provides not only a wide playground, but also allows us to find out which parameters are critical for the experiment and which are not. For instance, the metal edges at the end face in Fig. 7.4 were set to have a radius of curvature of 15 nm at the upper edge and 5 nm at the lower edge (at the glass interface). The recomputation of analogous problems with radii of 30 nm and 5 nm instead of 15 nm at the upper metal surface yields essentially the same transmission behavior. Also, assuming a 100-nm-deep removal of the glass substrate within the groove (which could easily happen during the focused-ion-beam (FIB) sputtering) does not alter the transmission data severely.

The transmission of SPPs across small grooves in thin metal films was studied extensively by Seidel et al. [146, 183, 184] using scanning near-field optical microscopy (SNOM). The observed values of the power propagating across the groove are marked in Fig. 7.4 as crosses ($\times$). The transmitted power measured is in good agreement with the calculated values $t_{\mathrm{vac/metal}}^2$. Only two data points for a width $w \approx 390$ nm differ significantly from the calculated values. That might be attributed to experimental uncertainties. Especially the quality of the groove is difficult to control. The grooves were milled by FIB sputtering. The sputter yield strongly depends on the orientation of the nanocrystals inside the thin silver film. Hence, arbitrarily oriented nanocrystals cause the sputtered edges of the grooves to become rough [146, p. 24], in contrast to what one assumes in the simulation.

A related geometry assuming a surface-wave-active medium intersected by a gap region where no surface modes exist has been theoretically investigated before by Maradudin *et al.* [150, 161]. They assumed a loss free surface-wave-active medium with $\varepsilon = -15$. The structure under investigation in Refs. [150, 161] consists of additional metallized plates besides the metallic SPP waveguide. These plates, which are placed directly underneath the waveguide and at a distance above the metal surface, confine the fields in the direction perpendicular to the interface. If the gap is "filled" with vacuum, the published results show "divergent" transmission values at $w \approx \lambda/2$ and $w \approx \lambda$. No such "divergences" have been found in the MMP calculation. The transmission behavior in Refs. [150, 161] originates most probably from the additional introduced metallized plates.

7.3   Experiments on structured thin films

The investigations presented in the previous chapters were carried out by modelling the plasmonic structures. But, models are only a formal representation of nature, offering the advantage that all variables can be controlled completely. Therefore, one can gain insight into the physical (electromagnetic) mechanisms present on the nanoscale by removing all the uncertainties which are inherent to any experiment. Nevertheless, theory and modelling

have to be validated by experiments in order to demonstrate the technical feasibility of the concepts.

7.3.1 Excitation of SPPs on slits

The local launching of SPPs and waveguide modes at discontinuities has been discussed theoretically in detail in Secs. 6.2.1 and 7.1 and is the subject of the experiments presented in the following.

To prove the principle of local launching, a sub-wavelength slit/groove in a 60-nm-thick film made of aluminum deposited onto a glass cover slip was fabricated at the Forschungszentrum Rossendorf using a focused-ion-beam (FIB) device for milling. This high-resolution FIB sputtering (25 keV Ga$^+$, IMSA-Orsay Physics FIB) features a resolution down to structural sizes of roughly 30 nm, but only if the sputtering yield is uniform across the sample. As already mentioned, this is usually not the case for materials consisting of differently oriented small grains/nanocrystals. For instance, the quality of FIB-milled slits/edges in thermally evaporated thin silver films on glass is rather bad, whereas the much smaller grain sizes in thermally evaporated aluminum thin films allows the fabrication of edges having a much smaller roughness. Also, the optical properties of aluminum are not too bad in the visible spectral range (see Fig. 6.2). Hence, the propagation length δ_{SPP} is still "macroscopic" $\delta_{\mathrm{SPP}}(\varepsilon_{\mathrm{Al}} = -56 + 21i) = 14.8~\mu$m, making aluminum the material of choice for the fabrication.

Groove illumination can be performed either through the glass or from the air. As shown in the modelling in Fig. 7.1, choosing an incident wave coming from the glass side noticeably increases the coupling efficiency. This also provides enough free space above the interface to map the electric field of the plasmon by a SNOM tip. The incident laser light ($\lambda = 633$ nm) was threaded through an inverted microscope (Zeiss Axiovert 135) and focused by an objective ($10\times$, NA $= 0.25$) onto the groove through the glass cover slip as sketched in Fig. 7.5 left panel. In order to geometrically restrict the angle of incidence to values close to normal incidence, the numerical aperture (NA) was deliberately chosen to be small. Therefore, the angle of the impinging light is far away from the angle of total internal reflection, so a Kretschmann-Raether-like excitation, as would be possible with a high-NA oil-immersion objective, can be excluded. The small NA implies a rather large diameter of the focus and the area where SPP is launched. The polarization was carefully adjusted in such a way that the electric field of the incident laser beam was oriented perpendicular to the edges of the groove, because only such an orientation of the incident field fits to the electromagnetic field of a plasmon.

The intensity above the air/metal interface was probed using a SNOM [185, 186] equipped with an uncoated dielectric fiber tip produced by tube etching [187]. The tip was mounted on a tuning fork which could be moved in all three dimensions with nanometer resolution. The
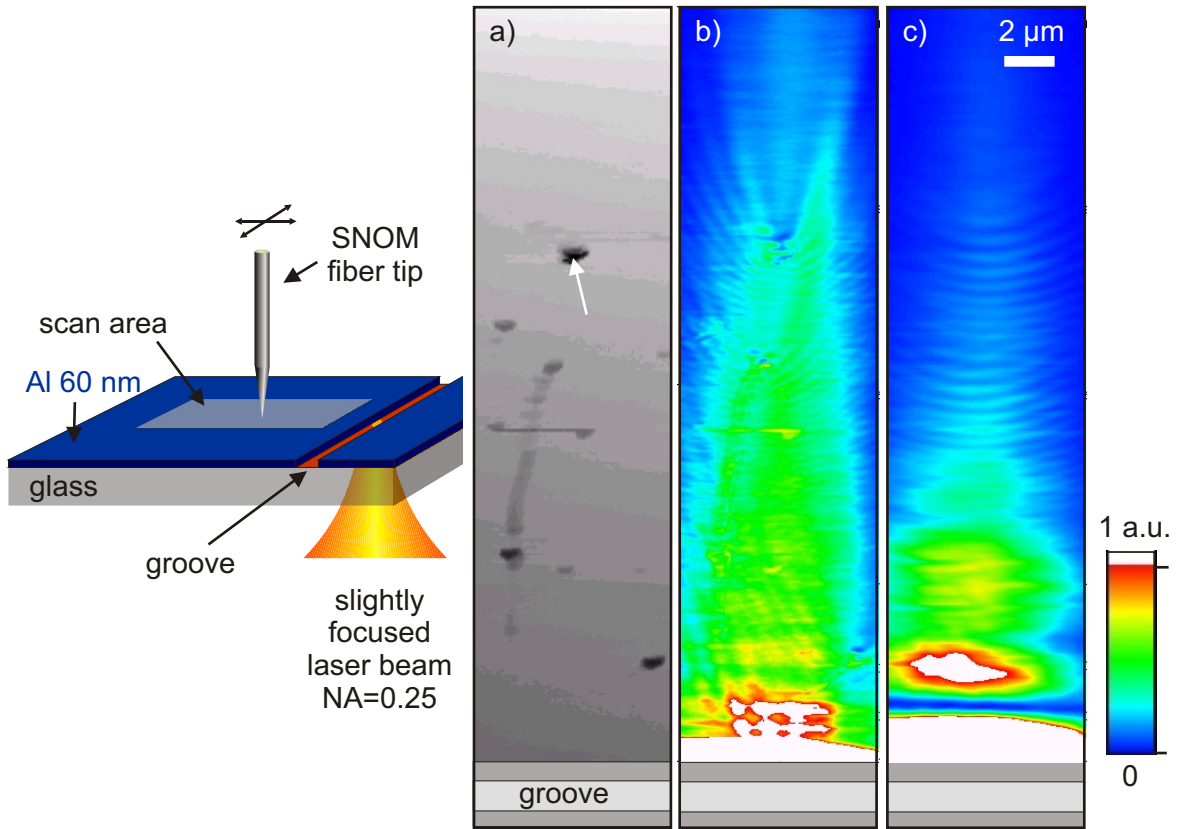
Figure 7.5 *a) Topography, b) near-field intensity observed when the SNOM probe is placed very close to the sample. The slightly focused laser light incident onto the groove (outside the scanned area) in an Al thin film excites the $SPP_{vac/metal}$ waveguide mode. The dust particles sense the mode, causing reflection and scattering, thereby giving rise to stationary intensity patterns. c) Intensity collected with the probing tip retracted by 3 µm away from the surface. The intensity plots b) and c) are scaled equally.*

tuning fork was mechanically excited at its resonance frequency, leading to lateral oscillations of the fiber tip. The interaction between the oscillating tip and the sample increases when the tip is approached towards the sample, and leads to a detuning of the system [188]. This shear-force damping signal was used to sensitively control the tip-sample distance. Such an accurate distance control is essential for mapping evanescent fields such as the one of SPPs. If the probe is placed close to the sample, the tip leads to conversion of the evanescent field into propagating modes inside the fiber probe via scattering. Therefore, the near-field intensity can be detected (far away) at the end of the fiber by a photodetector.

A typical result of such a SNOM measurement is displayed in Fig. 7.5. The light focused onto the sub-$\lambda/2$-groove is partially transmitted though the slit, leading to high intensities close to the groove as shown in Fig. 7.5 b) and c). Some microns away from the groove,

the transmitted light is less intense and does not perturb the SPP mapping. The intensity observed while the probe was scanned at a small height across the sample (near-field intensity) is displayed in Fig. 7.5 b). This image reveals a high intensity coming from the groove at the bottom and propagating away from the launching site. The horizontal extension of roughly $4 \, \mu$m reflects the relatively "large" spot size produced by the small-NA objective. This near-field scan also exhibits fine structures that arise from the interference of the primary SPP and portions reflected and scattered from small particles lying on the metal surface. Especially the particle marked by the arrow in the topographic scan Fig. 7.5 a) causes pronounced reflection and scattering. Measuring the intensity of the same area with the tip retracted by some microns from the interface leads to an intensity pattern that exhibits much fewer details and partially is less intense than the one shown in Fig. 7.5 b). Only the propagating modes (light transmitted directly through the slit and parts of the SPPs scattered by the defects) contribute to the detected intensity, whereas the intensity of the SPPs rapidly decays normal to the interface and is negligible at larger separations. This fact can easily be seen by comparing the intensities in the upper parts of Figs. 7.5 b) and c) (both scans of the intensity are scaled equally).

The SNOM measurements, such as the one displayed in Fig. 7.5, can only be used to map the $SPP_{air/metal}$ waveguide mode, whereas the portion of the field associated with $SPP_{glass/metal}$ that is present in the air region strongly decreases with increasing thickness of the metal film. Hence, for thin metal films which are not too "thick" (in respect to the skin depth $\delta_{skin} = \frac{\lambda}{4\pi Im[n]}$) the modulation Λ_4 (see p. 91) arising from the beating of the two modes could be used to identify $SPP_{glass/metal}$ by measuring the visibility of Λ_4. In our case, the small skin depth of $\delta_{Al}(\lambda = 633 \text{ nm}) = 6.6$ nm together with a film thickness of 60 nm and especially the presence of transmitted light make the beating disappear in the noise.

7.3.2 Propagation of SPPs on triangularly-shaped waveguides

The inherent confinement of the electromagnetic field of an SPP close to an interface may make the "transportation" of light in sub-wavelength spaces by means of SPPs an attractive approach. Such structures might be useful for sensorics or as probes for SNOM and TERS because one could separate the location of the SPP excitation from the active interacting region.

To check this idea, the propagation of SPPs on waveguides having a small width w has to be studied. For the sake of clarity, we start by looking at a rectangularly shaped metal stripe as displayed in Fig. 7.6 a). Similar to dielectric waveguides, reduction of a metal slab to a metal waveguide of *finite width* causes a quantization of the waveguide modes along this (transverse) dimension, as pointed out theoretically by Berini [165, 169, 190] and others [191]. Especially, narrow waveguides ($w \approx \lambda$) can only support the lowest-order modes, as experimentally verified by SNOM mapping of the transverse intensity distribution across
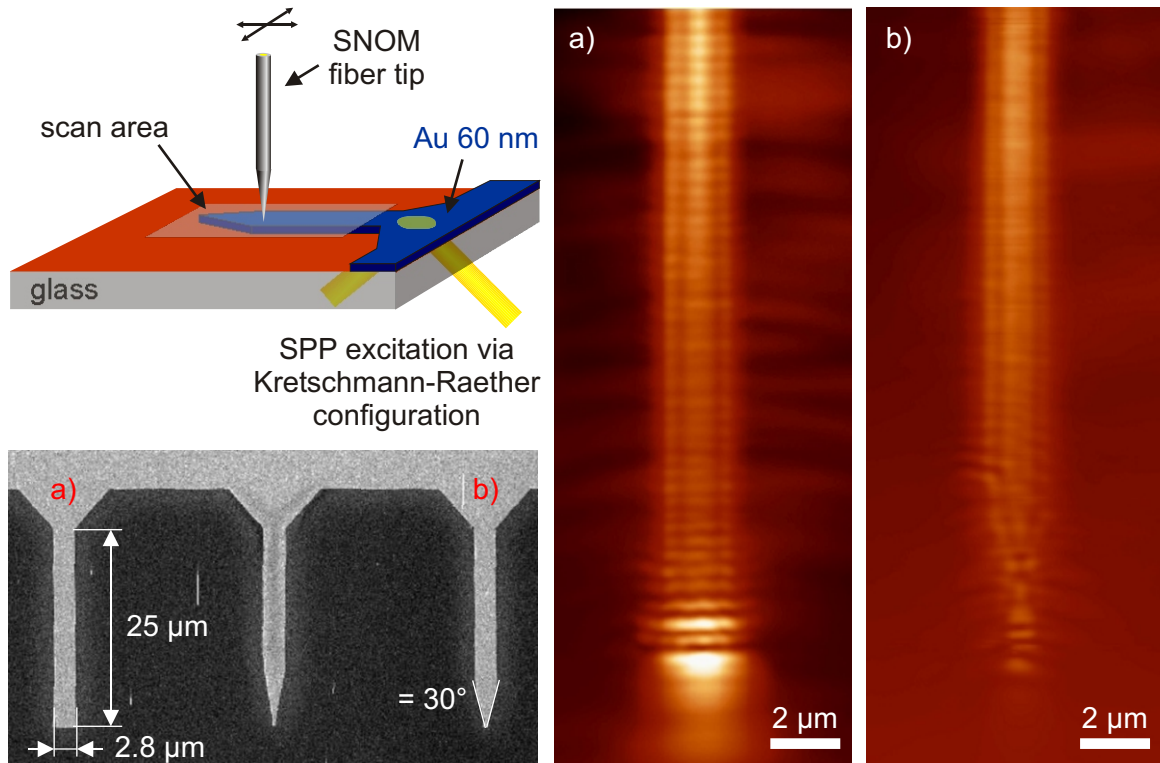
Figure 7.6   *Intensity collected by SNOM, a) on a rectangularly shaped thin gold stripe waveguide, and b) for a waveguide with a triangular end. (bottom left) Scanning electron micrograph of the sample. Data reproduced with kind permission by D. Taverna and J.-C. Weeber [189].*

the waveguide [192–194].

The SNOM images of the stripes displayed in Fig. 7.6 were observed by means of constant-height scans by D. Taverna and J.-C. Weeber [189]. The leaky SPP waveguide mode in the 60-nm-thick gold film was excited via a Kretschmann-Raether configuration at $\lambda = 800$ nm in the supporting gold film at the upper end of the gold stripe, as sketched in Fig. 7.6. This SPP propagates towards the end of the support and excites the different transverse modes of the waveguide. In the case of a rectangular stripe having a width of $w = 2.8$ μm, the SNOM images displayed in Fig. 7.6 a) reveals two minima in the transverse (horizontal) direction. Thus, not only the lowest-order, but also the second-order leaky quasi-TM mode[4] has been excited [191]. The light propagates by means of these modes along the stripe. At the end of the waveguide most of the power is radiated into the forward direction as indicated by the bright colors in Fig. 7.6 a). Similar to the behavior found at an end face of a metal

---

[4]In contrast to slab waveguides, all six field components are present in the case of a waveguide having a finite width. Therefore, a strict classification into TM and TE modes is no longer possible. Nevertheless, the SPP waveguide modes are quasi-TM as long as $w \gg t$.

slab in Sec. 7.2.1, a small amount of the incident power will be back-reflected. The resulting interference with the incident wave causes a small intensity modulation having a constant visibility along the waveguide. Unfortunately, the SNOM tip is not only sensitive to the evanescent modes, but also collects the radiated back-propagating power, especially when placed close to the end of the waveguide. Therefore, the SNOM image may contain artifacts. After studying the most simple case of a rectangular waveguide, we use such a waveguide and change the shape of the terminating end face to a triangle having an opening angle of 30°. The SNOM image displayed in Fig. 7.6 b) reveals a similar transverse near-field intensity profile on the rectangular base, but no longitudinal modulation. This suggests that the presence of a tilted edge does not give rise to as much reflection into a backward propagating-waveguide mode. At the triangularly shaped waveguide end the complex physics of the SPP waveguide modes complicates the interpretation. For narrow metal stripes having widths below the wavelength, the propagation constants of the modes as well as the mode profiles strongly depend on w. Therefore, a definitive answer to the question as to how much of the intensity reaches the very end of the waveguide has not yet been found. The theoretical work in the context of the dispersion in asymmetrically embedded metallic waveguides [169, 191] points to the existence of cut-off widths for the different modes. The attenuation of the bound modes ($SPP_{glass/metal}$ in the slab case), described by the imaginary part of the propagation constants, decreases when the width is reduced as pointed out by Zia *et al.* [191]. Contrary, the attenuation of the leaky modes increases when the width is reduced [191]. This reduction of the propagation length for decreasing width of the silver stripe was found before in experiments done by Lamprecht *et al.* [171] at $\lambda = 633$ nm. Despite the fact that the cut-off widths are substantially smaller [191] for the modes bound to the inner interface, no similar investigations for this case have been published so far.

The triangularly shaped waveguides studied so far were excited using a Kretschmann-Raether arrangement, which is unsuitable for an integration into micrometer-scale devices. As shown in the previous sections, the SPP excitation at groove(s) allows the SPPs to be launched locally. Therefore, incorporation of such launching structures into the triangularly shaped waveguide can further reduce the dimensions of the system, even allowing integration of such structures into the metallized side face of an atomic force tip to produce a novel near-field optical source.

A planar version of such a micrometer-scale plasmon-optical device is sketched in Fig. 7.7. The triangularly shaped waveguide was prepatterned by optical lithography of a photosensitive resist and wet etching. Such processes, commonly used in semiconductor industry, rely on far-field imaging, and therefore the resolution / size of the features is limited physically by the wavelength and NA used. Therefore, FIB milling had to be used to fabricate the sub-wavelength-sized slits and to further improve the shape of the waveguide, especially to sharpen its very end. The latter was done by removing material along the border of the
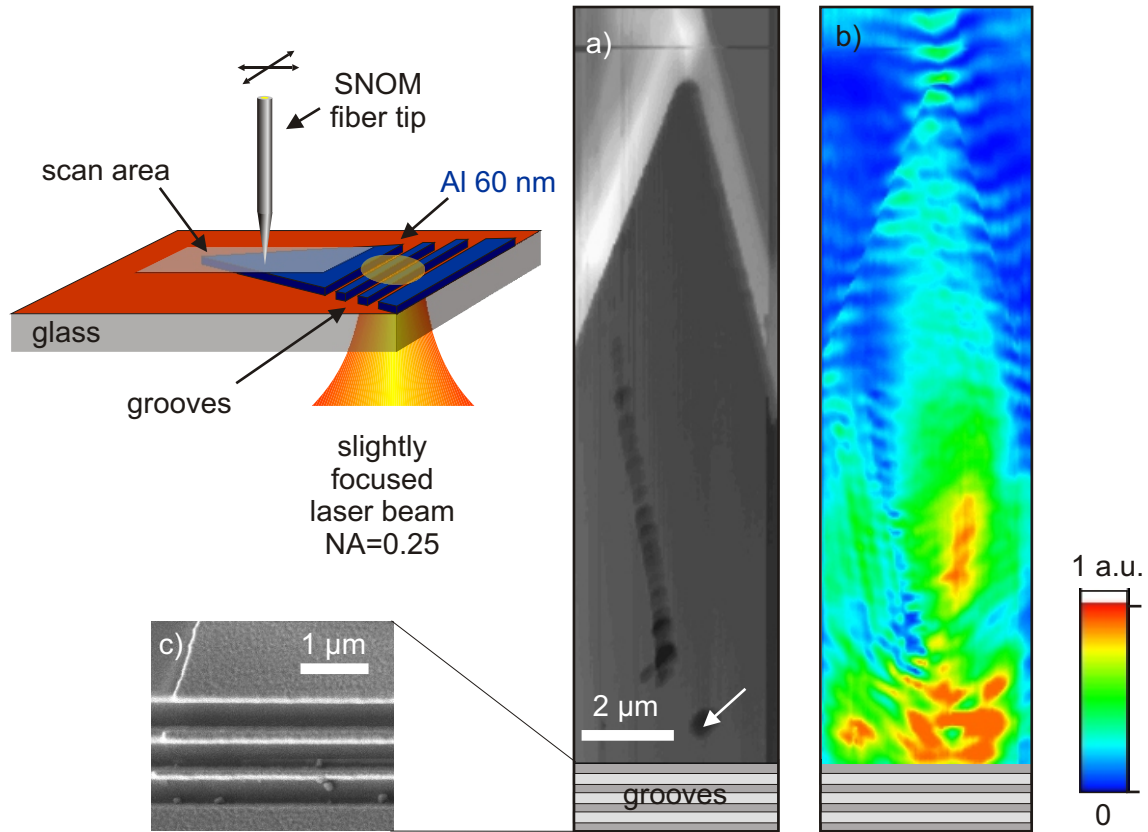
Figure 7.7 *a) Topography, b) near-field intensity observed with the SNOM probe placed very close to the sample. The SPP$_{vac/metal}$ waveguide mode is incident from the bottom and is scattered by the small particle marked by the arrow in a). A part of the plasmon reaches the very end of the tapered waveguide, leading to radiation in the forward direction. c) Scanning electron image of the coupling grooves. The distance between the marked particle and the center of the grooves was $\approx 5~\mu m$.*

triangular end.

The topography of the sample used is displayed in Fig. 7.7 a). This scan shows that not only the metal has been removed during the sharpening but also small 100-nm-deep grooves have been "dug" into the glass cover slip. At the point of intersection of those two grooves, a tip has been formed with a radius of curvature below 200 nm. The SPP$_{air/metal}$ waveguide mode is excited by directing a slightly focused laser beam to the grooves from the glass side (in analogy to Sec. 7.3.1). As displayed in Fig. 7.7 b), the SPP$_{air/metal}$ propagates upwards to the end of the waveguide. The accidentally deposited particle marked by the arrow in Fig. 7.7 a) causes a back-reflection and scattering of the mode. Nevertheless, a significant portion of the launched SPP propagates further towards the very end resulting in a pronounced forward scattering visible by the bright interference pattern around the geometrical apex of the

waveguide structure. The interference pattern is a consequence of the fact that the exciting light is partially transmitted through the slit in the Al film and is superimposed on both the near field and the radiated field of the SPP, which are collected by the uncoated fiber tip.

The SNOM images in Figs. 7.6 and 7.7 show the possibility of guiding light by means of SPP waveguide modes to the end of a triangularly shaped waveguide. The question remaining is: To what extent can light be focused by means of tapered waveguides? Or does the decreasing width of the waveguide cause such a strong damping [191] of the SPP and change of the mode field pattern that it limits the achievable confinement? The answer to this question could be found (in the future) by a three-dimensional simulation or by fabricating the wedge-like structure with an optimized in-coupling groove (array) on an AFM cantilever and mapping the light confinement by processes which are sensitive to the local electric field, e.g. Raman scattering. Such plasmon-coupled optical probes would also benefit from the local field enhancement at the sharp tip apex.

7.4 Summary: optics of SPPs in thin metallic films

Asymmetrically embedded slab waveguides made from thin metallic films support two SPP waveguide modes having their electromagnetic fields mostly concentrated at the vacuum/metal or glass/metal interface. Their propagation constants and field patterns deviate from the case of an interface between two semi-infinite half-spaces because of the presence of the second metal/dielectric boundary. The mode having most of its energy located at the interface between the metal and the dielectric with the smaller dielectric constant can become leaky, whereas the other one remains bound to the interface. Both modes have to be accounted for in plasmonic devices based on thin metallic films. More precisely this means:

- Both modes may be excited by illuminating a groove/slit in the waveguide. Either mode may be addressed preferentially by a proper choice of the width of the groove/slit in the waveguide.

- The modes will be partially converted into each other at points where the translational invariance is violated, such as end faces of the waveguide or grooves/slits in the metal film.

- The SPP waveguide modes propagating across slits/grooves in thin-film waveguides have larger radiation losses compared to what is the case for grooves in thick metals. Because, the presence of the glass interface at groove bottom causes a strong radiation out of the plane of the metal interfaces. Therefore, applications, such as plasmonic wavelength-selective filters should use grooves having a metallic bottom (capable of guiding SPPs) rather than a dielectric bottom in order to minimize the radiative transmission loss.

- A reduction of the width of the waveguide causes a discretization of the modes in the transverse direction. The lowest-order modes may be used to guide light by means of SPPs into sub-wavelength spaces.

Chapter 8

Outlook

This thesis comes to its end without repeating all conclusions from the previous chapters. However, some of them are worth being set more in context with each other. This selection is subjective, especially the future perspectives reflecting more my personal experiences and hobbyhorses than being "universal".

Nanooptical effects are entering into our (scientific) lives silently and gradually. Undoubtedly, the increased sensitivity in (bio-) chemical sensing using SERS- or SPR-based sensors attracts a lot of attention, boosting other natural sciences by providing them with useful tools. Other near-field optical research fields such as SNOM or TERS are still basic research rather than being established as widely used methods. Their great potential has already been demonstrated and they provide insight into processes down to the molecular level, as shown for instance with carbon nanotubes. The price for this excellent resolution beyond the diffraction limit of classical optics has to be paid by a larger effort in the measurement itself and a more difficult interpretation of the observations, as discussed in chapter 5.

The SPP waveguide modes discussed in the second part of the thesis for flat metal surfaces likewise exist on nonplanar metallic structures such as cylindrical wires or metal-coated tips used in SNOM or TERS. These modes have to be accounted for in the theoretical modelling and experiments. Fortunately, they also provide a wide playground for the optimization of near-field optical probes.

Before plasmonic applications will enter into widely used technologies, such as optical interconnections on integrated circuits or data processing, some important problems have to be solved:

- The intrinsic damping of SPPs in the metal restricts their propagation length especially when the mode volume is strongly confined. For instance, the MIM waveguide displayed in Fig. 6.4 can provide a sub-λ confinement in one dimension for narrow gaps, but the imaginary part and therewith the damping significantly increase for a reduced width of the gap. On the other hand, long-ranging SPP modes exist in (nearly) symmetrically embedded thin metallic waveguides and at lower frequencies. In both cases, the larger propagation length has to be bought through a larger extension of the waves into the

dielectric and, hence, a reduced confinement. Therefore, a trade-off between confinement and damping has to be made in applications such as optical interconnections.

- The weak guiding of SPPs in the red and infrared spectral regions around bends in waveguides (see Sec. 6.3.1), the strong reflection and scattering at steps, and the large transmission loss (see Sec. 7.2.2) at grooves in asymmetrically embedded thin-film metallic waveguides imply that it is absolutely necessary to well control the nanopatterning process and that more sophisticated structures are required.

Nevertheless, tailoring plasmonic properties by altering the density of electromagnetic surface states has the potential to be used widely. For instance, the transmission of light through small holes and arrays of them can be enhanced by structuring the interface on the incident side, moreover even a directional emission can be achieved with this sub-λ holes surrounded by a nanopatterned interface on the transmission side. These phenomena might be used in optical data storage or to collect the light from a large area and then guide it to a detector of nanoscale dimensions [195]. The drastically reduced capacitance would allow ultrahigh-speed communication.

Moreover, researchers have realized that the unintentional and unavoidable excitation of SPPs in the metal electrodes in optoelectronic devices such as (organic) light-emitting diodes opens ways to optimize their performance, either by minimizing the coupling via spacer layers, by using the increased field caused by the SPPs to excite dyes, or by improving the light out-coupling by means of SPPs.

Bibliography

[1] V. G. Veselago. The electrodynamics of substances with simultaneously negative values of ϵ and μ. *Sov. Phys. Usp.*, 10:509–514, 1968.

[2] D. R. Smith, J. B. Pendry, and M. C. K. Wiltshire. Metamaterials and Negative Refractive Index. *Science*, 305:788–792, 2004.

[3] M. Moskovits. Surface-enhanced spectroscopy. *Rev. Mod. Phys.*, 57:783–826, 1985.

[4] A. Otto, I. Mrozek, H. Grabhorn, and W. Akemann. Surface-enhanced Raman scattering. *J. Phys.: Condens. Matter*, 4:1143–1212, 1992.

[5] S. Nie and S. R. Emory. Probing Single Molecules and Single Nanoparticles by Surface-Enhanced Raman Scattering. *Science*, 275:1102–1106, 1997.

[6] Y. Inouye and S. Kawata. Near-field scanning optical microscope with a metallic probe tip. *Opt. Lett.*, 19:159–161, 1994.

[7] M. Specht, J. D. Pedarnig, W. M. Heckl, and T. W. Hänsch. Scanning Plasmon Near-Field Microscope. *Phys. Rev. Lett.*, 68:476–479, 1992.

[8] R. Bachelot, P. Gleyzes, and A. C. Boccara. Near field optical microscopy by local perturbation of a diffraction spot. *Microsc. Microanal. Microstruct.*, 5:389–397, 1994.

[9] F. H'dhili, R. Bachelot, G. Lerondel, and D. Barchiesi. Near-field optics: Direct observation of the field enhancement below an apertureless probe using a photosensitive polymer. *Appl. Phys. Lett.*, 79:4019–4021, 2001.

[10] H. Raether. *Surface Plasmons*. Springer-Verlag, Berlin, 1988.

[11] B. Liedberg, C. Nylander, and I. Lundstrom. Biosensing with surface plasmon resonance - how it all started. *Biosens. Bioelectron.*, 10:i–ix, 1995.

[12] J. Homola, S. S. Yee, and G. Gauglitz. Surface plasmon resonance sensors: review. *Sensors and Actuators B*, 54:3–15, 1999.

[13] E. Ozbay. Plasmonics: Merging Photonics and Electronics at Nanoscale Dimensions. *Science*, 311:189–193, 2006.

[14] W. L. Barnes. Fluorescence near interfaces: the role of photonic mode density. *J. Mod. Opt.*, 45:661–699, 1998.

[15] W. L. Barnes. Electromagnetic crystals for surface plasmon polaritons and the extraction of light from emissive devices. *J. Lightw. Techn.*, 17:2170–2182, 1999.

[16] J. Vučković, M. Lončar, and A. Scherer. Surface plasmon enhanced light-emitting diode. *J. Quantum Electronics*, 36:1131–1144, 2000.

[17] S. Wedge and W. L. Barnes. Surface plasmon-polariton mediated light emission through thin metal films. *Opt. Express*, 12:3673–3685, 2004.

[18] J. D. Jackson. *Klassische Elektrodynamik*. de Gruyter, Berlin, 3rd edition, 2002.

[19] C. F. Bohren and D. R. Huffman. *Absorption and Scattering of Light by Small Particles*. John Wiley & Sons, New York, 1983.

[20] C. Girard and A. Dereux. Near-field optics theories. *Rep. Prog. Phys.*, 59:657–699, 1996.

[21] M. N. O. Sadiku. *Numerical techniques in electromagnetics*. CRC Press LLC, Boca Raton (Fl), 2nd edition, 2001.

[22] Ch. Hafner. Beiträge zur Berechnung der Ausbreitung elektromagnetischer Wellen in zylindrischen Strukturen mit Hilfe des "Point-Matching"-Verfahrens. Diss. ETH Nr. 6683, Eidgenössische Technische Hochschule Zürich, 1980.

[23] Ch. Hafner. *The Generalized Multipole Technique for Computational Electromagnetics*. Artech House Books, Boston, 1990.

[24] Ch. Hafner. *Post-modern Electromagnetics: Using Intelligent MaXwell Solvers*. John Wiley & Sons, Chichester, 1999.

[25] L. Novotny and Ch. Hafner. Light propagation in a cylindrical waveguide with a complex, metallic, dielectric function. *Phys. Rev. E*, 50:4094–4106, 1994.

[26] E. Moreno, D. Erni, Ch. Hafner, R. E. Kunz, and R. Vahldieck. Modeling and optimization of non-periodic grating couplers. *Opt. Quant. Electron.*, 34:1051–1069, 2002.

[27] Ch. Hafner. Multiple multipole program computation of periodic strucures. *J. Opt. Soc. Am. A*, 12:1057–1067, 1995.

[28] Th. Geiler. ϕ-Scatterometrie und optische Nahfeld Mikroskopie für industrielle CMOS Strukturen. Diplomarbeit, Technische Universität Dresden, 2005.

[29] L. Novotny, D. W. Pohl, and P. Regli. Near-field, far-field and imaging properties of the 2D aperture SNOM. *Ultramicroscopy*, 57:180–188, 1995.

[30] L. Novotny. Light propagation and light confinement in near-field optics. Diss. ETH No. 11420, Eidgenössische Technische Hochschule Zürich, 1996.

[31] E. Moreno. MMP modelling and optimization of photonic crystals, optical devices and nanostrucures. Diss. ETH No. 14553, Eidgenössische Technische Hochschule Zürich, 2002.

[32] L. H. Bomholt. MMP-3D – A Computer Code for Electromagnetic Scattering Based on the GMT. Diss. ETH No. 9225, Eidgenössische Technische Hochschule Zürich, 1990.

[33] P. Regli. Automatische Wahl der sphärischen Entwicklungsfunktionen für die 3D-MMP Methode. Diss. ETH Nr. 9946, Eidgenössische Technische Hochschule Zürich, 1992.

[34] Ch. Hafner and L. Bomholt. *The 3D Electrodynamic Wave Simulator.* John Wiley & Sons, Chichester, 1993.

[35] E. Moreno. Brief introduction to the multiple multipole method. Workshop on theoretical methods in scattering of surface plasmon polaritons, Madrid, 2005.

[36] http://www-europe.sgi.com/products/evaluation.

[37] Ch. Hafner. MaX-1 A Visual Electromagnetics Platform for PCs. John Wiley & Sons, Chichester, 1998.

[38] E. Moreno, D. Erni, Ch. Hafner, and R. Vahldieck. Multiple multipole method with automatic multipole setting applied to the simulations of surface plasmons in metallic nanostructures. *J. Opt. Soc. Am. A*, 19:101–111, 2002.

[39] G. Mie. Beiträge zur Optik trüber Medien, speziell kolloidaler Metallösungen. *Annalen der Physik*, 25:377–445, 1908.

[40] R. M. Stöckle, Y. D. Suh, V. Deckert, and R. Zenobi. Nanoscale chemical analysis by tip-enhanced Raman spectroscopy. *Chem. Phys. Lett.*, 318:131–136, 2000.

[41] M. S. Anderson. Locally enhanced Raman spectroscopy with an atomic force microscope. *Appl. Phys. Lett.*, 76:3130–3132, 2000.

[42] N. Hayazawa, Y. Inouye, Z. Sekkat, and S. Kawata. Metallized tip amplification of near-field Raman scattering. *Opt. Commun.*, 183:333–336, 2000.

[43] A. Hartschuh, H. N. Pedrosa, L. Novotny, and T. D. Krauss. Simultaneous Fluorescence and Raman Scattering from Single Carbon Nanotubes. *Science*, 301:1354–1356, 2003.

[44] A. Wokaun. Surface enhancement of optical fields - Mechanism and application. *Molecular Physics*, 56:1–33, 1985.

[45] Sopra GmbH. n & k database. www.sopra.org, August 2003.

[46] Th. Härtling. Nano-optical addressing of ferroelectric domains using novel laser polarization modes. Diplomarbeit, Technische Universität Dresden, 2004.

[47] Th. Härtling and L. M. Eng. Gold-particle-mediated detection of ferroelectric domains on the nanometer scale. *Appl. Phys. Lett.*, 87:142902–1–3, 2005.

[48] J. Renger, S. Grafström, V. Deckert, and L. M. Eng. Evanescent wave scattering and local electric field enhancement at ellipsoidal silver particles in the vicinity of a glass surface. *J. Opt. Soc. Am. A*, 21:1362–1367, 2004.

[49] D. W. Lynch and W. R. Hunter. *Handbook of Optical Constants of Solids II*, chapter Introduction to the Data for Several Metals, page 350. Academic Press, New York, 2nd edition, 1985.

[50] N. Calander and M. Willander. Theory of surface-plasmon resonance optical-field enhancement at prolate spheroids. *J. Appl. Phys.*, 92:4878–4884, 2002.

[51] A. Wokaun, J. P. Gordon, and P. F. Liao. Radiation Damping in Surface-Enhanced Raman Scattering. *Phys. Rev. Lett.*, 48:957–960, 1982.

[52] M. R. Beversluis, A. Bouhelier, and L. Novotny. Continuum generation from single gold nanostructures through near-field mediated intraband transitions. *Phys. Rev. B*, 68:115433–1–10, 2003.

[53] A. Bouhelier, M. R. Beversluis, and L. Novotny. Characterization of nanoplasmonic structures by locally excited photoluminescence. *Appl. Phys. Lett.*, 83:5041–5043, 2003.

[54] R. Antoine, M. Pellarin, B. Palpant, M. Broyer, B. Prével, P. Galletto, P. F. Brevet, and H. H. Girault. Surface plasmon enhanced second harmonic response from gold clusters embedded in an alumina matrix. *J. Appl. Phys.*, 84:4532–4536, 1998.

[55] A. Pinchuk and U. Kreibig. Interface decay channels of particle surface plasmon resonance. *New J. Phys.*, 5:151–1–15, 2003.

[56] J. Lermé. Introduction of quantum finite-size effects in the Mie's theory for a multilayered metal sphere in the dipolar approximation: Application to free and matrix-embedded noble metal clusters. *Eur. Phys. J. D.*, 10:265–277, 2000.

[57] U. Kreibig and L. Genzel. Optical absorption of small metallic particles. *Surf. Science*, 156:678–700, 1985.

[58] D. Dalacu and L. Martinu. Optical properties of discontinuous gold films: finite-size effects. *J. Opt. Soc. Am. B*, 18:85–92, 2001.

[59] L. B. Scaffardi, N. Pellegri, O. de Sanctis, and J. O. Tocho. Sizing gold nanoparticles by optical extinction spectroscopy. *Nanotechn.*, 16:158–163, 2005.

[60] R. M. Stöckle, V. Deckert, Ch. Fokas, and R. Zenobi. Controlled Formation of Isolated Silver Islands for Surface-Enhanced Raman Scattering. *Applied Spectroscopy*, 54:1577–1583, 2000.

[61] W. Rechberger, A. Hohenau, A. Leitner, J. R. Krenn, B. Lamprecht, and F. R. Aussenegg. Optical properties of two interacting gold nanoparticles. *Opt. Commun.*, 220:137–141, 2003.

[62] K.-H. Su, Q.-H. Wei, X. Zhang, J. J. Mock, D. R. Smith, and S. Schultz. Interparticle Coupling Effects on Plasmon Resonances of Nanogold Particles. *Nano Lett.*, 3:1087–1090, 2004.

[63] T. Atay, J.-H. Song, and A. V. Nurmikko. Strongly Interacting Plasmon Nanoparticle Pairs: From Dipole-Dipole Interaction to Conductively Coupled Regime. *Nano Lett.*, 4:1627–1631, 2004.

[64] L. Gunnarsson, E. J. Bjerneld, H. Xu, S. Petronis, B. Kasemo, and M. Käll. Interparticle coupling effects in nanofabricated substrates for surface-enhanced Raman scattering. *Appl. Phys. Lett.*, 78:802–804, 2001.

[65] C. L. Haynes, A. D. McFarland, L. L. Zhao, R. P. Van Duyne, G. C. Schatz, L. Gunnarsson, J. Prikulis, B. Kasemo, and Mikael Käll. Nanoparticle Optics: The Importance of Radiative Dipole Coupling in Two-Dimensional Nanoparticle Arrays. *J. Phys. Chem. B*, 107:7337–7342, 2003.

[66] N. Félidj, S. Lau Truong, J. Aubard, G. Lévi, J. R. Krenn, A. Hohenau, A. Leitner, and F. R. Aussenegg. Gold particle interaction in regular arrays probed by surface enhanced Raman scattering. *J. Chem. Phys.*, 120:7141–7146, 2004.

[67] N. Félidj, J. Aubard, G. Lévi, J. R. Krenn, G. Schider, A. Leitner, and F. R. Aussenegg. Enhanced substrate-induced coupling in two-dimensional gold nanoparticle arrays. *Phys. Rev. B*, 66:245407–1–7, 2002.

[68] J. P. Kottmann and O. J. F. Martin. Retardation-induced plasmon resonances in coupled nanoparticles. *Opt. Lett.*, 26:1096–1098, 2001.

[69] C. Rockstuhl. *Properties of light fields near submicro and nano-scale structures.* PhD thesis, Université de Neuchâtel, 2004.

[70] P. Nordlander, C. Oubre, E. Prodan, K. Li, and M. I. Stockmann. Plasmon hybridization in nanoparticle dimers. *Nano Lett.*, 4:899–903, 2004.

[71] J. J. Xiao, J. P. Huang, and K. W. Yu. Optical response of strongly coupled metal nanoparticles in dimer arrays. *Phys. Rev. B*, 71:045404–1–8, 2005.

[72] J. R. Krenn, A. Dereux, J. C. Weeber, E. Bourillot, Y. Lacroute, J. P. Goudonnet, G. Schider, W. Gotschy, A. Leitner, F. R. Aussenegg, and C. Girard. Squeezing the Optical Near-Field Zone by Plasmon Coupling of Metallic Nanoparticles. *Phys. Rev. Lett.*, 82:2590–2593, 1999.

[73] A. M. Stefan and H. A. Atwater. Plasmonics: Localization and guiding of electromagnetic energy in metal/dielectric structures. *Appl. Phys. Lett.*, 98:11101–1–10, 2005.

[74] M. L. Brongersma, J. W. Hartman, and H. A. Atwater. Electromagnetic energy transfer and switching in nanoparticle chain arrays below the diffraction limit. *Phys. Rev. B*, 62:16356–16359, 2000.

[75] S. A. Maier, M. L. Brongersma, P. G. Kik, S. Meltzer, A. A. G. Requicha, and H. A. Atwater. Plasmonics - A route to nanoscale optical devices. *Adv. Mater.*, 13:1501–1505, 2001.

[76] K. Li, M. I. Stockman, and D. J. Bergman. Self-Similar Chain of Metal Nanospheres as an Efficient Nanolens. *Phys. Rev. Lett.*, 91:227402–1–4, 2003.

[77] R. Lettow. Nano-Raman-Spectroscopy with Single Metal Spheres. Diplomarbeit, Technische Universität Dresden, 2005.

[78] T. Otto, S. Grafström, J. Seidel, and L. M. Eng. Novel transparent electrodes for electro-optical near-field microscopy. In *SPIE Int. Soc. Opt. Eng. Adv. Mater.: Advanced optical materials*, volume 5122, pages 366–370, 2003.

[79] Final report of the workpackage WP19.1.1 (Joint Activity: "Superfocusing through tuned plasmon resonators"). European Network of Excellence - Plasmo Nano Devices, 2005.

[80] K. Lindfors, T. Kalkbrenner, P. Stoller, and V. Sandoghdar. Optical Detection and Spectroscopy of very small Gold Nanoparticles. The 8th International Conference on Near-field Nano Optics & Related Techniques, Seoul Korea (2004).

[81] F. Zenhausern, M. P. O'Boyle, and H. K. Wickramasinghe. Apertureless near-field optical microscope. *Appl. Phys. Lett.*, 65:1623–1625, 1994.

[82] T. Kalkbrenner. *Charakterisierung und Manipulation der Plasmonenresonanz eines einzelnen Goldnanopartikles*. PhD thesis, Universität Konstanz, 2002.

[83] B. Knoll and F. Keilmann. Scanning microscopy by mid-infrared near-field scattering. *Appl. Phys. A*, 66:477–481, 1998.

[84] J. Wessel. Surface-enhanced optical microscopy. *J. Opt. Soc. Am. B*, 2:1538–1541, 1985.

[85] A. Hartschuh, N. Anderson, and L. Novotny. Near-field Raman spectroscopy using a sharp metal tip. *J. Micros.*, 210:234–240, 2003.

[86] A. Bouhelier, M. Beversluis, A. Hartschuh, and L. Novotny. Near-Field Second Harmonic Generation Induced by Local Field Enhancement. *Phys. Rev. Lett.*, 90:13903–1–4, 2003.

[87] T. Kalkbrenner, M. Ramstein, J. Mlynek, and V. Sandoghdar. A single gold particle as a probe for apertureless scanning near-field microscopy. *J. Microsc.*, 202:72–76, 2000.

[88] T. Kalkbrenner, U. Håkanson, A. Schädle, S. Burger, C. Henkel, and V. Sandoghdar. Optical Microscopy via Spectral Modifications of a Nanoantenna. *Phys. Rev. Lett.*, 95:200801–1–4, 2005.

[89] O. Sqalli, M.-P. Bernal, P. Hoffmann, and F. Marquis-Weible. Improved tip performance for scanning near-field optical microscopy by the attachment of a single gold nanoparticle. *Appl. Phys. Lett.*, 76:2134–2136, 2000.

[90] O. Sqalli, I. Utke, P. Hoffmann, and F. Marquis-Weible. Gold elliptical nanoantennas as probes for near field optical microscopy. *J. Appl. Phys.*, 92:1078–1083, 2002.

[91] Y. C. Martin, H.F. Hamann, and H. K. Wickramasinghe. Strength of the electric field in apertureless near-field optical microscopy. *J. Appl. Phys.*, 89:5774–5778, 2001.

[92] P. K. Aravind and H. Metiu. The effects of the interaction between resonances in the electromagnetic response of a sphere-plane structure; Application to surface enhanced spectroscopy. *Surf. Science*, 124:506–528, 1983.

[93] J.-J. Greffet and R. Carminati. Image Formation in Near-Field Optics. *Prog. Surf. Sci.*, 56:133–237, 1997.

[94] M. Xiao. Theoretical treatment for scattering scanning near-field optical microscopy. *J. Opt. Soc. Am. A*, 14:2977–2984, 1997.

[95] A. V. Zayats. Electromagnetic field enhancement in the context of apertureless near-field microscopy. *Opt. Commun.*, 161:156–162, 1999.

[96] J. T. Krug, E. J. Sánchez, and X. S. Xie. Design of near-field optical probes with optimal field enhancement by finite difference time domain electromagnetic simulation. *J. Chem. Phys.*, 116:10895–10901, 2002.

[97] V. V. Klimov, M. Ducloy, and V. S. Letokkov. A model of an apertureless scanning microscope with a prolate nanospheroid as a tip and an excited molecule as an object. *Chem. Phys. Lett.*, 358:192–198, 2002.

[98] J. A. Porto, P. Johansson, S. P. Apell, and T. López-Riós. Resonance shift effects in apertureless scanning near-field optical microscopy. *Phys. Rev. B*, 67:85409–1–11, 2003.

[99] C. Sönnichsen, S. Geier, N. E. Hecker, G. von Plessen, J. Feldmann, H. Ditlbacher, B. Lamprecht, J. R. Krenn, F. R. Aussenegg, V. Z.-H. Chan, J. P. Spatz, and M. Möller. Spectroscopy of single metallic nanoparticles using total internal reflection microscopy. *Appl. Phys. Lett.*, 77:2949–2951, 2000.

[100] G. A. Wurtz, N. M. Dimitrijevic, and G. P. Wiederrecht. The Spatial Extension of the Field Scattered by Silver Nanoparticles Excited near Resonance as Observed by Apertureless Near-Field Optical Microscopy. *Jpn. J. Appl. Phys.*, 41:L351–L354, 2002.

[101] K. Fukuzawa and H. Kuwano. Scattering of evanescent light by a finite-size probe in near-field scanning optical microscopy. *J. Appl. Phys.*, 80:4799–4803, 1996.

[102] C. Girard, A. Dereux, and J.-C. Weeber. Near-field optical contrasts in the Fresnel evanescent wave. *Phys. Rev. E*, 58:1081–1085, 1998.

[103] M. Quinten, A. Pack, and R. Wannemacher. Scattering and extinction of evanescent waves by small particles. *Appl. Phys. B*, 68:87–92, 1999.

[104] R. Wannemacher, A. Pack, and M. Quinten. Resonant absorption and scattering in evanescent fields. *Appl. Phys. B*, 68:225–232, 1999.

[105] H. Chew, D. S. Wang, and M. Kerker. Elastic scattering of evanescent electromagnetic waves. *Appl. Opt.*, 18:2679–2687, 1979.

[106] C. Liu, T. Kaiser, S. Lange, and G. Schweiger. Structural resonances in a dielectric sphere illuminated by an evanescent wave. *Opt. Commun.*, 117:521–531, 1995.

[107] A. V. Shchegrov, K. Joulain, R. Carminati, and J.-J. Greffet. Near-field Spectral Effects due to Electromagnetic Surface Excitations. *Phys. Rev. Lett.*, 85:1548–1551, 2000.

[108] M. Born and E. Wolf. *Principles of Optics.* Cambridge University Press, Cambridge, 7th edition, 1999.

[109] B. Hecht. *Forbidden Light Scanning Near-Field Optical Microscopy.* PhD thesis, University of Basel, Basel, 1996.

[110] L. Novotny, D. W. Pohl, and B. Hecht. Scanning near-field optical probe with ultrasmall spot size. *Opt. Lett.*, 20:970–972, 1995.

[111] B. Hecht, H. Heinzelmann, and D. W. Pohl. Combined aperture SNOM/PSTM: best of both worlds? *Ultramicroscopy*, 57:228–234, 1995.

[112] M. Quinten, A. Leitner, J. R. Krenn, and F. R. Aussenegg. Electromagnetic energy transport via silver nanoparticles. *Opt. Lett.*, 23:1331–1333, 1998.

[113] R. Hillenbrand. Towards phonon photonics: scattering-type near-field optical microscopy reveals phonon-enhanced near-field interaction. *Ultramicroscopy*, 100:421–427, 2004.

[114] R. Hillenbrand, T. Taubner, and F. Keilmann. Phonon-enhanced light-matter interaction at the nanometre scale. *Nature*, 418:159–162, 2002.

[115] R. Hillenbrand and F. Keilmann. Material-specific mapping of metal/semiconductor/dielectric nanosystems at 10 nm resolution by backscattering near-field optical microscopy. *Appl. Phys. Lett.*, 80:25–27, 2002.

[116] B. Knoll and F. Keilmann. Enhanced dielectric contrast in scattering-type scanning near-field optical microscopy. *Opt. Commun.*, 182:321–328, 2000.

[117] P. K. Aravind and H. Metiu. Use of a Perfectly Conducting Sphere to excite the plasmon of a flat surface. 1. Calculation of the local field with Applications to Surface-Enhanced Spectroscopy. *J. Phys. Chem.*, 86:5076–5084, 1982.

[118] R. Ruppin. Infrared active modes of dielectric crystallites on a substrate. *Surf. Science*, 58:550–556, 1976.

[119] R. Ruppin. Surface modes and optical absorption of a small sphere above a substrate. *Surf. Science*, 127:108–118, 1983.

[120] F. Engelbrecht and R. Helbig. Effect of crystal anisotropy on the infrared reflectivity of 6H-SiC. *Phys. Rev. B*, 48:15698–15707, 1993.

[121] M. S. Anderson. Enhanced infrared absorption with dielectric nanoparticles. *Appl. Phys. Lett.*, 83:2964–2966, 2003.

[122] T. Taubner, F. Keilmann, and R. Hillenbrand. Nanomechanical Resonance Tuning and Phase Effects in Optical Near-Field Interaction. *Nano Letters*, 4:1669–1672, 2004.

[123] L. Aigouy, F. X. Andréani, A. C. Boccara, J. C. Rivoal, J. A. Porto, R. Carminati, J.-J. Greffet, and R. Mégy. Near-field optical spectroscopy using an incoherent light source. *Appl. Phys. Lett.*, 76:397–399, 2000.

[124] R. Hillenbrand and F. Keilmann. Complex Optical Constants on a Subwavelength Scale. *Phys. Rev. Lett.*, 85:3029–3032, 2000.

[125] B. Hecht, H. Bielefeldt, Y. Inouye, and D. W. Pohl. Facts and artifacts in near-field optical microscopy. *J. Appl. Phys.*, 81:2492–2498, 1997.

[126] S. Schneider. Internal communication. to be published, 2006.

[127] S. Schneider, S. Grafström, and L. M. Eng. Scattering near-field optical microscopy of optically anisotropic systems. *Phys. Rev. B*, 71:115418–1–8, 2005.

[128] L. Novotny, M. R. Beversluis, K.S. Youngworth, and T. G. Brown. Longitudinal Field Modes Probed by Single Molecules. *Phys. Rev. Lett.*, 86:5251–5254, 2001.

[129] W. L. Barnes, S. C. Kitson, T. W. Preist, and J. R. Sambles. Photonic surfaces for surface-plasmon polaritons. *J. Opt. Soc. Am. A*, 14:1654–1661, 1997.

[130] H. Ditlbacher, J. R. Krenn, G. Schider, A. Leitner, and F. R. Aussenegg. Two-dimensional optics with surface plasmon polaritons. *Appl. Phys. Lett.*, 81:1762–1764, 2002.

[131] R. Charbonneau, P. Berini, E. Berolo, and E. Lisicka-Shrzek. Experimental observation of plasmon-polariton waves supported by a thin metal film of finite width. *Opt. Lett.*, 25:844–846, 2000.

[132] J. Zenneck. Über die Fortpflanzung ebener elektromagnetischer Wellen längs einer ebenen Leiterfläche und ihre Beziehung zur drahtlosen Telegraphie. *Ann. d. Physik*, 23:846–866, 1907.

[133] A. Sommerfeld. Über die Ausbreitung der Wellen in der drahtlosen Telegraphie. *Ann. d. Physik*, 28:665–736, 1909.

[134] C. J. Powell and J. B. Swan. Effect of Oxidation on the Characteristic Loss Spectra of Aluminum and Magnesium. *Phys. Rev.*, 118:640–643, 1960.

[135] R. H. Ritchie. Plasma Losses by Fast Electrons in Thin Films. *Phys. Rev.*, 106:874–881, 1957.

[136] R. A. Ferrell. Predicted Radiation of Plasma Oscillations in Metal Films. *Phys. Rev.*, 111:1214–1222, 1958.

[137] A. Otto. Excitation of nonradiative surface plasma waves in silver by the method of frustrated total reflection. *Z. Phys.*, 216:398–410, 1968.

[138] E. Kretschmann and H. Raether. Radiative decay of non-radiative surface plasmons excited by light. *Z. Naturforsch.*, 23a:2135–2136, 1968.

[139] F. Abelès and T. Lopez-Rios. Surface Polaritons at Metal Surfaces and Interfaces. In V. M. Agranovich and D. L. Mills, editors, *Surface polaritons*, pages 239–274. North-Holland Publishing Company, Amsterdam, 1982.

[140] E. T. Arakawa, M. W. Williams, R. N. Hamm, and R. H. Ritchie. Effect of Damping on Surface Plasmon Dispersion. *Phys. Rev. Lett.*, 31:1127–1129, 1973.

[141] G. S. Kovener, Jr. R. W. Alexander, and R. J. Bell. Surface electromagnetic waves with damping. I. Isotropic media. *Phys. Rev. B*, 14:1458–1464, 1976.

[142] D. N. Mirlin. Surface Phonon Polaritons in Dielectrics and Semiconductors. In V. M. Agranovich and D. L. Mills, editors, *Surface polaritons*, pages 3–67. North-Holland Publishing Company, Amsterdam, 1982.

[143] W. L. Barnes, A. Dereux, and T. W. Ebbesen. Surface plasmon subwavelength optics. *Nature*, 424:824–830, 2003.

[144] W. P. Chen, G. Ritchie, and E. Burstein. Excitation of Surface Electromagnetic Waves in Attenuated Total-Reflection Prism Configurations. *Phys. Rev. Lett.*, 37:993–997, 1976.

[145] P. Dawson, F. de Fornel, and J.-P. Goudonnet. Imaging of Surface Plasmon Propagation and Edge Interaction Using a Photon Scanning Tunneling Microscope. *Phys. Rev. Lett.*, 72:2927–2930, 1994.

[146] J. Seidel. *Propagation, Scattering and Amplification of Surface Plasmons in Thin Silver Films*. PhD thesis, Dissertation Technische Universität Dresden, 2005.

[147] G. I. Stegeman, R. F. Wallis, and A. A. Maradudin. Excitation of surface polaritons by end-fire coupling. *Opt. Lett.*, 8:386–388, 1983.

[148] H. Ditlbacher, J. R. Krenn, A. Hohenau, A. Leitner, and F. R. Aussenegg. Efficiency of local light-plasmon coupling. *Appl. Phys. Lett.*, 83:3665–3667, 2003.

[149] R. F. Wallis, A. A. Maradudin, and G. I. Stegeman. Surface polariton reflection and radiation at end faces. *Appl. Phys. Lett.*, 42:764–766, 1983.

[150] A. A. Maradudin, R. F. Wallis, and G. I. Stegeman. The optics of surface and guided wave polaritons. *Prog. Surf. Sci.*, 33:171–258, 1990.

[151] H. A. Jamid and S. J. Al-Bader. Diffraction of Surface Plasmon-Polaritons in an Abruptly Terminated Dielectric-Metal Interface. *IEEE Photon. Technol. Lett.*, 7:321–323, 1995.

[152] K. Hasegawa, J. U. Nöckel, and M. Deutsch. Surface plasmon polariton propagation around bends at a metal-dielectric interface. *Appl. Phys. Lett.*, 84:1835–1837, 2004.

[153] Bo E. Sernelius. *Surface Modes in Physics*. Wiley-VCH, Berlin, 2001.

[154] H. A. Jamid and S. J. Al-Bader. Reflection and Transmission of Surface Plasmon Mode at a Step Discontinuity. *IEEE Photon. Technol. Lett.*, 9:220–222, 1997.

[155] B. A. F. Puygranier, P. Dawson, Y. Lacroute, and J.-P. Goudonnet. Surface plasmon polariton propagation across a gentle silver step. *Surf. Science*, 490:85–98, 2001.

[156] T. P. Shen, R. F. Wallis, A. A. Maradudin, and G. I. Stegeman. Interference phenomena in the refraction of a surface polariton by vertical dielectric barriers. *Appl. Opt.*, 23:607–611, 1984.

[157] F. Pincemin, A. A. Maradudin, A. D. Boardman, and J.-J. Greffet. Scattering of a surface plasmon polariton by a surface defect. *Phys. Rev. B*, 50:15261–15275, 1994.

[158] J. A. Sańchez-Gil. Surface defect scattering of surface plasmon polaritons: Mirrors and light emitters. *Appl. Phys. Lett.*, 73:3509–3511, 1998.

[159] J. A. Sańchez-Gil and A. A. Maradudin. Near-field and far-field scattering of surface plasmon polaritons by one-dimensional surface defects. *Phys. Rev. B*, 60:8359–8367, 1999.

[160] M. B. Sobnack, W. C. Tan, N. P. Wanstall, T. W. Preist, and J. R. Sambles. Stationary Surface Plasmons on a Zero-Order Metal Grating. *Phys. Rev. Lett.*, 80:5667–5670, 1998.

[161] A. A. Maradudin, R. F. Wallis, and G. I. Stegeman. Surface polariton reflection and transmission at a barrier. *Sol. State Commun.*, 46:481–485, 1983.

[162] F. Pincemin and J.-J. Greffet. Propagation and localization of a surface plasmon polariton on a finite grating. *J. Opt. Soc. Am. B*, 13:1499–1509, 1996.

[163] E. Hecht. *Optics*. Addison-Wesley, 4$^{\text{th}}$ edition, 2002.

[164] J. J. Burke, G. I. Stegeman, and T. Tamir. Surface-polariton-like waves guides by thin, lossy metal films. *Phys. Rev. B*, 33:5186–5201, 1986.

[165] P. Berini. Plasmon-polariton waves guided by thin lossy metal films of finite width: Bound modes of symmetric structures. *Phys. Rev. B*, 61:10484–10503, 2000.

[166] M. Fukui, V. C. Y. So, and R. Normandin. Lifetimes of Surface Plasmons in Thin Silver Films. *Phys. Stat. Sol. (B)*, 91:K61–K64, 1979.

[167] D. Sarid. Long-Range Surface-Plasma Waves on Very Thin Metal Films. *Phys. Rev. Lett.*, 47:1927–1930, 1981.

[168] H. Dohi, Y. Kuwamura, M. Fukui, and O. Tada. Long-Range Surface Plasmon Polaritons in Metal Films Bounded by Similar-Refractive-Index Materials. *J. Phys. Soc. Jpn.*, 53:2828–2836, 1984.

[169] P. Berini. Plasmon-polariton waves guided by thin lossy metal films of finite width: Bound modes of asymmetric structures. *Phys. Rev. B*, 63:125417–1–15, 2001.

[170] A. Bouhelier, Th. Huser, H. Tamaru, H.-J. Güntherodt, D. W. Pohl, F. I. Baida, and D. Van Labeke. Plasmon optics of structured silver films. *Phys. Rev. B*, 63:155404–1–9, 2001.

[171] B. Lamprecht, J. R. Krenn, G. Schider, H. Ditlbacher, M. Salerno, N. Felidj, A. Leitner, F. R. Aussenegg, and J. C. Weeber. Surface plasmon propagation in microscale metal stripes. *Appl. Phys. Lett.*, 79:51–53, 2001.

[172] A. Bouhelier and G. P. Wiederrecht. Excitation of broadband surface plasmon polaritons: Plasmonic continuum spectroscopy. *Phys. Rev. B*, 71:195406–1–7, 2005.

[173] S. A. Darmanyan and A. V. Zayats. Light tunneling via surface plasmon polariton states and the enhanced transmission of peridically nanostructured metal films: An analytical study. *Phys. Rev. B*, 67:35424–1–7, 2003.

[174] T. W. Ebbesen, H. J. Lezec, H. F. Ghaemi, T. Thio, and P. A. Wolff. Extraordinary optical transmission through sub-wavelength hole arrays. *Nature*, 391:667–669, 1998.

[175] J. Bravo-Abad, L. Martin-Moreno, and F. J. Garcia-Vidal. Transmission properties of a single metallic slit: From the subwavelength regime to the geometrical-optics limit. *Phys. Rev. E*, 69:26601–1–6, 2004.

[176] F. Marquier, J.-J. Greffet, S. Collin, F. Pardo, and J. L. Pelouard. Resonant transmission through a metallic film due to coupled modes. *Opt. Express*, 13:70–76, 2005.

[177] T. Thio, K. M. Pellerin, R. A. Linke, H. J. Lezec, and T. W. Ebbesen. Enhanced light transmission through a single subwavelength aperature. *Opt. Lett.*, 26:1972–1974, 2001.

[178] U. Schröter, S. Seider, S. Tode, and D. Heitmann. Surface plasmon reflection at edges and resonance effects in metal bars. *Ultramicros.*, 68:223–230, 1997.

[179] F. I. Baida, D. Van Labeke, and J.-M. Vigoureux. Near-field surface plasmon microscopy: A numerical study of plasmon excitation, propagation, and edge interaction using a three-dimensional Gaussian beam. *Phys. Rev. B*, 60:7812–7815, 1999.

[180] L. Salomon, G. Bassou, H. Aourag, J. P. Dufour, F. de Fornel, F. Carcenac, and A. V. Zayats. Local excitation of surface plasmon polaritons at discontinuities of a metal film:

Theoretical analysis and optical near-field measurements. *Phys. Rev. B*, 65:125409–1–5, 2002.

[181] P. Dawson, B. A. F. Puygranier, W. Cao, and F. de Fornel. The interaction of surface plasmon polaritons with a silver film edge. *J. Microsc.*, 194:578–583, 1999.

[182] B. Steinberger. Internal communication – unpublished. Karl Franzens University and Erwin Schrödinger Institute for Nanoscale Research, Graz, Austria, January 2006.

[183] J. Seidel, S. Grafström, L. Eng, and L. Bischoff. Surface plasmon transmission across narrow grooves in thin silver films. *Appl. Phys. Lett.*, 82:1368–1370, 2003.

[184] J. Seidel, F. I. Baida, L. Bischoff, B. Guizal, S. Grafström, D. Van Labeke, and L. M. Eng. Coupling between surface plasmon modes on metal films. *Phys. Rev. B*, 69:121405–1–4, 2004.

[185] R. C. Reddick, R. J. Warmack, and T. L. Ferrell. New form of scanning optical microscopy. *Phys. Rev. B*, 39:767–770, 1989.

[186] O. Marti, H. Bielefeldt, B. Hecht, S. Herminghaus, P. Leiderer, and J. Mlynek. Near-field optical measurement of the surface plasmon field. *Opt. Commun.*, 96:225–228, 1993.

[187] R. Stöckle, C. Fokas, V. Deckert, R. Zenobi, B. Sick, B. Hecht, and U. P. Wild. High-quality near-field optical probes by tube etching. *Appl. Phys. Lett.*, 75:160–162, 1999.

[188] J. U. Schmidt, H. Bergander, and L. M. Eng. Shear force interaction in the viscous damping regime studied at 100 pn force resolution. *J. Appl. Phys.*, 87:3108–3112, 2000.

[189] D. Taverna and J.-C. Weeber. Internal communication within the Network of Excellence – Plasmo-Nano-Devices project WP 19.1.1. Université de Bourgogne, May 2005.

[190] P. Berini. Plasmon-polariton modes guided by a metal film of finite width. *Opt. Lett.*, 24:1011–1013, 1999.

[191] R. Zia, M. D. Selker, and M. L. Brongersma. Leaky and bound modes of surface plasmon waveguides. *Phys. Rev. B*, 71:165431–1–9, 2005.

[192] J. R. Krenn, B. Lamprecht, H. Ditlbacher, G. Schider, M. Salerno, A. Leitner, and F. R. Aussenegg. Non-diffraction-limited light transport by gold nanowires. *Europhys. Lett.*, 60:663–669, 2002.

[193] J. C. Weeber, Y. Lacroute, and A. Dereux. Optical near-field distributions of surface plasmon waveguide modes. *Phys. Rev. B*, 68:115401–1–10, 2003.

[194] J. R. Krenn and J. C. Weeber. Surface plasmon polaritons in metal stripes and wires. *Phil. Trans. R. Soc. Lond. A*, 362:739–756, 2004.

[195] T. Ishi, J. Fujikata, K. Makita, T. Baba, and K. Ohashi. Si Nano-Photodiode with a Surface Plasmon Antenna. *Jpn. J. Appl. Phys.*, 44:L364–L366, 2005.

Publications

Papers

A. Bouhelier, J. Renger, M. R. Beversluis, and L. Novotny, *Plasmon-coupled tip-enhanced near-field optical microscopy*, J. Microsc. **210**, 220–224 (2004).

J. Renger, S. Grafström, V. Deckert, and L. M. Eng, *Evanescent wave scattering and local electric field enhancement at ellipsoidal silver particles in the vicinity of a glass surface*, J. Opt. Soc. Am. A. **21**, 1362–1367 (2004).

L. M. Eng, S. Grafström, I. Hellmann, C. Loppacher, T. Otto, J. Renger, F. Schlaphof, J. Seidel, and U. Zerweck, *Nanoscale nondestructive electric field probing in ferroelectrics, organic molecular films, and near-field optical nanodevices*, Proc. SPIE **5392**, 21–35 (2004).

J. Renger, S. Grafström, R. Hillenbrand, and L. M. Eng, *Resonant light scattering by near-field-induced phonon polaritons*, Phys. Rev. B **71**, 75410-1–7 (2005).

J. Renger, S. Grafström, and L. M. Eng, *SPP excitation at single and multiple slits in metals and thin metal films*, in preparation (2006).

Conference contributions

talks

J. Renger, *Optics and Properties of Novel SNOM Tips*, Workshop Photonics in Electronics Technologies, Dresden, July 1-2, 2002.

J. Renger, S. Grafström, B. Schmidt, L. Bischoff, B. Köhler, and L. M. Eng, *Investigation of aperture SNOM levers fabricated by FIB patterning and wet chemical etching*, 7$^{\text{th}}$ International Conference on Near-field Optics and Related Techniques, Rochester NY (USA), August 11-15, 2002.

J. Renger, I. Hellmann, S. Grafström, V. Deckert, and L. M. Eng, *Modellierung der Feld-*

verstärkung an metallischen Spitzen, Spring meeting of the German Physical Society (DPG), Dresden, March 24-28, 2003.

J. Renger, J. Seidel, I. Hellmann, S. Grafström, V. Deckert, and L. M. Eng, *Field Enhancement at sharp metal tips*, The International Symposium on Optical Science and Technology, SPIE's 48th Annual Meeting, San Diego CA (USA), August 4-8, 2003.

J. Renger, I. Hellmann, S. Grafström, V. Deckert, and L. M. Eng, *Evanescent wave scattering and local electric field enhancement at ellipsoidal silver particles in the proximity of a glass surface*, Progress in Electromagnetic Research Symposium, Pisa (Italy), March 38-31, 2004.

I. Hellmann, J. Renger, S. Grafström, L. M. Eng, and V. Deckert, *Optical field enhancement at coated metal spheroids*, Proceedings of the XIX International Conference on Raman Spectroscopy, Gold Coast, Queensland (Australia), August 8-13, 2004.

P. Olk, J. Seidel, J. Renger, S. Grafström, L. M. Eng, M. Ott, and M. Möller, *Collective Surface Plasmon Propagation in Gold Particle Ensembles*, The 8th International Conference on Near-field Nano Optics & Related Techniques, Seoul (Korea), September 5-9, 2004.

I. Hellmann, J. Renger, S. Grafström, L. M. Eng, and V. Deckert, *Numerical Investigation of the Optical Near Field at Silver Coated Metal Particles*, The 8th International Conference on Near-field Nano Optics & Related Techniques, Seoul (Korea), September 5-9, 2004.

J. Renger, S. Grafström, I. Hellmann, V. Deckert, and L. M. Eng, *Evanescent wave scattering and local electric field enhancement at ellipsoidal silver particles in the vicinity of a glass surface*, The 8th International Conference on Near-field Nano Optics & Related Techniques, Seoul (Korea), September 5-9, 2004.

J. Renger, S. Grafström, L. M. Eng, and R. Hillenbrand, *Light scattering by localized phonon polaritons*, The 8th International Conference on Near-field Nano Optics & Related Techniques, Seoul (Korea), September 5-9, 2004.

J. Renger, S. Grafström, R. Hillenbrand, and L. M. Eng, *Resonant light scattering by near-field induced localized phonon polaritons*, Spring meeting of the German Physical Society (DPG), Berlin, March 4-9, 2005.

P. Olk, T. Härtling, J. Renger, S. Grafström, L. M. Eng, B. Gorzolnik, M. Ott, and M. Möller, *Near- and Farfield Scattering Properties of Metal Nanoparticles Excited by Radially Polarized Light*, Spring meeting of the German Physical Society (DPG), Dresden, March 27-31, 2006.

J. Renger, S. Grafström, J. Seidel, P. Olk, L. M. Eng, C. Akhmadaliev, L. Bischoff, B. Schmidt, D. Taverna, and J.-C. Weeber, *Excitation of surface plasmon polaritons at surface grooves in bulk metals and thin film metal waveguides*, Spring meeting of the German Physical Society (DPG), Dresden, March 27-31, 2006.

posters

A. Bouhelier, J. Renger, M. Beversluis, and L. Novotny, *Plasmon coupled tip-enhanced near-field optical microscopy*, 7th International Conference on Near-field Optics and Related Techniques, Rochester NY (USA), August 11-15, 2002.

V. Deckert, J. Renger, and L. M. Eng, *MMP Calculation of the electromagnetic field enhancement at sharp noble metal tips for tip-enhanced Raman scattering*, 7th International Conference on Near-field Optics and Related Techniques, Rochester NY (USA), August 11-15, 2002.

J. Seidel, J. Renger, S. Grafström, L. Bischoff, and L. M. Eng, *Surface Plasmon Propagation in Structured Metal Films*, Surface Plasmon Photonics, EuroConference on Nano-Optics, Granada (Spain), September 20-25, 2003.

J. Renger, J. Seidel, P. Olk, S. Grafström, L. M. Eng, B. Schmidt, L. Bischoff, and C. Akhmadaliev, *Focussing of surface plasmon polaritons by triangle-shaped waveguides and coupled SPP resonantors*, 24nd Research Workshop and Network Council Meeting, Belfast (UK), December 12-14, 2004.

J. Renger, J. Seidel, R. Lettow, P. Olk, S. Grafström, and L. M. Eng, *Focussing of light using coupled surface plasmon resonantors*, Surface Plasmon Photonics 2, Graz (Austria), May 21-26, 2005.

J. Renger, S. Grafström, J. Seidel, P. Olk, L. M. Eng, C. Akhmadaliev, L. Bischoff, and B. Schmidt, *Excitation of surface plasmon polaritons at grooves and gratings*, Surface Plasmon Photonics 2, Graz (Austria), May 21-26, 2005.

S. Grafström, J. Renger, S. Schneider, and L. M. Eng, *The Role of Polaritons in Scattering Near-field Optical Microscopy*, Fall meeting of the Materials Research Society MRS, Boston, (USA), November 28 - December 2, 2005.

Acknowledgement

and checking the content and language.

Die vorliegende Arbeit wurde am Institut für Angewandte Physik/Photophysik der Technischen Universität Dresden unter wissenschaftlicher Betreuung von Prof. Dr. Lukas M. Eng durchgeführt.

Versicherung

Hiermit versichere ich, dass ich die vorliegende Arbeit ohne unzulässige Hilfe Dritter und ohne Benutzung anderer als der angegebenen Hilfsmittel angefertigt habe; die aus fremden Quellen direkt oder indirekt übernommenen Gedanken sind als solche kenntlich gemacht. Die Arbeit wurde bisher weder im Inland noch im Ausland in gleicher oder ähnlicher Form einer anderen Prüfungsbehörde vorgelegt.

Dresden, den 22.05.2006